



Strålsäkerhets
myndigheten

Swedish Radiation Safety Authority

Authors:

Steven J. Benbow
Peter C. Robinson
Sarah P. Watson

Research

2011:12

Analysis of Barrier Performance:

Modelling of Copper corrosion scenarios with and without buffer erosion

SSM perspective

Background

Based on the safety assessment SR-Can in 2006 the advection- corrosion case can be expected to be the dominant canister failure mechanism in a KBS-3 repository for spent nuclear fuel, The SR-Can assessment was, however, completed based on extrapolation of results from analysis of various static conditions of the buffer. There is thus a need to explore modelling approaches which can better account for the gradual evolution of buffer conditions. The Swedish Radiation Safety Authority (SSM) and its predecessors (SKI and SSI) has previously only thoroughly analysed copper corrosion in cases where the buffer has been assumed to remain intact during the assessment period. The present study was initiated to contribute to bridging the gap between recent knowledge developing in the area of buffer erosion and the mass-transfer limited model of copper corrosion, by developing a dynamic model covering these coupled phenomena. It was recognised already from the start that such a development could in its initial phase only result in a preliminary and incomplete model. The representation of both buffer erosion and copper corrosion in the model should therefore be regarded as incomplete and may have to be further updated in possible subsequent stages of model development.

Objectives

The purpose of this project was to develop a numerical modelling capacity to address the corrosion of the copper canister under gradually changing transport conditions caused by buffer erosion and removal of buffer mass. Due to the complexity of this task, such a model cannot be realistic in all respects, but the present effort should address the feasibility of solving numerical and computational problems as well as providing preliminary results that can guide future model development. The present results may also be used to preliminarily assess the performance implications of various assumptions and experimental data.

Results

This report contains a range of modelling results from calculation cases corresponding to various conditions of the buffer such as intact buffer, imposed cavities in a buffer, gradually evolving buffer density with a spatial resolution of density, and microbial reduction of sulphate in regions of the buffer with low buffer density. The results show that the conditions of buffer with mass loss involving buffer density evolution, supply of groundwater sulphide from fractures (intersecting deposition holes) and local SRB activity all contributes to an uneven corrosion profile on the canister. This is not caused by a true localized corrosion phenomenon but rather by what might be termed as an uneven general corrosion of copper caused by geometrically distributed corrodent supply. The present formulation of SRB activity suggests only a moderate influence on copper corrosion.

Need for further research

A future goal will be to provide a more detailed, defensible and comprehensive assessment of the advection- corrosion case.

Project Information

Project manager: Bo Strömberg

Reference: SSM 2010/829



Strål
säkerhets
myndigheten

Swedish Radiation Safety Authority

Authors: Steven J. Benbow, Peter C. Robinson and Sarah P. Watson
Quintessa Limited, Henley-on-Thames, England

2011:12

Analysis of Barrier Performance:
Modelling of Copper corrosion scenarios with and without buffer erosion

Date: February 2011

Report number: 2011:12 ISSN: 2000-0456

Available at www.stralsakerhetsmyndigheten.se

This report concerns a study which has been conducted for the Swedish Radiation Safety Authority, SSM. The conclusions and viewpoints presented in the report are those of the author/authors and do not necessarily coincide with those of the SSM.

Summary

SKB have identified buffer erosion as a process that could potentially lead to increased corrosion of the copper canister. Buffer erosion can be caused by: the formation of bentonite (i.e., montmorillonite) colloids and their transport away from deposition holes in intersecting fractures containing dilute groundwaters (such as subglacial meltwaters); steep hydraulic gradients during buffer resaturation; or shearing of solid bentonite particles by rapidly flowing groundwater. Only colloidal removal of bentonite (the first of the processes listed) is considered in this study. The erosion of the bentonite leads to a reduction in density and swelling potential, and hence a lowering of transport resistances in the buffer that can make it easier for corrosive agents to be transported to the canister surface, resulting in increased levels of corrosion of the canister surface compared with those predicted in “normal evolution” conditions.

The reduction in bentonite density that follows as a consequence of erosion also leads to the possibility of breaching other safety functions of the buffer, for example prevention of canister sinking and resistance to shear deformation. These are not considered in this study.

This report describes the modelling of copper corrosion processes in the SKB KBS-3 design concept. The modelling includes an initial representation of all relevant physical processes, but with some processes represented in more detail than others. This allows investigation of the impacts of the processes that are modelled on canister corrosion, allowing identification of the processes that impact most on the key performance measures for the EBS, which will help to focus modelling developments in future work. This work could be taken as the starting point in a longer-term modelling study in which the interactions between processes that affect canister corrosion are further investigated.

Two high-level scenarios are considered in this work: a base case scenario in which the buffer is assumed to remain intact; and a scenario in which (colloidal) bentonite erosion takes place. Variant cases for each scenario are considered to investigate sensitivities. In the latter scenario the bentonite erosion process is represented in a simplified way, and the subsequent redistribution of the bentonite within the buffer is controlled by a single rate term that acts to equalise the density of the buffer. The same buffer redistribution process is used to model the extrusion of the bentonite into the fracture. In future work this representation could be replaced by a more chemically-based representation of the erosion processes and a more mechanistic representation of the bentonite redistribution process.

The modelling has been performed using Quintessa’s QPAC general purpose modelling software together with relevant modules. This collection of components has previously been referred to as QPAC-EBS. By using QPAC we have been able to model coupled mechanical, hydro and chemical

processes, albeit with some of the process representations being simplified, in a way that has not been done previously. A satisfactory understanding of the evolution of the EBS will be a key issue in the review of SR-Site and this work illustrates the capability to undertake independent model simulations to test the assumptions made by SKB.

The objective of the work presented here was to demonstrate a flexible and independent capability that can be used to support regulatory review.

Building on earlier modelling work and utilising the general-purpose QPAC software, a coupled model for the evolution of the EBS system through a sequence of glacial cycles has been developed and applied. The flexibility of the approach has been demonstrated by modelling a range of scenarios and variants covering both parameter variations and conceptual model alternatives.

Although many simplifying assumptions have been made, particularly in the chemistry aspects, a rich variety of behaviour is seen in the modelling results. The linkage between erosion and corrosion has been clearly demonstrated to depend on factors such as the precise geometry of any cavities that form in the buffer due to erosion in addition to the physical and chemical parameters of the system.

The flexibility of the QPAC approach, with models being coded in the input language, has allowed the required range of processes to be treated at a suitable level. It proved possible to develop models over relatively short time periods, demonstrating that the approach should be sufficiently responsive to address issues that arise during the review process. In future work the sophistication with which particular processes are modelled can be adjusted to suit the needs of specific investigations.

The simulations presented here should be taken as illustrative and indicative. At this preliminary stage of the modelling it would be premature to consider any of the results to be definitive.

Contents

1	Introduction	1
2	Scenarios	4
3	System Features and Geometry	7
	3.1 The Buffer	7
	3.2 Cavities	7
	3.3 The Buffer/Host Rock Interface	8
	3.4 The Fracture	8
	3.5 Bentonite Gel	9
	3.6 The Canister	9
	3.7 The Buffer/Backfill Interface	9
	3.8 Tunnel Backfill	9
	3.9 The EDZ	9
4	Processes	10
	4.1 Thermal Processes	10
	4.2 Corrosion	11
	4.3 The Role of Pyrite in the Buffer	12
	4.4 Other Chemical Processes	13
	4.5 Microbial Processes	16
	4.6 Bentonite Redistribution	17
	4.7 Erosion	19
	4.8 Bentonite Gel Extrusion	20
	4.9 Groundwater Flow	21
	4.10 Groundwater-mediated Transport	21
	4.11 Spalling	21
5	External Factors	22
	5.1 Groundwater Chemistry	22
	5.2 Flow rates	22
	5.3 Frequency of Glaciation	24
6	The Simplified Buffer Redistribution Model	25
7	The Erosion Model	29
	7.1 Verification with a simple constant erosion rate	29
	7.2 A Colloid Capacity-Based Erosion Model	36
8	The Base Case Scenario	43
	8.1 FEP Representation	43
	8.2 Parameterisation	45
	8.3 Calculations	47
9	The Base Case Scenario with Imposed Buffer Cavities	56
	9.1 FEP Representation	59
	9.2 Parameterisation	60
	9.3 Calculations	60
10	Erosion Case Modelling	70
	10.1 FEP Representation	71
	10.2 Parameterisation	72
	10.3 Calculations	74

11 Modelling Erosion and Microbial Effects	89
11.2 FEP Representation	93
11.3 Parameterisation	94
11.4 Calculations	95
12 Summary	105
13 Relevance for the SR-Site Review	108
References	109
Appendix A: Possible Variants for Future Studies	111

1 Introduction

This report documents modelling studies undertaken during 2010 in preparation for the SR Site review.

The studies described here relate to coupled modelling the processes of canister corrosion and buffer erosion. A sister report [1] documents work related to consequence analysis calculations, that is to the calculation of radionuclide release and transport if a canister is breached.

SKB have identified buffer erosion as a process that could potentially lead to greater levels of corrosion of the copper canister [2]. Buffer erosion can be caused by: the formation of bentonite (i.e., montmorillonite) colloids and their transport away from deposition holes in intersecting fractures containing dilute groundwaters (such as subglacial meltwaters); and by steep hydraulic gradients during buffer resaturation; or by shearing of solid bentonite particles by rapidly flowing groundwater. Only colloidal removal of bentonite (the first of the processes listed) is considered in this study. The erosion of the bentonite leads to a reduction in density and swelling potential, and hence a lowering of transport resistances in the buffer that can make it easier for corrosive agents to be transported to the canister surface, resulting in increased levels of corrosion of the canister surface than are predicted in “normal evolution” conditions.

The reduction in bentonite density that follows as a consequence of erosion also leads to the possibility of breaching other safety functions of the buffer, such as resistance to shear deformation and prevention of canister sinking. These are not considered in this study.

This report describes the modelling of copper corrosion processes in the SKB KBS-3 design concept. The modelling includes an initial representation of all relevant physical processes, but with some processes represented in more detail than others. This allows investigation of consequences of the processes that are modelled, allowing identification of the processes that impact most on the key performance measures of the EBS, which will help to focus developments in future work. This work could be taken as the starting point in a longer-term modelling study in which the interactions between processes that affect canister corrosion are further investigated.

The work reported here makes a first attempt at modelling a complex coupled system. At this stage, many of the process models used and parameter values taken are speculative. The purpose of the work is to develop a capability to model the coupled processes involved in erosion and corrosion which can be used to explore various scenarios of interest. The scenarios explored should be considered as indicative only and the results presented should be viewed as illustrative. No attempt has been made to compare calculations with experimental results.

The focus of the corrosion modelling is on the sulphidic corrosion of the copper. The initially oxic corrosion conditions following the closure period are assumed to occur at early times before the period modelled. Anoxic (pure water) corrosion processes have been the subject of separate review [3] and are not included in the current modelling, although they could be addressed using QPAC in a future study. The modelling considers various sources of sulphide ions such as microbially reduced sulphate from naturally occurring sulphate in the groundwater and those that arise from dissolution of accessory minerals in the bentonite (e.g. directly from pyrite, or from sulphate released by gypsum dissolution that may be subsequently converted to sulphide by sulphate reducing bacteria). Alternative sulphide solubility limiting factors can be considered (e.g. FeS_2 , $\text{FeS}_{(\text{am})}$) to assess their effect on corrosion rates.

A key output of the modelling is the investigation of the potential for non-uniform corrosion profiles to develop across the canister surface, beyond those which develop due to the localised source of sulphide at the fracture. For example, bentonite erosion leading to a non-uniform bentonite density field may result in faster transport regions that carry sulphide ions to the canister surface in specific locations, resulting in more uneven corrosion.

Two scenarios are considered in this work: a base case scenario in which the buffer is assumed to remain intact; and a scenario where (colloidal) bentonite erosion takes place. Variant cases for each scenario are considered to investigate sensitivities. In the latter scenario, the bentonite erosion process is represented in a simplified way, and the subsequent redistribution of the bentonite within the buffer is controlled by a single rate term (representing the effects of swelling pressure) that acts to equalise density in the buffer. The same buffer redistribution process is used to model extrusion of bentonite into the fracture. In future, these could be replaced by a more chemically-based representation of the erosion processes and a more mechanistic representation of the redistribution process.

In the scenario in which erosion is assumed to occur, periods of erosion are imposed as a cyclic process repeating over timescales that are consistent with expected frequencies of glaciations up to a cut-off time of a million years. This allows investigation of the potential for rates of corrosion to gradually increase due to successive loss of buffer material in each cycle. During periods of erosion, the in-situ groundwaters in the rock hosting the EBS are likely to change (in particular the sulphate and sulphide content may vary, as will the redox conditions) and so the host rock water boundary condition in the model is imposed as a time-varying water composition.

The modelling has been performed using Quintessa's QPAC general purpose modelling software together with relevant modules. This collection of components has previously been referred to as QPAC-EBS [4].

Decisions on the features and processes to be included in the simulations and the level of detail in which they should be represented were based on discussions from a FEP workshop held in July 2010. Useful discussions were also held with Adrian Bath during the study and his input is gratefully acknowledged.

The simulations that have been undertaken are 3D and represent one half of the EBS and fracture due to the symmetry of the system. A relatively coarse grid has been used to keep run times practical. Non-uniform gridding is used to provide higher resolution where the system is expected to alter most and near key interfaces that system evolution is likely to be sensitive to. Specific cases can be re-run with a higher grid resolution where necessary.

In Section 2 of this report, the scenarios that have been considered are introduced. Details of the representation of the features and processes that need to be modelled are discussed in Sections 3 and 4 respectively. Section 5 describes the handling of external factors that drive system evolution, Section 6 gives details of the way mass redistribution is modelled, and Section 7 discusses erosion modelling. The remaining sections describe the calculations.

An appendix documents some variants could be considered in future studies but which have not been modelled in the current study.

2 Scenarios

Two high-level scenarios are considered in the study:

- ▲ a scenario in which the buffer remains intact (i.e. no erosion occurs); and
- ▲ a scenario in which the buffer is assumed to erode during periods of intrusion of glacial meltwaters.

The first scenario acts as a base case for comparison with the second scenario in order to assess the impact of the eroding buffer. Variant cases for each scenario are used to investigate sensitivities.

The two scenarios are illustrated in Figure 2-1. The system is taken to be comprised of a copper canister located in a tunnel deposition hole and surrounded by bentonite. The top of the deposition hole interfaces with a backfilled tunnel. An excavation damaged zone (EDZ) may exist around the tunnel. A fracture (or fractures) intersects the deposition hole, providing a route for flowing groundwater to arrive and leave. Bentonite is extruded into the fracture as a consequence of the swelling pressure in the deposition hole. In the buffer erosion scenario, the buffer/fracture porewater interface (which is initially at the tip of the extruded bentonite) provides a location for destabilised bentonite colloids to be eroded, thus reducing the net density of the buffer. In this case, a cavity in the bentonite can potentially form if the rheological properties of the bentonite do not give rise to redistribution at a rate that is comparable to the rate at which mass is lost due to colloid removal. The potential for backfill material to enter from the tunnel is also possible if the reduction in bentonite density is sufficient, but this is not modelled in this study.

The starting point for the simulations is after the initial transient period in which the buffer is assumed to resaturate homogeneously, so that only fully saturated conditions are considered. It is assumed that the bentonite extrusion into the fracture only begins once the buffer is fully resaturated so that this process begins when the simulation commences. In reality the period over which this process occurs will coincide with the buffer resaturation period, but since the timescale for extrusion is relatively small any inconsistency introduced by this assumption is expected to be minor. Extensions to the model to consider incomplete or inhomogeneous resaturation could be considered in a future study.

Sulphate and sulphide ions are assumed to be present in the flowing groundwater. In the buffer, gypsum and pyrite are the only additional sources of sulphate and sulphide. Sulphate reducing bacteria (SRB) are present and assumed to be active in the host rock. SRB are also assumed to be present in the buffer, but the intact buffer swelling pressure is sufficient to prevent them from being active to a significant extent.

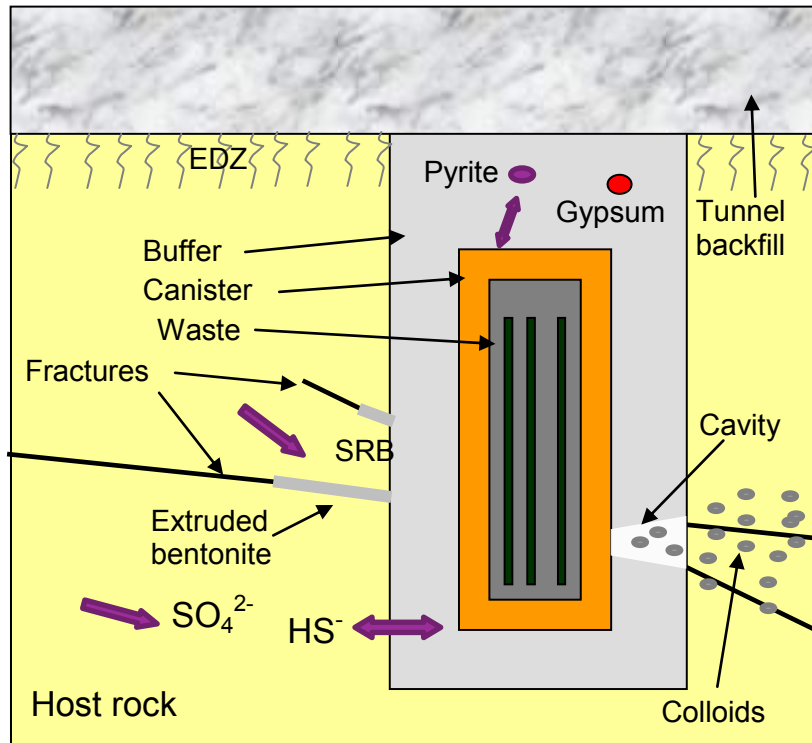


Figure 2-1 Illustration of the scenario in which the buffer has eroded (after [5]). The non-eroding buffer only differs by the absence of the cavity and colloids

The key output of interest from the modelling is the degree of corrosion of the surface of the copper canister and its spatial profile. In particular, conditions that lead to the potential for regions of enhanced corrosion are of interest. The following issues are explored in both scenarios:

- ▲ The role of sulphide supply in groundwater, taking account of natural groundwater concentrations, flow rates, and diffusion within buffer, where geometric considerations will lead to higher corrosion nearer the fracture plane, particularly on the up-stream side; and
- ▲ The role of sulphate reducing bacteria (SRB).

The role of sulphide originating in the buffer, specifically from dissolution of pyrite that is initially present and possibly inhomogeneously distributed in the buffer, and its potential to lead to uneven corrosion of the canister surface, is discussed in Section 4.3.

For the scenario where the buffer erodes, the following additional issues are investigated:

- ▲ The potential for transport of sulphide to the canister (or part-way to the canister) by advection, taking account of:

- the impact of redistribution of buffer material;
 - the geometry of any cavity in the buffer; and
 - the relationship with the SKB performance criterion of 1200 kg loss of buffer material.
- ▲ The impact of changed buffer diffusivity (characterised by the relationship to buffer density).
 - ▲ The effect of SRB in the presence of cavities or reduced density buffer.

Details of the representation of the features and processes listed above are given in the sections that follow.

3 System Features and Geometry

The key features in the system are shown in Figure 2-1. In the subsections that follow the way in which each feature is represented in the simulations is discussed. Variant cases that are considered in this study are highlighted as bullet points. Variants that might be considered in a future study are described in Appendix A.

3.1 The Buffer

The starting point for the simulations is after the initial transient period of buffer resaturation. As noted in Section 2, it is assumed that this period precedes intrusion of bentonite into the fracture. The buffer is assumed to be homogeneously resaturated¹ with a uniform swelling pressure throughout the buffer that is consistent with SKB's reference design. The only exception to this uniformity assumption is that the outer annulus of the buffer derives from saturated bentonite pellets.

The buffer composition is assumed to be bentonite with pyrite and gypsum as accessory minerals. Pyrite weight percentages in MX-80 and Deponit CA-N bentonites are given as 0.07 and 0.5 wt% in [2], with an uncertainty of $\pm 0.05\%$ (in both cases). There is some ambiguity concerning the interpretation of this value – whether every bentonite block will be expected to satisfy this pyrite weight percentage, or whether blocks with larger or smaller weight percentages will be accepted if, on the whole, the buffer pyrite content is sufficiently low. This leads to the possibility of a heterogeneous pyrite distribution within the bentonite and hence the possibility of localised sulphide sources in the buffer if pyrite is found to dissolve, or regions within the buffer where pyrite concentrations are low and hence solubility limits on sulphide may be controlled by higher solubility phases (e.g. $\text{FeS}_{(\text{am})}$). The potential for pyrite dissolution to act as a source of sulphide and give rise to uneven corrosion of the canister surface is considered in Section 4.3.

3.2 Cavities

A cavity in the buffer could potentially arise if the buffer does not redistribute itself at a rate comparable with the rate of erosion. This of

¹ There is some evidence (e.g. from SKB's canister retrieval test (e.g., [4]) to suggest that homogeneous resaturation may not take place, or that it will only be possible over long timescales (beyond the canister thermal phase). These issues are not considered in the current study, but could be included in future studies.

course assumes that erosion within the deposition hole is actually possible, which has not yet been studied in detail by SKB. SKB's modelling to date has considered only erosion in the fracture at the tip of the extruded bentonite gel (see [6] and the references therein) with any impacts on the bulk loss rates in the buffer being upscaled from the loss rates derived in the fracture. In the current study, the erosion process (discussed in Section 4) is implemented in a simplified manner with the rate of erosion being directly imposed, or imposed as a groundwater flow-dependent rate. The bentonite redistribution process is also represented in a simplified manner as a process that acts to equalise density at a specified rate. The same process is used to control the extrusion into the buffer. These choices allow a range of potential cavity structures or density reduction profiles to develop with a suitable parameterisation of the model.

3.3 The Buffer/Host Rock Interface

The buffer/host rock interface is only important if piping flow pathways are assumed to have arisen during the resaturation phase. Resaturation is assumed to have completed prior to the simulations, hence the piping pathways could be implemented as an initial condition in the simulations by including a thin feature at the edge of the buffer with suitably specified flow parameters. Piping features that develop early might be healed by later swelling processes. In the simulations no piping features are included.

3.4 The Fracture

The fracture is the primary route for eroded material to leave the buffer and for naturally occurring sulphide and sulphate to enter the buffer. The size of the fracture and its flow properties will affect the rate of groundwater flow, which will in turn affect the rate at which materials can be transported. Additionally, any channelling in the fracture will also affect the flow pathways and rates; the fracture is approximately a 2D feature but could behave more like a 1D feature if flows are highly channelled. The sister report [1] reviewed handling of this interface in the context of radionuclide transport, but that study is also relevant to sulphate and sulphide. It was noted that spalling could have an important effect of transport at this interface; this has not been considered in the current modelling.

In SKB's "semi-correlated models" [2], fracture transmissivities are related to the fracture radius. SKB have shown that they have a high possibility of avoiding fractures with transmissivities on the order of 10^{-5} m²/s, which corresponds to fractures with radius > 100 m. Likely transmissivities are in the range 10^{-10} to 10^{-7} m²/s with 10^{-6} m²/s a likely worst case [7]. Fracture flow rates are discussed in Section 5.

The fracture is implemented as a 3D volume feature in order to derive correct flow rates around the deposition hole.

The simulations include:

- ▲ Investigation of a range of fracture apertures and flow properties.

3.5 Bentonite Gel

As discussed in Section 2, the extent to which bentonite gel intrudes into the fracture at the start of the simulations is calculated using the bentonite redistribution model. The extremity of the gel represents the initial location of the bentonite/groundwater interface and is therefore the location for the onset of erosion. In the simulations it is assumed that:

- ▲ The bentonite gel transport properties are identical to those of the buffer.

3.6 The Canister

The canister surface is represented in the model as a surface boundary condition where the corrosion process is implemented. The interior of the canister is not represented. Corrosion products are not modelled explicitly – this is discussed further in Section 4. The copper thickness is 50 mm [8], so this is the depth against which corrosion should be judged.

3.7 The Buffer/Backfill Interface

The top of the buffer is held in place by the weight of the backfill above it. In principle, backfill material could be transported into the deposition hole if the buffer density falls. To simplify the modelling, the focus is on the buffer only, so:

- ▲ Assume that the buffer/backfill interface is fixed.

3.8 Tunnel Backfill

The tunnel backfill is not represented in the first phase of modelling because of the assumptions made concerning the buffer/backfill interface (see Section 3.7).

3.9 The EDZ

The tunnel EDZ is not included in the simulations.

4 Processes

In the subsections that follow the way in which each process has been represented in the simulations is discussed. Further details are given in Sections 8 and 10. Variant cases that are considered in this study are highlighted as bullet points. Additional variants that might be considered in a future study are discussed in Appendix A.

4.1 Thermal Processes

The strongest part of the thermal pulse from the waste form is assumed to have ended by the time that simulations begin and subsequent thermal effects are ignored in the current modelling. Hence a constant temperature of 12°C has been imposed (SKB [9] give a figure of 11.7°C at 500 m at Forsmark). The chosen value affects the values of equilibrium constants in chemical reactions and transport properties.

Dependence of the diffusion coefficient on temperature can be represented using the Stokes-Einstein formula, which describes the effect of temperature and viscosity on the porewater diffusion coefficient:

$$D_{p,T} = D_{p,298} \frac{T}{298} \frac{\eta_{298}}{\eta_T}$$

where $D_{p,T}$ (m^2/s) is the porewater diffusion coefficient at temperature T (K), and η_T (Pa s) is the viscosity of the fluid at temperature T , which varies according to

$$\eta_T = \eta_{20} \exp\left(-\ln 10 \times \frac{\left(1.37023(T_C - 20) + 8.36 \times 10^{-4}(T_C - 20)^2\right)}{109 + T_C}\right)$$

where T_C is the temperature in °C and 1.002×10^{-3} Pa s (see [10]). Viscosity variation is plotted as a function of temperature in Figure 4-1.

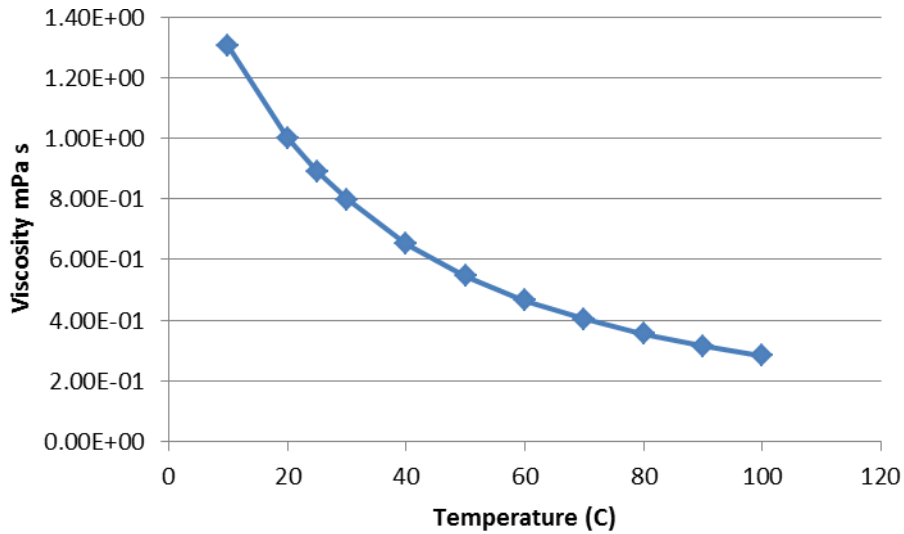
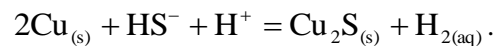


Figure 4-1 Viscosity of water as a function of temperature

4.2 Corrosion

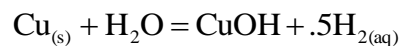
Sulphidic corrosion of the copper canister is the key corrosion process under consideration and proceeds according to the reaction



This reaction is studied in [11], which states that the reaction is typically either under transport control (i.e. limited by the availability of diffusing sulphide) or kinetically controlled (under negative potentials), or both (mixed kinetics). However, in the presence of clays, or in the presence of a thick Cu_2S corrosion product layer, the reaction is stated to be more likely to be under transport control, in which case all sulphide arriving at the canister surface is assumed to be consumed in the corrosion reaction. Thus the approach used in the simulations is

- ▲ Treat corrosion as transport controlled.

The anoxic corrosion reaction

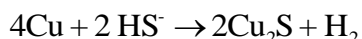


has been reviewed separately [3] and is not considered in the current study.

4.3 The Role of Pyrite in the Buffer

Pyrite precipitation has the potential to impose a solubility limit on sulphide concentrations in the buffer and is considered in the modelling variant cases discussed in Sections 8 and 10. Here we consider the possibility for the dissolution of pyrite that is initially present to provide a transient sulphide source in the buffer and the potential impact on canister corrosion.

As a pessimistic case, we calculate the total volume of copper that could be corroded if all of the sulphur in the buffer was converted to sulphide and was involved in the corrosion reaction:



Each mole of sulphur therefore has the potential to corrode 2 moles of copper. It then follows that each mole of pyrite (FeS_2) has the potential to corrode 4 moles of copper.

According to SKB [2], Table 4-3 and Table 9-10, the wt% of pyrite in MX-80 is 0.07% for MX-80 and 0.5% in Deponit CA-N. These figures are stated to have an uncertainty of 0.05%.

Since there is more buffer above the canister than at the sides, the impact of any corrosion from the initial pyrite will be higher on the top of the canister than on the sides. We pessimistically assume that all the pyrite above the canister corrodes the top of the canister. The MX-80 calculation is described here; the Deponit CA-N result would be 7 times higher.

Given a bentonite (MX-80) dry density of around 1500 kg/m^3 the pyrite density will be 1.05 kg/m^3 . At 120 g/mol this gives 8.75 moles/m^3 of pyrite, enough to corrode 35 moles of copper per m^3 of buffer. The volume of the buffer above the canister is (from Figure 4-4 in [2]) 3.6 m^3 and hence 126 moles of copper can be corroded. This corresponds to about 8.1 kg of copper, or $9 \times 10^{-4} \text{ m}^3$. The surface area of the top of the canister is about 0.9 m^2 giving an average corrosion of 1 mm . This is a factor of two higher than the figure given by SKB [2], Table 9-10, but is still small.

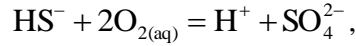
The Deponit CA-N figure would be 7 mm . In [2] it is indicated that the solubility limit for sulphide means that this process would be very slow, a figure of 3 million years for corrosion of the top of the canister is given.

Given that the pyrite source is distributed, it is to be expected that any resulting corrosion would be reasonably uniform. Pyrite occurs naturally in the material and there is no reason to expect it to be concentrated in one region. The most likely cause of a heterogeneous distribution would be for some bentonite blocks to have different pyrite concentrations, but there would have to be much higher concentrations to lead to much more corrosion.

Given the pessimistic nature of this calculation, we conclude that pyrite in an MX-80 buffer would not be an important factor for canister corrosion, but the situation for Deponit CA-N is less clear cut and requires further study.

4.4 Other Chemical Processes

Sulphate and sulphide will interact via the following redox reaction [12]



$$\log K_{\text{rdx}}(12^\circ\text{C}) \approx 145.$$

If the redox reaction is assumed to be in equilibrium then the ion activity product and equilibrium constant are equal and so at 12°C,

$$\frac{[\text{SO}_4^{2-}]}{[\text{HS}^-]} = \frac{[\text{O}_{2(\text{aq})}]^2}{[\text{H}^+]} K_{\text{rdx}} = [\text{O}_{2(\text{aq})}]^2 10^{145+\text{pH}}.$$

The oxygen fugacity equation $\text{O}_{2(\text{g})} = \text{O}_{2(\text{aq})}$ with $\log K_{\text{O}_2}(12^\circ\text{C}) \approx -2.8$ [12] implies that at equilibrium

$$\frac{[\text{SO}_4^{2-}]}{[\text{HS}^-]} = f_{\text{O}_2}^2 10^{139.4+\text{pH}} = (f_{\text{O}_2} 10^{69.7+\text{pH}/2})^2.$$

From this equation we can derive a value for the fugacity f_{O_2} that is necessary to support given $[\text{SO}_4^{2-}]/[\text{HS}^-]$ ratios as a function of pH at redox equilibrium. This is plotted in Figure 4-2. The $\text{O}_{2(\text{aq})}$ activity is related to f_{O_2} by $[\text{O}_{2(\text{aq})}] = f_{\text{O}_2} 10^{-2.8}$ at 12°C. It is clear from the figure that sulphate will quickly dominate the system with activities many orders of magnitude above those of sulphide for f_{O_2} above 10^{-71} bars, equivalent to $\text{O}_{2(\text{aq})}$ activities above 10^{-74} .

Therefore, in order to achieve significant concentrations of sulphide in the porewater, we must treat the redox reaction as being in disequilibrium. This can either be simulated by ignoring the reaction completely, or modelling the reaction with a slow kinetic rate. The approach taken in the modelling is:

- ▲ Ignore the sulphate / sulphide redox reaction and treat sulphate and sulphide as separate species in the model (with SRB providing the only conversion mechanism).

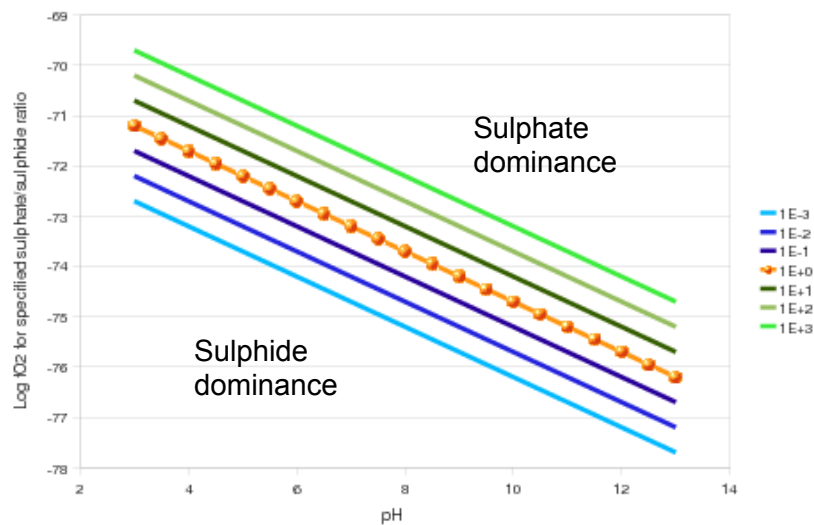
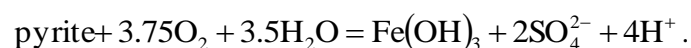


Figure 4-2 Fugacity (bars) required to achieve specified $[\text{SO}_4^{2-}]/[\text{HS}^-]$ ratios as a function of pH, assuming equilibrium in the redox reaction

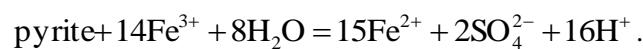
Pyrite dissolution and precipitation will potentially affect the sulphate and sulphide concentrations in the buffer porewaters. Corrodant formation through reductive and/or direct pyrite dissolution is probably feasible, but would in the long-term be constrained by slow redox kinetics and/or solubility limits. In any case, the simple bounding analysis in Section 4.3 provides an estimate on its maximum contribution to copper corrosion. It is therefore not explicitly addressed in the modelling.

Pyrite dissolution is typically formulated as an oxidation reaction that produces sulphate:



This form of pyrite dissolution is infeasible in the low oxygen environments that we would expect in the EBS system.

Oxidation of pyrite by ferric ion (Fe(III)) is known to be faster than oxidation by O_2 . Hence another possible reaction is



The likelihood of this reaction occurring is constrained by the availability of ferric iron. PHREEQC calculations have been performed to speciate the Forsmark groundwater quoted in Table 2-1 of [13]. Three calculations were performed that assumed:

- (1) f_{O_2} equilibrium with magnetite-hematite;

(2) f_{O_2} at $\text{H}_2\text{-H}_2\text{O}$ equilibrium; and

(3) f_{O_2} at 10^{-22} bars, corresponding to a value just below the detection limit [13].

The conditions in (1) are assumed here to be the most realistic assumption for Forsmark water, those in (2) are possible in corroding metal and anoxic water conditions and those in (3) are more likely in soil water conditions.

The total Fe concentration in the Forsmark water is 3.3×10^{-5} mol/l [13]. The results of the PHREEQC calculations are shown in Table 4-1. In every case it is clear that Fe^{2+} dominates Fe^{3+} and that pyrite is only under-saturated in the case of the high oxygen content water. From this it would seem sensible to conclude that under unaltered groundwater conditions pyrite precipitation is more likely to occur than dissolution. Near the canister where sulphide concentrations are lower, and in locations where other chemical processes affect the $\text{Fe}^{2+}/\text{Fe}^{3+}$ ratio, then pyrite dissolution would be more likely.

Table 4-1 Fe^{2+} , Fe^{3+} concentrations (mol/kg) and pyrite saturation index (SI) in the PHREEQC calculations

Case	Fe^{2+}	Fe^{3+}	Pyrite SI
1	3.177e-05	2.403e-22	11.53
2	3.177e-05	4.794e-25	6.13
3	1.821e-09 [†]	5.182e-14	-159.92

[†] $\text{Fe}(\text{OH})_3$ is the dominant Fe species in this case

Given the analysis of Section 4.3, the uncertainty over whether pyrite will dissolve, and the additional complexity that would be needed in the modelling to treat the relevant processes, the simplifying assumption of ignoring pyrite dissolution within the buffer was taken for this study.

Therefore, the modelling imposes a solubility limit on sulphate. $\text{FeS}_{(\text{am})}$ has a higher solubility than pyrite, but precipitates more readily, so may provide a solubility limit for HS^- in the system if it arrives in excess in the buffer (e.g. due to microbial reduction of sulphate) with pyrite unable to consume all of the excess. $\text{FeS}_{(\text{am})}$ will gradually undergo a transition to pyrite, being the more thermodynamically stable mineral. The transformation of $\text{FeS}_{(\text{am})}$ to pyrite is not considered in the current study, which means that potentially HS^- concentrations could become higher than is realistic. This would seem to be a conservative assumption since this will lead to higher rates of corrosion. Therefore the approach taken in the modelling is to:

- ▲ Assume that sulphide is buffered by pyrite and $\text{FeS}_{(\text{am})}$ solubility.

Here, we mean that sulphide and sulphate concentrations are initially determined by the in situ porewater chemistry and this is imposed as a boundary condition on the model. With the exception of SRB, no processes

are assumed to occur within the fracture and buffer system that can increase sulphate and sulphide concentrations, so these imposed values represent the maximum that can be attained in the model (and the solubility limit is implicitly imposed). When SRB are active in the buffer, a solubility limit is imposed as described in the next section.

Gypsum dissolution via the reaction



can occur in the buffer and provides a source of sulphate. The sulphate will be available for microbial reduction to sulphide if it migrates to a location in which microbes are active. Thus

- ▲ Treat gypsum as a source of sulphate in the buffer.

Ion exchange is simulated in the bentonite and gel. In the first instance only Na-Ca exchange is considered since these are the only species of the larger Na-Ca-Mg-K system, which is more typically considered, that take part in the other chemical reactions under consideration. Thus:

- ▲ Consider ion exchange for the Na-Ca system.

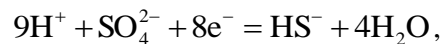
Cl^- reactions are excluded from the first set of calculations; they are only relevant in highly reducing systems, when Cu^+ dominates Cu^{2+} . However, Na^+ and Cl^- are represented in the modelling to allow solutions to be charge balanced with a specified ionic strength.

Cement waters (e.g. from grouted fractures in tunnel that meet with deposition hole fractures or EDZ) are not considered.

The chemical system to be modelled comprises the species: sulphide, sulphate, Ca, Na, Fe, H with Cl for ionic strength specification and charge balance. A minimal set of aqueous complex species is considered to limit the number of variables in the simulations.

4.5 Microbial Processes

The sulphate reduction reaction can be expressed in electron balance form as:

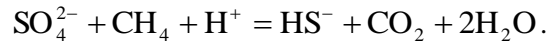


or equivalently, by using the standard hydrogen half cell reaction $2\text{e}^- + 2\text{H}^+ = \text{H}_{2(\text{g})}$, as



The H_2 fugacity in this model could either be imposed on the system or solved for (together with the $H_{2(aq)}$ concentration). In either case, in-situ f_{H_2} would be bounded by the measured f_{H_2} values, since hydrogen is consumed in the reaction. (At $12^\circ C$, $\log f_{H_2}$ is related to $\log f_{O_2}$ by $\log f_{H_2} \approx -46.6 - 0.5 \log f_{O_2}$, using data from [12]).

An alternative representation of the microbial sulphate reduction reaction that uses the CH_4 energy source is:



Using this form of the reaction, the CH_4 energy source would need to be included in the simulations in the same way that H_2 was treated in the earlier reaction (i.e either imposed as a constant or treated as a limiting factor in the reaction). Additionally, the CO_2 product would also need to be included in the simulations.

The appropriate rate of the microbial reaction as a function of nutrient availability in the relevant environment is not known. The Monod rate expression (see [14]) could be used if it can be suitably parameterised. An alternative approach, which removes the need to consider uncertainties regarding the availability of H_2 or CH_4 , is to treat the microbial reaction simply as a conversion process and ignore the coupling with other chemical species. This is equivalent to assuming that the supply of sulphate is the rate-limiting process. This simplifies the system and allows a simple rate to be used to control the conversion process and is conservative in the sense that availability of energy sources does not limit the reaction. Thus the approach used is to:

- ▲ Treat microbial processes using a simple rate of conversion.

A simple linear rate law is adopted and the rate constant is explored through a sensitivity study. The reaction is assumed to be possible at any location where microbes are “active”, which is interpreted to mean anywhere in the system where microbes are present and where the bentonite density is sufficiently low that microbial activity is assumed to be possible; this can include the fracture if microbes are assumed to be present.

4.6 Bentonite Redistribution

In the current modelling study, bentonite redistribution is simply viewed as a mechanism by which heterogeneous density fields that develop in the bentonite due to erosion are “re-homogenised”. In such a heterogeneous state, regions of enhanced diffusion (or possibly advection) of sulphide to the canister surface will be present that will “heal” to some extent as the density field is made uniform by mass redistribution. The rate of redistribution will control the length of the periods for which enhanced transport regions exist, with a zero rate corresponding to an inability to heal

following erosion. The modelling does not aim to represent the rate or pattern of redistribution in detail because the main aim is to investigate the effect of heterogeneous density fields in the bentonite rather than their cause.

The primary driving force for mass redistribution is a change in stress state. It is assumed that the dominant cause of change in stress will arise from changes in the characteristics of the bentonite rather than external forces; specifically changes in the swelling due to smectite hydration, erosion of the bentonite causing density change and changes in local bentonite composition through geochemical alteration.

The fundamental idea underlying the simplified representation presented here is that following any loss of mass due to erosion (Section 4.7), the bentonite will attempt to redistribute itself in order to equalise the swelling pressure and arrive at a new equilibrium some time after the period of erosion has ended. Thus the ambition is to simulate the transition towards a new equilibrium state after each glacial cycle, with the rate at which re-equilibration is achieved being controllable. It is likely that the transient behaviour will not be represented as well as by a fully mechanistic model, but since these transients only occur during the glacial period and for a (relatively) short “recovery” period after the glacial cycle, the transient periods will mostly be short in relation to the overall simulation time; hence any effect of the simplification in the transient behaviour is expected to be minimal. If the recovery period is not short compared to the overall simulation time, this implicitly refers to situations in which the bentonite redistribution is slow, in which case the differences caused by the precise nature of the transient are likely to be small (and would obviously tend to zero as controls on the rate of bentonite movement tend to zero in both models). Once it becomes clear which aspects of the redistribution are most significant, further developments in the modelling approach may be appropriate.

The mechanical model for bentonite employed in the relevant QPAC module (see [4] and references therein) is complex, with compacted bentonite assumed to behave as a poro-elastic-plastic body at low water contents, then moving towards a poro-visco-elastic (Maxwell) body at increasing water contents. At the higher water contents where the bentonite becomes gel-like the bentonite is represented as behaving more like a viscous fluid than an elastic-plastic body because the elastic limit to viscous movement is extremely low and hence almost any applied stress will induce viscous movement. It is expected that this 'viscosity' will be relatively high in the fully hydrated, confined conditions to be expected immediately after resaturation and will decrease as the local water content increases.

Given the high hydration state considered and the fact that the primary objective is to represent the large-scale movement of buffer material, rather than using the full elastic-viscous model [4, 15], a simplified viscous flow model is judged to provide an adequate approximation. Stress is assumed to be isotropic (as in a viscous fluid) and hence is conceptually identical to a fluid pressure. Changes in local stress state are calculated from changes in bentonite density and the 'flow' of bentonite is taken to be proportional to the stress gradient divided by the bentonite 'viscosity'. The key advantage of

this approach is that it is conceptually considerably simpler than a full mechanical model and need not address issues relating to extreme grid deformations associated with large strains. The disadvantages are that conventional elastic or plastic processes are not represented, but for the system that is simulated this is not considered to be a problem. It should be noted that it is conceptually possible to couple the viscous transport model outlined above with the mechanical model used previously, to utilise the key advantages of both approaches in a single model - such an approach may be useful in future work and would enable the impact of the approximations made in the current modelling to be quantified.

Redistribution within the bentonite gel is a different non-Newtonian fluid flow process, but a minor modification to the redistribution model discussed above to inhibit indefinite extrusion into fractures is expected to provide an adequate description for the current purposes.

In summary, the bentonite redistribution can be thought of as arising from the non-uniform density and bentonite composition fields, with the density variation being of primary interest. The following approach is used:

- ▲ The redistribution process is characterised solely by density differences.

At each internal interface in the buffer the redistribution process is represented by inferring a potential swelling pressure on each side of the interface. The rate of redistribution is controlled by viscosity, which is initially imposed, allowing a range of response rates to be considered. In the simulations:

- ▲ The bentonite viscosity parameter is imposed.

Details of the mathematical model used to simulate bentonite redistribution are given in Section 6.

4.7 Erosion

Bentonite erosion is assumed only to take place when glacial meltwaters are in contact with the bentonite. Glacial meltwater periods are imposed externally through a change in boundary conditions (Section 5) but the residence of meltwaters in the buffer is controlled by the buffer transport properties and so may persist beyond the end of the glacial period. Periods of glaciation are assumed to last for 10^4 years and occur with frequency on the order of 10^5 years (Section 5.3). Porewater compositions of glacial meltwaters are discussed in Section 5.1.

Bentonite erosion will occur at locations where bentonite is in contact with flowing dilute groundwater and is represented as a process that converts solid bentonite to colloidal bentonite that can be transported in porewater. Locations at which erosion is possible are characterised by high (solid) bentonite density on one side of the interface and low on the other (where there is effectively no bentonite in the solid phase). Hence the bentonite

transfer here can be represented as a loss term from the high density side and a source term (of bentonite colloids) to the low density side.

Initially the location for erosion will be at the extremity of the bentonite gel / porewater interface in the fracture, but extreme erosion cases could cause removal of bentonite back towards and into the buffer, which could lead to advective conditions in cavities or low density zones in the buffer. In the subsequent modelling here we use the term cavity to denote a region with low enough density to allow significant advective flow.

In the buffer, erosion is possible at locations where solid bentonite neighbours “open” porewater and hence satisfies the same basic erosion condition. Erosion in the buffer has not yet been studied in detail by SKB. SKB’s modelling to date has considered only erosion in the fracture at the tip of the extruded bentonite gel (see [6] and the references therein) with any impacts on the bulk loss rates in the buffer being upscaled from the loss rates derived in the fracture. The assumption of continued erosion in the buffer in this study has been made so that cavities can potentially form in the buffer, and hence allows the possible effects of advective conditions in the buffer to be investigated.

The bentonite solid to colloidal bentonite loss is characterised in the following way in the modelling:

- ▲ Assume a constant colloidal loss term ($\text{kg m}^{-2} \text{y}^{-1}$) when conditions for erosion are satisfied (i.e. meltwaters are present).

Rates are taken in the first instance from SKB’s work [6]. The rates that are quoted are for mass loss of bentonite gel and are expressed (in Table 9-2 of [2]) as a function of groundwater velocity. For simulations in which slow redistribution of the bentonite leads to an inability for the buffer swelling pressure to maintain an intrusion of gel into the fracture, groundwater will come into contact with non-gel buffer material. In this case, basing the erosion process on the gel model may lead to more rapid erosion than is realistic and hence the rate of cavity formation may be overestimated.

If flow in the fracture is assumed to be channelled (i.e. when the entire fracture is not available for flow) or when piping is assumed to have occurred at the buffer/rock interface, the erosion location will act more like a point, but this will arise as a natural consequence of the flow field.

4.8 Bentonite Gel Extrusion

The extrusion of bentonite gel into the fracture is modelled using a minor modification to the simplified bentonite redistribution model (Sections 4.6 and 6). This modification is needed to prevent transport of buffer material into the fracture over unlimited distances (due to the diffusion-like implementation of the process) and instead cause the gel front to halt at a controlled distance from the buffer. Erosion at the gel / fracture porewater interface will cause the distance of bentonite intrusion into the fracture to recede. This will be balanced by the redistribution model if the

redistribution rate is sufficiently fast or will cause the penetration distance to shorten if the rate is slow.

If the penetration distance reduces to zero erosion may continue within the buffer. This process has not yet been studied in detail by SKB. As previously indicated, SKB's modelling to date has considered only erosion in the fracture at the tip of the extruded bentonite gel. If the erosion front penetrates the deposition hole region, then the nature of the available surface area for erosion differs (changing from a narrow band to an extended area) and it is therefore possible that the net rates of buffer erosion could be quite different.

4.9 Groundwater Flow

Fully saturated groundwater flow is represented throughout the system. Flow is negligible in the intact buffer due to its low permeability, but in the fracture and in any cavities, flow will be more rapid (advection will dominate diffusion). Since the permeability of a given location in the system can change with time, it is necessary to infer the permeability at any given location as a function of the density of the bentonite. If the density is zero (i.e. there is no bentonite) the location will behave like the open fracture, but if bentonite is present, the permeability will depend on the density.

4.10 Groundwater-mediated Transport

Advection and diffusion of all transported chemical species are represented throughout the system (although advection will be negligible in regions where high-density bentonite is present).

The fracture is treated as a uniform aperture. In [1], it was concluded that random aperture variations could be ignored but that channelling could be important. The effects of channelling are ignored in the present study.

4.11 Spalling

Spalling is a consequence of the local stress field around the deposition hole, leading to fracturing of the host rock, and hence enhanced hydraulic conductivity, near the deposition hole surface. If spalling occurs in the vicinity of the fracture this may lead to enhanced flows across a wide area of the deposition hole surface, reducing the transport resistance associated with the buffer/fracture interface, as indicated in [1]. In the current study, spalling is not considered.

5 External Factors

The external factors that drive the evolution of the system described in the previous sections are implemented as time-dependent boundary conditions. These are discussed below.

5.1 Groundwater Chemistry

The incoming groundwater composition will vary with time according to whether the water arises from glacial or non-glacial sources. Glacial sources in particular and surface sources in general would tend to have a lower ionic strength, while deeper water sources and sea-water intrusion could lead to higher ionic strength groundwaters. To specify the boundary conditions, groundwater compositions for the both of these periods must be specified [16]. There is some evidence that glacial meltwaters may be higher in sulphate than the Grimsel water used by SKB. This implies that during the erosion period, perhaps before the buffer has had much chance to redistribute, the invading water might allow corrosion to continue – assuming that microbial activity continues whilst these waters are present.

The concentration of divalent cations in the glacial water will introduce a “pulse” into the ion-exchange profile in the buffer system that will most likely recover when the meltwater recedes. Furthermore, the divalent cation concentration is the factor that initiates the destabilisation of the bentonite to form colloids and is related to bentonite stability through the critical coagulation concentration (CCC). In this first phase of investigation the erosion process is not modelled in sufficient detail to relate the erosion rate to the CCC, but in future studies it could be considered.

SKB use the Grimsel meltwater as a typical glacial meltwater composition. Recent data compiled by Arthur [17] suggests that the Grimsel water may be lower in divalent calcium ion content than is found in measurements of other glacial waters and therefore that calculations of expected amounts of erosion may be pessimistic when using this water. For the calculations presented in this study, whose focus is on investigating the potential for uneven corrosion of the canister surface due (primarily) to bentonite erosion, the Grimsel meltwater is used because it is likely to lead to conditions where more erosion would be seen. However, it is acknowledged that the calculated amounts of erosion, especially within the buffer, may be pessimistic.

5.2 Flow rates

The hydraulic head is specified on the outer edges of the fracture in order to impose a range of flow rates in the fracture that are at least as wide as those quoted by SKB [2]. Flow rates within the buffer will initially be (effectively) zero, but erosion may cause the net permeability to be altered.

Head boundary conditions may vary with time between glacial and non-glacial periods. For example the local topographical gradient is $\sim 30 \text{ m}/3 \text{ km} = 0.01$ [7]. However, at the tail of a retreating glacier, surface elevations may vary by 1 km over a distance of around 5 km giving a topographical gradient of 0.2. Periods of glacial retreat will be present for only a fraction of the glacial period and so these elevated flow rates would not in reality be expected to persist over the entire glacial period. However, for simplicity, the conservative assumption that glacial flow rates will be constant at the maximum value for the duration of the glacial period is made.

Hence

- ▲ A range of fracture flow rates can be investigated and flow rates varied between glacial and non-glacial periods.

SKB relate fracture transmissivity to aperture using a quadratic Doe's law, $a = \zeta T^{1/2}$, with $\zeta = 0.5 \text{ s}^{1/2}$ (e.g. [18]). For example, a fracture with transmissivity $10^{-8} \text{ m}^2/\text{s}$ has an equivalent aperture of $0.5 \times 10^{-4} \text{ m}$ and an equivalent hydraulic conductivity of $2 \times 10^{-4} \text{ m/s}$.

This approach is used to cover a range of fracture transmissivities from $10^{-6} \text{ m}^2/\text{s}$ (worst likely case) to $10^{-11} \text{ m}^2/\text{s}$ into equivalent fracture hydraulic conductivities for use in the models. When combined with the head gradients suggested above, these transmissivities lead to equivalent Darcy velocities in the fracture in the range $2 \times 10^{-5} - 2 \times 10^{-7.5} \text{ m/s}$ during non-glacial periods, and in the range $4 \times 10^{-4} - 4 \times 10^{-6.5} \text{ m/s}$ during periods of glacial melting, as shown in Table 5-1. Note that the values are written with fractional powers to emphasise the square root relationship with transmissivity.

Table 5-1 Fracture hydraulic conductivities and resulting Darcy velocities for topographical and receding glacier flows

$T \text{ (m}^2/\text{s)}$	$a \text{ (m)}$ (using $a = \zeta T^{1/2}$)	$K \text{ (m/s)}$	$K\nabla h \text{ (m/s)}$ ($\nabla h = 0.01$)	$K\nabla h \text{ (m/s)}$ ($\nabla h = 0.2$)
10^{-6}	5×10^{-4}	2×10^{-3}	2×10^{-5}	4×10^{-4}
10^{-7}	$5 \times 10^{-4.5}$	$2 \times 10^{-3.5}$	$2 \times 10^{-5.5}$	$4 \times 10^{-4.5}$
10^{-8}	5×10^{-5}	2×10^{-4}	2×10^{-6}	4×10^{-5}
10^{-9}	$5 \times 10^{-5.5}$	$2 \times 10^{-4.5}$	$2 \times 10^{-6.5}$	$4 \times 10^{-5.5}$
10^{-10}	5×10^{-6}	2×10^{-5}	2×10^{-7}	4×10^{-6}
10^{-11}	$5 \times 10^{-6.5}$	$2 \times 10^{-5.5}$	$2 \times 10^{-7.5}$	$4 \times 10^{-6.5}$

5.3 Frequency of Glaciation

Periods of glaciation are assumed to occur for durations of around ten thousand years with a frequency of glacial cycles of around 100,000 years. The period of glacial retreat is assumed to be a few thousand years and it is during this period that flow and geochemical boundary conditions are perturbed to represent glacial influences. The period of glaciation would likely lead to altered (reduced) flow conditions in the system, but this has not been represented in the simulations. Permafrost conditions would also lead to reduced flows, but such conditions are not considered in the simulations.

The potential for damage to the buffer to accumulate over several glacial cycles is of interest, as is the potential for the buffer to partly self-heal during the interglacial periods.

- ▲ Glacial and inter-glacial periods can be imposed on the system by varying the composition of the boundary water with time.

As noted in Section 5.2, periods of glacial retreat may correspond to elevated groundwater flow rates due to the increased head gradient as the glacier retreats across the site. These periods of retreat will be shorter than the overall glacial period and so their effect will not persist for the duration of the imposed glaciation period. However for simplicity, the conservative assumption that glacial flow rates will be constant at the maximum value for the duration of the glacial period is made.

6 The Simplified Buffer Redistribution Model

As discussed in Sections 3.1, 3.2 and 4.6, bentonite redistribution following loss of mass due to erosion is modelled in a simplified fashion. Bentonite redistribution is simply viewed as a mechanism by which heterogeneous density fields that develop in the bentonite due to erosion are “re-homogenised”. During the heterogeneous state, regions of enhanced diffusion (or possibly advection) of sulphide to the canister surface will be present that will “heal” to some extent as the density field is made uniform by mass redistribution and the rate of redistribution will control the periods for which these regions exist. The model does not aim to represent in detail the rate or pattern of redistribution, because the main aim is to investigate the effect of heterogeneous density fields in the bentonite rather than their cause.

The redistribution process is also used to simulate the ingress of bentonite into the fracture. It is necessary to simulate this process because bentonite erosion is assumed (initially) to take place at the tip of the intruded bentonite where low density bentonite sol is in contact with dilute water in the fracture. In SKB’s modelling to date, all erosion is assumed to take place at this location, with the bentonite in the buffer able to respond and redistribute itself at a rate that balances the rate of erosion [19]. In the model presented here, the ability for the bentonite to balance the erosion rate can be controlled with a rate parameter. With a small value for this parameter, balancing of erosion is not possible and the bentonite will recede towards the buffer and into the deposition hole while the bentonite “edges” are in contact with dilute water. If a zero redistribution rate is set, the bentonite never recovers, whilst with a small value it will only begin to recover when the dilute water is replaced by less dilute waters after glaciation has ceased.

The primary driving force for mass redistribution is a change in stress state. It is assumed that the dominant cause of change in stress will arise from changes in the characteristics of the bentonite rather than external forces, specifically changes in the swelling pressure due to density changes following erosion of the bentonite and changes in local bentonite composition.

The model described here is intended to reproduce plausible responses of the buffer to density variation and to simulate the process of extrusion adequately without the need for complex algorithms. The details of the processes used to achieve this should therefore not be considered definitive and would be subject to change if further modelling studies were undertaken.

It is assumed that bentonite redistribution can be represented approximately by a viscous flow-like process, in which a bulk solid (smectite - the swelling phase) carries minor non-swelling phases as it moves. The redistribution of smectite is described by a nonlinear diffusion equation of the form

$$\begin{aligned}\frac{\partial \rho_{sm}}{\partial t} &= \nabla \cdot \mathbf{q}_{sm}, \\ \mathbf{q}_{sm} &= -D_{sm}(\rho_{sm}) \nabla f(\rho_{sm}).\end{aligned}$$

Here, ρ_{sm} (kg m^{-3}) is the dry density of smectite, \mathbf{q}_{sm} ($\text{kg m}^{-2} \text{s}^{-1}$) is the smectite flux, D_{sm} ($\text{m}^2 \text{s}^{-1}$) is a redistribution rate function and f (kg m^{-3}) is the “homogenisation function”.

The homogenisation function controls the distribution of smectite density at equilibrium. It is necessary because bentonite behaves differently in different regions of the system. Within the buffer it is assumed that bentonite is redistributed in order to equalise its density (a proxy for swelling pressure). If the same assumption were made in the fracture, the model would predict that bentonite could move infinitely far into the fracture. In order to impose a bentonite density that falls as we move further into the fracture we impose a rule of the form

$$f(\rho_{sm}) = (r/r_{buf})^n \rho_{sm},$$

where r (m) is the distance from the centre axis of the system and r_{buf} (m) is the radial extent of the buffer (i.e. the radius at the buffer/fracture interface). Taking $n > 1$ it is evident that the bentonite density must fall with distance when at equilibrium (when $\nabla f(\rho_{sm}) = 0$). The rate at which the bentonite density falls with radial distance will increase with increasing n . This rule is purely a modelling convenience to simplify treatment of the extruded bentonite and is not intended to represent directly any particular process.

The redistribution rate function, $D_{sm}(\rho_{sm})$, is taken to depend on the swelling pressure at the given density. The form

$$D_{sm}(\rho_{sm}) = D_{sm,1700} \alpha(\rho_{bent}) H(\rho_{bent} - \rho_{bent,\min})$$

is taken for this function, where $D_{sm,1700}$ is the redistribution rate at a bentonite dry density of 1700 kg/m^3 , $\alpha(\rho_{bent})$ is a scaling function for bentonite densities below 1700 kg/m^3 , based on measured data, and $H(\rho_{bent} - \rho_{bent,\min})$ is a Heaviside function, resulting in a zero redistribution rate for bentonite densities below $\rho_{bent,\min} \text{ kg/m}^3$, which helps to control the “falling off” of bentonite density at the tip of the extruded material in the fracture.

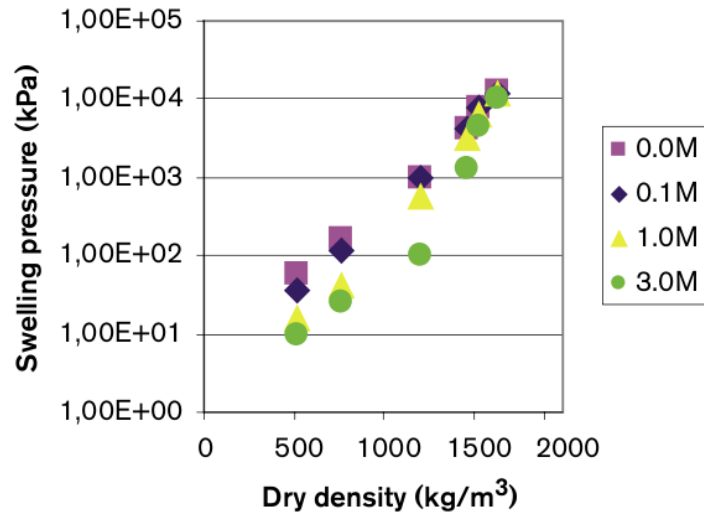


Figure 6-1 Variation of bentonite swelling pressure with bentonite dry density (from [9] Fig 5-3 (b))

Figure 6-1 (from [2] Fig 5-3) suggests that bentonite swelling pressure falls by around 3 orders of magnitude when the bentonite dry density drops from 1700 to 500 kg/m³. This log-linear scaling has been used to derive a relationship for the scaling function $\alpha(\rho_{bent})$. The redistribution rate at 1700 kg/m³ ($D_{sm,1700}$) is scaled by

$$\alpha(\rho_{bent}) = 10^{-3 \left(\frac{\rho_{bent} - 500}{1700 - 500} \right)}$$

Only the homogenisation function is taken to vary between the buffer and fracture regions, thus the redistribution equations in these two regions are coupled by an internal boundary condition that ensures continuity of \mathbf{q}_{sm} across the internal boundary.

Numerical experiments with the model have shown that the parameterisation $n = 4$, $D_{sm,1700} = 10^{-9}$ m²/s and $\rho_{bent,min} = 1000$ kg/m³ gave rise to plausible density profiles in the fracture, as shown in Figure 6-2. With this choice of parameters, the smectite density falls from around 1440 to 900 kg/m³ (smectite is assumed to occupy 87 wt% of the bentonite [8]) over the first 15 cm of the intruded material, with dry density rapidly falling off beyond this distance. The time taken for bentonite to intrude this far is around 10 years for this choice of parameters. The time taken can be controlled by modifying the $D_{sm,1700}$ parameter.

The coupling of the bentonite intrusion and the response in the buffer, which effectively imposes a boundary condition on the intruding material, is shown in Figure 6-3, which shows the variation in time of the smectite dry density in a buffer compartment adjacent to the fracture. Taking an initial buffer dry

density of 1655 kg m^{-3} [9] gives an initial smectite dry density of 1440 kg m^{-3} . The amount of variation is small, but the initial reduction in density as bentonite is extruded into the fracture and the subsequent recovery can be seen.

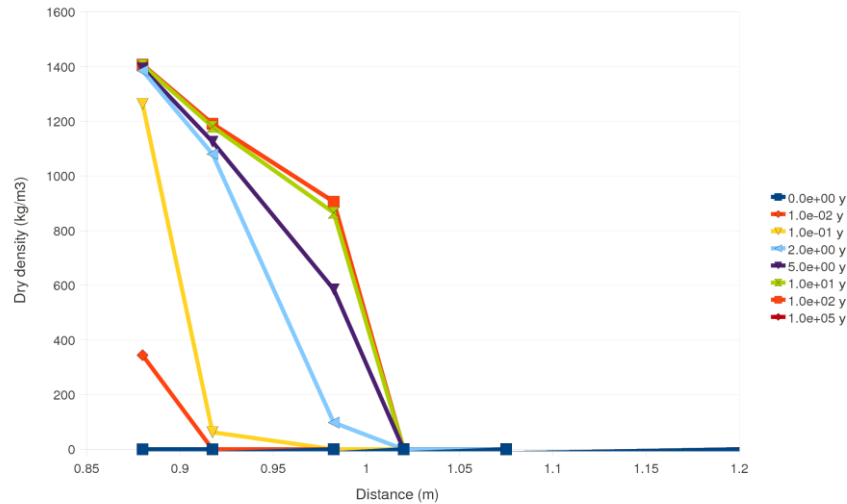


Figure 6-2 Smectite dry density in the fracture (Equalisation rate $D_{sm} = 10^{-9} \text{ m}^2/\text{s}$). The deposition hole / fracture interface is at a radial distance of 0.875 m.

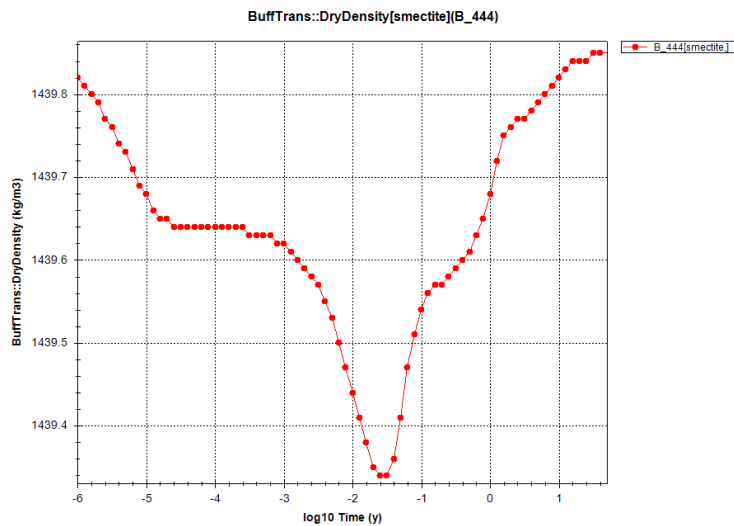


Figure 6-3 Response of smectite dry density in the buffer compartment adjacent to fracture. The degree of variation is small, but the initial reduction during ingress and recovery is visible. (The total bentonite density is 1655 kg/m^3 ; the smectite initial density is 1439.85 kg/m^3 (87 wt%).)

7 The Erosion Model

A simple erosion model has been implemented that converts solid smectite to colloidal smectite at a controllable rate that can depend on any other quantities of interest in the system. For example, in future, a CCC-based model could be implemented by writing the rate as a function of the Ca^{2+} concentration in the porewater.

QPAC represents spatial discretisations using compartments and interfaces [20]. Compartments can represent volumes into which space is subdivided and interfaces describe the connectivity between compartments in terms of the common area that is shared between compartments (Figure 7-1). Mass transfers are represented as fluxes across interfaces from one compartment to another, with one compartment being labelled as the “from” compartment and the other being labelled as the “to” compartment although this does not necessarily indicate the direction of mass transfer (since fluxes can be negative). By default, QPAC conserves mass locally in the model by ensuring that the mass entering a compartment is equal to the mass leaving the neighbouring compartment.

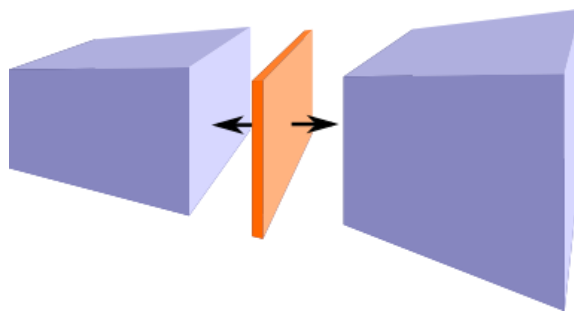


Figure 7-1 Abstract compartments and interfaces model in QPAC

The erosion model is implemented as a process that takes place on interfaces between compartments with solid mass in one compartment being converted to colloidal mass in the neighbouring compartment. The rate at which the conversion takes place can be expressed in terms of quantities in the compartments on either side of the interface.

7.1 Verification with a simple constant erosion rate

We express the bentonite erosion rate as a constant that depends only on whether there is solid mass of smectite in one of the compartments that sit either side of an interface. A colloid solubility-based model of erosion is presented in Section 7.2. Models of bentonite erosion such as those

presented here are possibly more conservative than some presented by SKB [19] and earlier QPAC modelling work [4] where the erosion rates are controlled by the CCC and by rates at which the CCC can be buffered by mineral dissolution.

The erosion model works by examining the conditions on either side of the interface. When there is a non-zero solid mass of smectite on both sides of the interface, the interface is located implicitly within the interior of the buffer (or gel) and so no erosion takes place. Erosion only occurs at locations where bentonite is in contact with water, hence the rate is taken to be non-zero at locations where a non-zero solid mass of smectite is present on one side of the interface only. This is shown schematically in Figure 7-2.

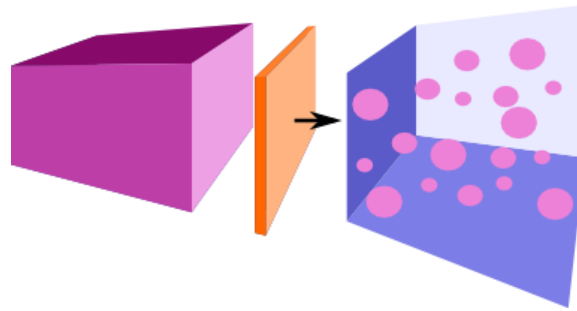


Figure 7-2 Conceptual model for bentonite erosion. Interfaces between compartments containing bentonite (left) neighbouring “open water” compartments (right) can act as locations for erosion, with loss of solid mass in the bentonite compartment and a corresponding increase in colloids in the porewater.

On any interfaces where erosion can take place, the rate of colloidal loss is taken to be a constant mass loss rate per unit area. The rate can therefore be expressed as

$$R = k_{erode}A \quad (7.1)$$

where A (m^2) is the area of the interface and k_{erode} ($kg\ m^{-2}\ s^{-1}$) is given by

$$k_{erode} = \begin{cases} \mu_{erode} & m_{smec,from} > 0 \text{ and } m_{smec,to} = 0 \\ & \text{or } m_{smec,from} = 0 \text{ and } m_{smec,to} > 0, \\ 0 & \text{otherwise.} \end{cases}$$

Here $m_{smec,from}$ and $m_{smec,to}$ (kg/m^3) are the dry densities of smectite on the “from” and “to” sides of the interface and μ_{erode} ($kg\ m^{-2}\ s^{-1}$) is the erosion rate, which is taken to be a constant in this example calculation, although will depend on whether glacial conditions persist in the simulations.

Smectite is removed from the solid phase in the relevant compartment and colloids are introduced into the aqueous phase in the neighbouring compartment and are transported in the groundwater. Colloids are not transported into the bentonite.

The bentonite redistribution model in this example calculation is parameterised as in Section 6. In particular, $D_{sm,1700} = 10^{-9} \text{ m}^2/\text{s}$. For this choice, without erosion the bentonite penetration into the fracture would reach a distance of around 15 cm into the buffer (see Figure 6-2). μ_{erode} is taken to be $10^2 \text{ kg m}^{-2} \text{ y}^{-1}$. Note that no attempt has been made to relate this value directly to experimental measurements.

There is a balance between the rate at which bentonite is eroded and the rate at which it can redistribute itself to replace the lost material. To allow time for the gel to penetrate the fracture in the simulation the erosion model does not become fully active until 200 y into the simulation (it is steadily increased in the simulation from $0 \text{ kg m}^{-2} \text{ y}^{-1}$ at 10 y to μ_{erode} at 200 y).

Figure 7-3 shows the smectite dry density in the compartment corresponding to the outermost downstream point of the gel penetration in the fracture in the calculation in Section 6 (which spans $r=0.95$ to $r=1.015$ m). The dry density at this location is initially zero, then increases as gel penetrates the region. When the erosion rate becomes active (after 10 y) bentonite begins to be removed, until the compartment is depleted of bentonite by around 50 y. Since the rate of removal is dependent on the exposed surface area of bentonite (as approximated by the interface area between adjacent compartments) it is possible that there will be a point in the fracture where the rate of erosion is balanced by the rate at which bentonite can redistribute.

A similar plot for the compartment that is adjacent to the one just discussed, in the inwards direction towards the buffer (which spans $r=0.885$ m to $r=0.95$ m) is shown in Figure 7-4. In this compartment a balance of erosion and redistribution is achieved, resulting in a dry density in this compartment around 250 kg m^{-3} (it is at the tip of the gel and hence has a low density – the next compartment inwards has bentonite with a dry density of around 1400 kg m^{-3}). A plot of the bentonite density distribution in the fracture is shown in Figure 7-5 (which is not drawn to scale). Figure 7-6 shows the corresponding distribution of colloids in the fracture for this model at 10^5 y. Colloids are only present in compartments outside the regions comprising bentonite gel.

The transmissivity of the fracture in this case is $10^{-9} \text{ m}^2 \text{ s}^{-1}$. Using the Doe law (Section 5.2) the aperture of the fracture is $1.6 \times 10^{-5} \text{ m}$. Since the balance between erosion and redistribution is achieved at a radius of 0.95 m (see above), the surface area over which erosion takes place once the system is balanced is $9.44 \times 10^{-5} \text{ m}^2$. In the first 2×10^5 y, the constant erosion rate of $10^2 \text{ kg m}^{-2} \text{ y}^{-1}$ will have applied for all but the first 200 y (during which time the erosion rate will have steadily ramped up) and hence the expected amount of material eroded is therefore slightly more than 1 886 kg. The total amount of bentonite that is eroded in the model (which only simulates

half of the system due to symmetry) is 943.3 kg (Figure 7-8). A similar plot for the case when the transmissivity is increased by two orders of magnitude is shown in Figure 7-9. Due to the Doe law assumption, the fracture aperture in this case is ten times larger than when transmissivity was $10^{-9} \text{ m}^2 \text{ s}^{-1}$, which results in approximately ten times as much erosion in the $10^{-7} \text{ m}^2 \text{ s}^{-1}$ case. It is noted that these amounts of erosion are non-physical because there is no controlling factor to limit erosion when colloid concentrations in the porewater become large and also erosion in the models presented here has been independent of the glacial cycle. These points are addressed in Section 7.2.

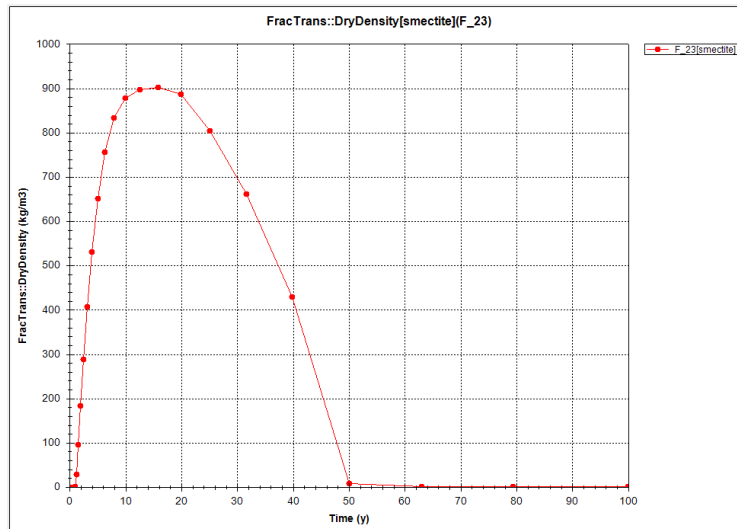


Figure 7-3 Smectite dry density in the downstream compartment between $r=0.95 \text{ m}$ and $r=1.015 \text{ m}$ for constant erosion rate per unit area of $10^2 \text{ kg m}^{-2} \text{ y}^{-1}$ ($T = 10^{-9} \text{ m}^2/\text{s}$, $D_{sm,1700} = 10^{-9} \text{ m}^2/\text{s}$). The dry density is initially zero and then increases as gel penetrates the region. When the erosion rate becomes active (after 10 y) bentonite is removed until the compartment is depleted of bentonite by around 50 y.

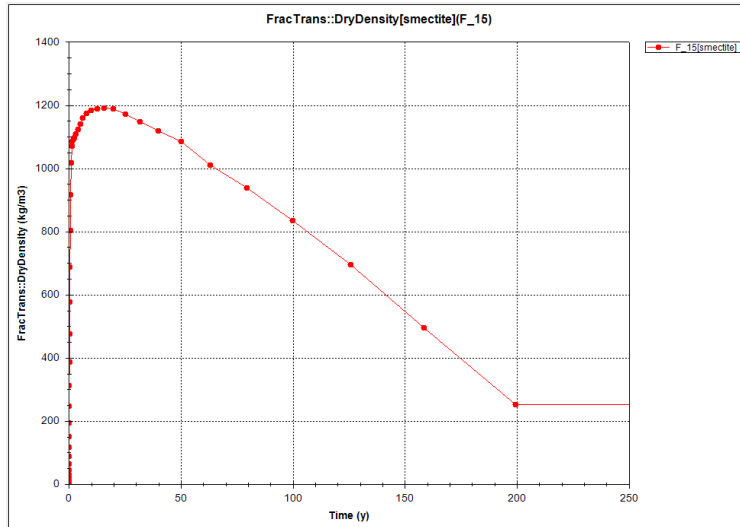


Figure 7-4 Smectite dry density in the downstream compartment between $r=0.885$ m and $r=0.95$ m for constant erosion rate per unit area of 10^2 $\text{kg m}^{-2} \text{y}^{-1}$ ($T = 10^{-9}$ m^2/s , $D_{sm,1700} = 10^{-9}$ m^2/s). The dry density is initially zero and then increases as gel penetrates the region. The erosion rate increases to a maximum between 10 and 200 y, after which time a balance is achieved between intrusion of fresh bentonite and removal by erosion.

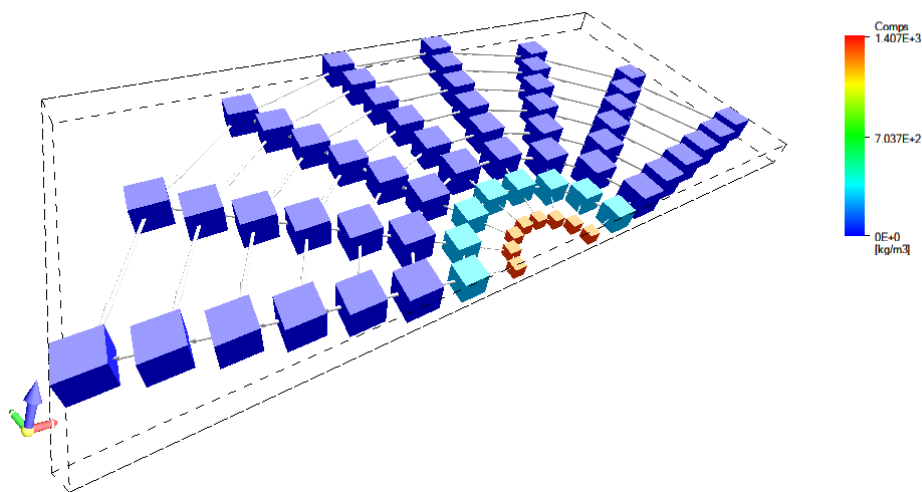


Figure 7-5 Dry density of bentonite (gel) in the fracture a for a constant erosion rate per unit area of 10^2 $\text{kg m}^{-2} \text{y}^{-1}$ (not to scale) ($T = 10^{-9}$ m^2/s , $D_{sm,1700} = 10^{-9}$ m^2/s). The corresponding colloid concentration profile is shown in Figure 7-6.

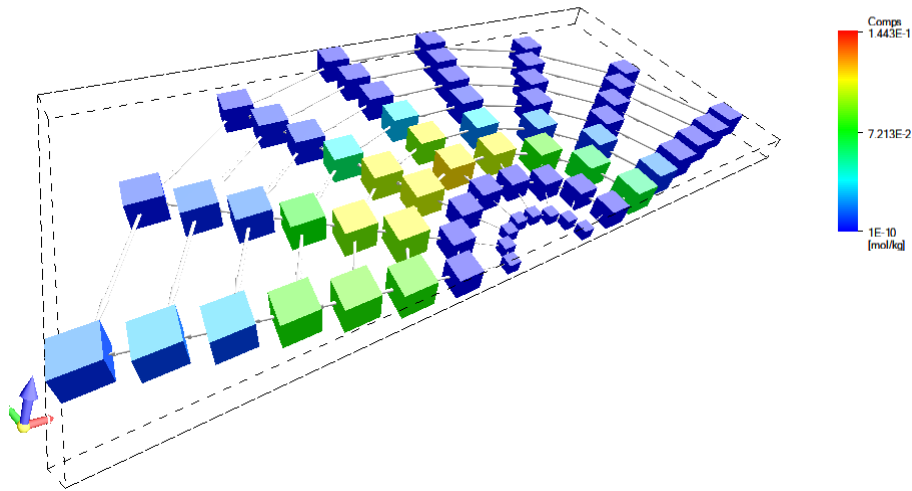


Figure 7-6 Spatial distribution (not to scale – shown to scale in Figure 7-7) of colloid concentrations in the fracture for a constant erosion rate per unit area of $10^2 \text{ kg m}^{-2} \text{ y}^{-1}$. Flow is right to left. ($T = 10^{-9} \text{ m}^2/\text{s}$, $D_{sm,1700} = 10^{-9} \text{ m}^2/\text{s}$). Colloids are released from the gel interface into the porewater (the location of the gel is shown in Figure 7-5). Colloid concentrations are highest at the point at which flow is parallel to the tangent to the gel. Concentrations become smaller as colloids diffuse away from the gel. No colloids are present in the regions occupied by gel.

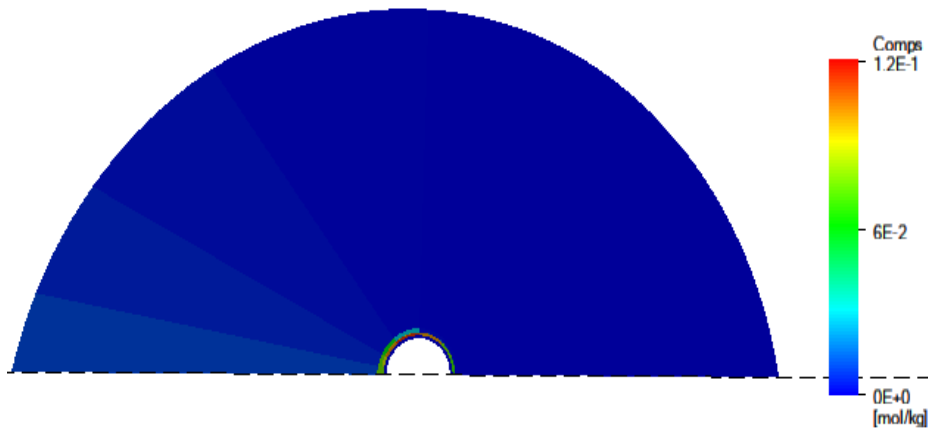


Figure 7-7 Spatial distribution of colloid concentrations in the fracture for a constant erosion rate per unit area of $10^2 \text{ kg m}^{-2} \text{ y}^{-1}$ (to scale) ($T = 10^{-9} \text{ m}^2/\text{s}$, $D_{sm,1700} = 10^{-9} \text{ m}^2/\text{s}$).

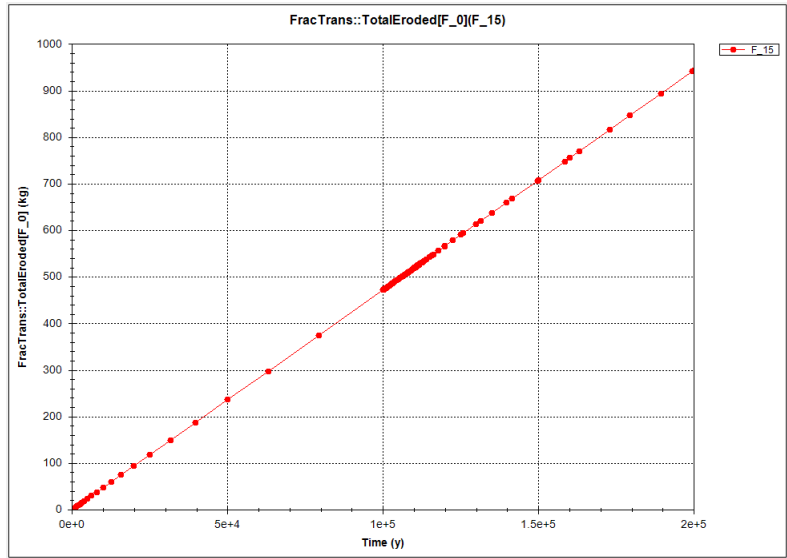


Figure 7-8 Total amount of material eroded in the example calculation (with fixed erosion rate of $10^2 \text{ kg m}^{-2} \text{ y}^{-1}$)
 $(T = 10^{-9} \text{ m}^2/\text{s}, D_{sm,1700} = 10^{-9} \text{ m}^2/\text{s})$

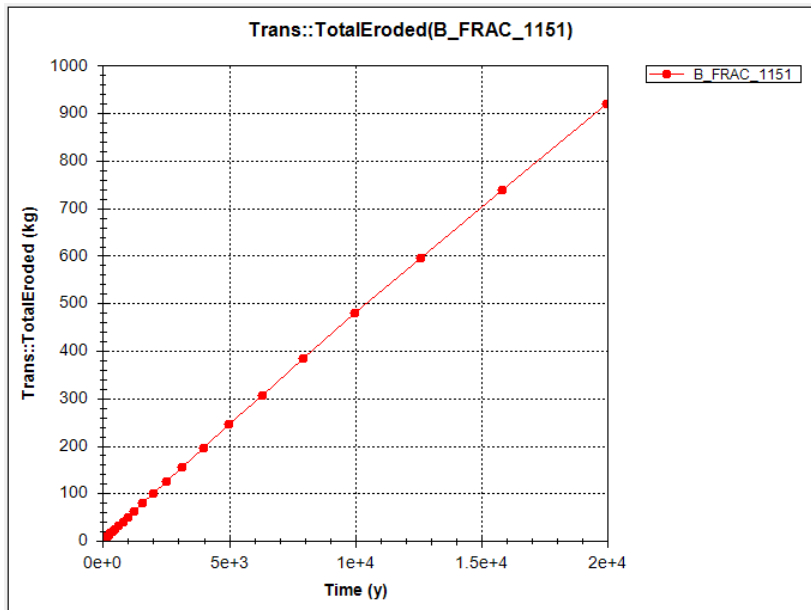


Figure 7-9 Similar plot to Figure 7-8 when the fracture transmissivity is increased by two orders of magnitude
 $(T = 10^{-7} \text{ m}^2/\text{s}, D_{sm,1700} = 10^{-9} \text{ m}^2/\text{s})$

7.2 A Colloid Capacity-Based Erosion Model

The constant erosion rate (per unit area), used in the model in the previous section, leads to non-physical amounts of erosion in regions where the exposed surface area for erosion is large (see for example Figure 7-8). In reality the porewater will only support colloids up to a maximum concentration C_{\max} (kg m^{-3}). SKB take $C_{\max} = 50 \text{ kg m}^{-3}$ [2], which is equivalent to a molality of $0.136 \text{ mol kg}^{-1}$ assuming a montmorillonite unit of $\text{Na}_{.33}\text{Mg}_{.33}\text{Al}_{1.67}\text{Si}_4\text{O}_{10}(\text{OH})_2$, which has a molar weight of 367.01 g/mol . We adopt the 50 kg m^{-3} value but note that the basis for this needs to be reviewed. Equation (7.1) can be revised to account for the maximum colloid concentration in the water by expressing it as

$$R = k_{\text{erode}} A g(C),$$

where $g(\cdot)$ is a function of the in-situ colloid concentration, C (kg/m^3) in the water that should satisfy $g(C) \rightarrow 0$ as $C \rightarrow C_{\max}$. One option is to represent the dependence on C as a hard switch, but this can cause numerical difficulties. Instead a smooth dependence on C is used by writing $g(\cdot)$ as

$$g(C) = 1 - \left(\frac{C}{C_{\max}} \right)^n.$$

In the simulations, the parameter n is taken to be 6, which gives the scaling on erosion rate as shown in Figure 7-10. While $C/C_{\max} < 0.5$ the erosion rate is relatively unchanged (within 98% of the maximum rate), and only falls below half the maximum rate when $C/C_{\max} > 0.89$.

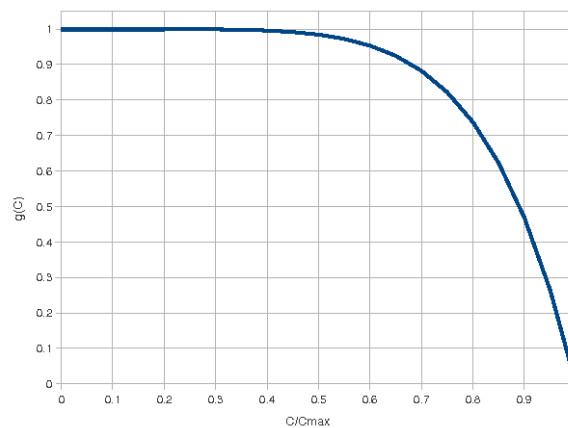


Figure 7-10 Scaling of erosion rate with relative colloid concentration C/C_{\max}

Colloids are transported in the aqueous phase like other aqueous species in the system (e.g. sulphide), but their transport is subject to some restrictions. Colloids are prevented from entering regions in which bentonite is present either diffusively or advectively. In the case of diffusive transport, the effective diffusion coefficient for colloids is given by

$$D_{eff, colloid}(\theta) = (s_{colloid} D_{eff, buff}(\theta) + (1 - s_{colloid}) D_{eff, frac}(\theta)) (1 - s_{colloid})$$

where $D_{eff, buff}(\theta)$ and $D_{eff, frac}(\theta)$ are the effective diffusion coefficients at the in-situ porosity and $s_{colloid}$ is a scaling term indicating whether the location contains sufficient bentonite to resist diffusion of colloids. This scaling term is taken to be

$$s_{colloid} = \begin{cases} \frac{\rho_{dry, smec}}{50 \text{ kg/m}^3} & \rho_{dry, smec} < 50 \text{ kg/m}^3, \\ 1 & \rho_{dry, smec} \geq 50 \text{ kg/m}^3, \end{cases}$$

that is, it is assumed that a dry density of 50 kg/m^3 of smectite is sufficient to resist diffusion of colloids, but this could be updated in future if a more physically-based model were available.

Advection of colloids is treated similarly. A factor of $1 - s_{colloid}$ is applied to the advective flow rate in the downstream direction in the case of colloids to prevent colloids from being advected into regions where bentonite is present.

This model of colloid-limited erosion has been implemented together with an update to the erosion rate, k_{erode} to only allow erosion during glacial periods. Figure 7-11 and Figure 7-12 show the evolution of dry density of the bentonite gel in a fracture with transmissivity $T = 10^{-7} \text{ m}^2/\text{s}$ following the onset of erosion. The same parameterisation of the redistribution model as the models presented earlier in this section was assumed ($D_{sm, 1700} = 10^{-9} \text{ m}^2/\text{s}$).

Gel is completely eroded at distances from 7.5-14 cm in the first 25 y of erosion and is eroded in the range 1-7.5 cm by 100 y. The rheology properties of the buffer slow the rate of erosion of gel in the range 0-1 cm. Unlike the earlier case of the lower transmissivity fracture (Figure 7-4), the rates of erosion and redistribution do not equilibrate over this distance and so reduction in density continues, albeit at a slower rate, as can be seen in Figure 7-12. The reason for this is the surface area for erosion that assumed in equation (7.1) is fixed at the common area between the grid cells (which are stationary).

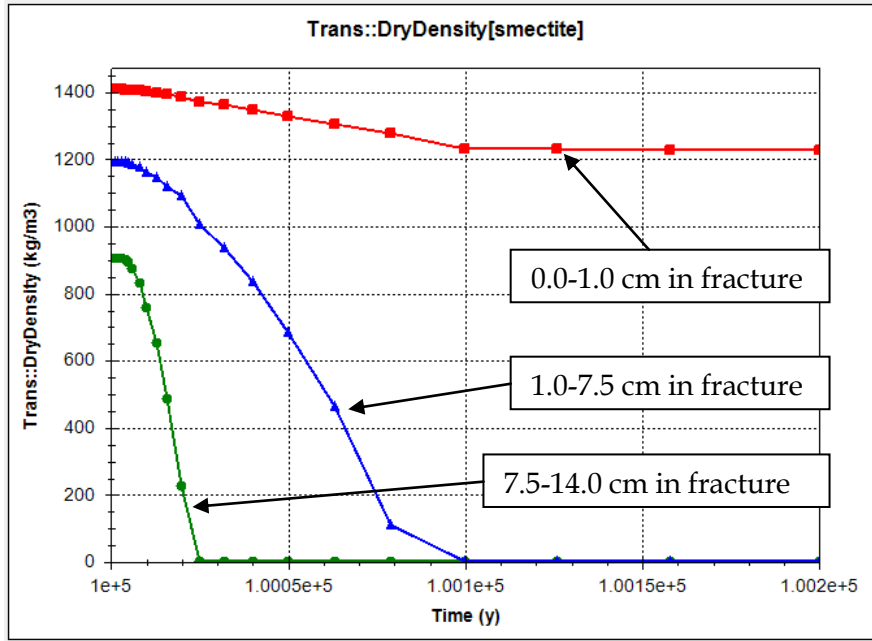


Figure 7-11 Evolution of dry density of gel in the fracture at the onset of the first glacial erosion cycle. Gel is completely eroded at distances of 7.5-14 cm in the first 25 y of erosion and is eroded in the range 1-7.5 cm by 100 y. The rheological properties of the buffer result in the rate of gel erosion being in the range 0-1 cm.

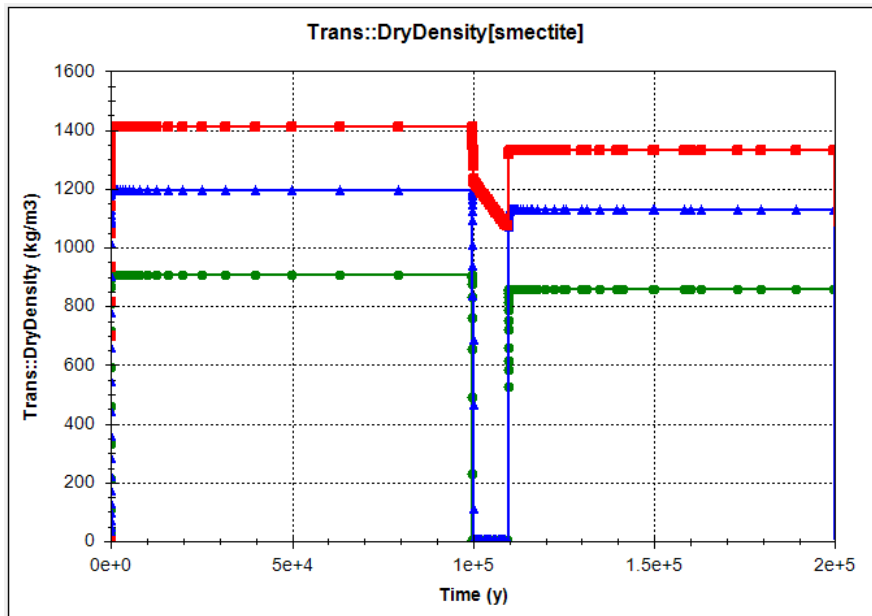


Figure 7-12 As Figure 7-11 - evolution over the first glacial cycle, showing re-intrusion of gel into the fracture at the end of the cycle.

Figure 7-13 shows the total amount of bentonite eroded during the first 2×10^5 y (i.e. to the start of the second glaciation). The absence of erosion during the non-glacial periods is clearly shown and around 475 kg of bentonite is eroded. This is the same amount of erosion as was seen in the non-colloid controlled rate model with the same fracture aperture (Figure 7-9), which suggests that colloid concentrations do not reach the concentration limit in the first 2×10^5 years. Figure 7-14 confirms that this is the case; the colloid concentrations in and neighbouring the eroding cells are always much less than $0.136 \text{ mol kg}^{-1}$.

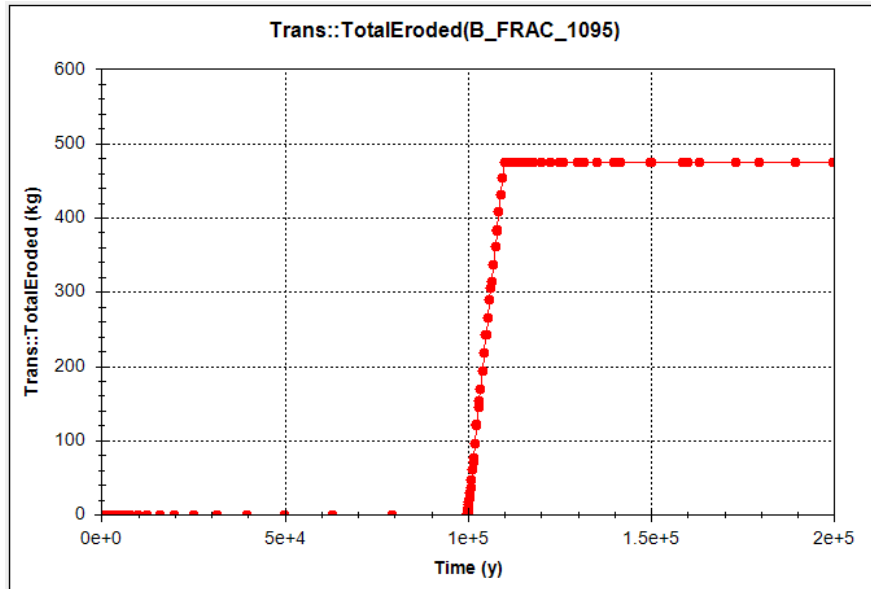


Figure 7-13 Total amount of bentonite eroded as a function of time, during the first 2×10^5 y.

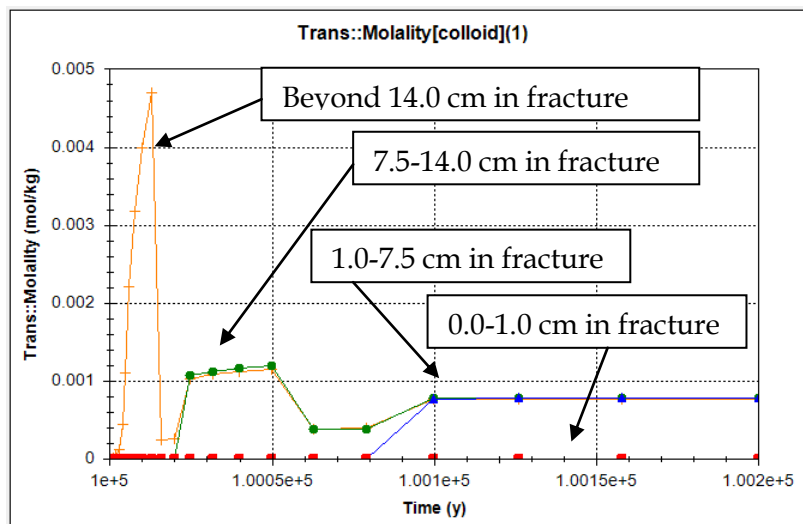


Figure 7-14 Colloid concentrations around the eroding cells shown in Figure 7-11

It is to be expected that the maximum colloid concentration would not be met in this example. The erosion rate is set to be $10^2 \text{ kg m}^{-2} \text{ y}^{-1}$ and the fracture aperture is $a = 0.5 \text{ s}^{1/2} \times \sqrt{T} = 1.6 \times 10^{-4} \text{ m}$. If we assume that the gel is eroded back to the interface with the deposition hole (which is approximately the case after 100 y of erosion, as shown in Figure 7-11), then the surface area for erosion is $2\pi a \times 0.875 = 8.7 \times 10^{-4} \text{ m}^2$ and so the maximal rate of erosion is $8.7 \times 10^{-2} \text{ kg y}^{-1}$. Colloids are transported away in the porewater which, during glacial periods, has a regional head gradient of 0.2. The volumetric flow rate is then $T\nabla hw$ where w (m) is a notional width of flow around the deposition hole. If we assume that the notional flow width is given by the width of the gel region that has been eroded back to the canister surface (i.e. that all colloids are transported around the canister at a maximum distance from the canister equal to this width) then w is around 0.15 m and so $T\nabla hw \approx 0.1 \text{ m}^3 \text{ y}^{-1}$. The colloidal concentration that would balance the erosive supply of colloids with the advective removal is around 0.9 kg/m^3 which has an equivalent molality of $2.5 \times 10^{-3} \text{ mol/kg}$. This calculation is approximate, but suggests that colloidal molalities of the order 10^{-3} mol/kg will balance the rate of erosion and this appears to be the case in Figure 7-14 for cells within 15 cm of the fracture.

Figure 7-15 is the corresponding figure to Figure 7-14 when the transmissivity is reduced by two orders of magnitude (to $10^{-9} \text{ m}^2 \text{ s}^{-1}$) and $D_{sm,1700} = 10^{-11} \text{ m}^2 \text{ s}^{-1}$. The same analysis as above leads to an expected balancing concentration of $0.025 \text{ mol kg}^{-1}$ for flows constrained to lie within 15 cm of the deposition hole as before. If the flow width is reduced to 5 cm, a balancing concentration of $0.075 \text{ mol kg}^{-1}$ is calculated (around half of the concentration limit), which matches the figure well.

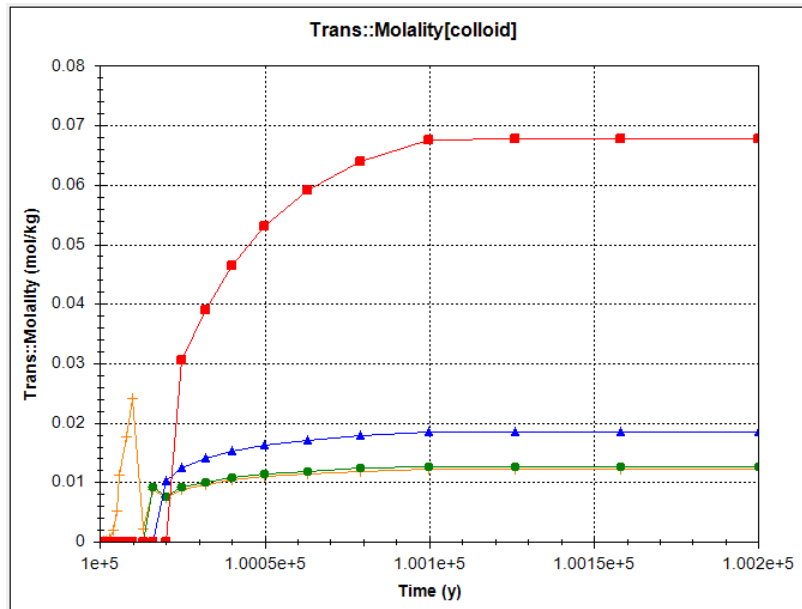


Figure 7-15 As Figure 7-14 when the transmissivity is reduced to $10^{-9} \text{ m}^2 \text{ s}^{-1}$ and $D_{sm,1700} = 10^{-11} \text{ m}^2/\text{s}$

To elevate colloidal concentrations closer to the colloidal concentration limit in regions where transport is dominated by advection it is necessary to either

- ▲ increase the rate of erosion,
- ▲ decrease the transmissivity or flow rate, or
- ▲ include processes to reduce transport, such as filtration or coagulation.

Since transmissivities below $10^{-9} \text{ m}^2 \text{ s}^{-1}$ are towards the lower end of the expected fracture properties, the observations above suggest that it is unlikely that the colloidal concentration limit will be reached unless erosion rates are higher than the rate of $10^2 \text{ kg m}^{-2} \text{ y}^{-1}$ that is assumed here. As will be seen later, this rate leads to overall bentonite losses of around 500 kg per glaciation, which is consistent with the range of rates considered by [2]. Inclusion of other processes from the above list could potentially increase colloidal concentrations. The only other situation in which the concentration might be expected to approach the limit is in regions of the system that are eroding but where advection is not dominant. Such locations are only expected to arise if significant material is eroded within the deposition hole away from the plane of the fracture.

Figure 7-16 shows the amounts of bentonite eroded during the first five glaciations. Over the first four glaciations the amount eroded per cycle reduces slightly. This is due to the net reduction in bentonite density in the buffer. As the density is reduced the swelling capacity of the buffer is reduced so less bentonite is pushed into the fracture for erosion and so it is eroded at distances closer to the buffer where the surface area is smaller, leading to a smaller net erosion rate. After five glaciations the amount of eroded material increases. This is due to the swelling capacity being sufficiently reduced that it is not able to prevent the total loss of gel in the fracture during the glacial period. At this point, glacial waters enter the deposition hole where the available surface area for dissolution increases and so the erosion rate correspondingly increases. We note that the erosion process in this situation may differ from that which applies during the period when bentonite is extruded into the fracture and hence the results obtained here may be an artefact of the modelling assumptions made.

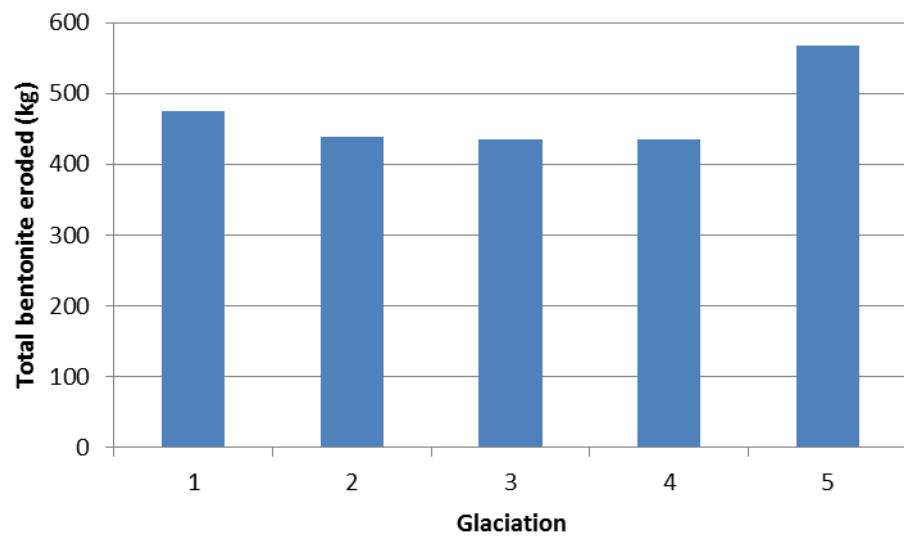


Figure 7-16 Total amounts of bentonite eroded during the first five glaciations when $T = 10^{-9} \text{ m}^2 \text{ s}^{-1}$ and $D_{sm,1700} = 10^{-9} \text{ m}^2 \text{ s}^{-1}$

8 The Base Case Scenario

The base case simulations are for the no-erosion scenario (see Section 2). Since there is no erosion in this case the bentonite mass is fixed and bentonite redistribution only occurs while bentonite is extruded into the fracture. After this time, no further bentonite movement takes place.

Since there is no erosion in these cases there is no opportunity for cavities to form in the bentonite and hence the pathways for sulphide migrating towards the canister surface are time-invariant. Densities are assumed to be sufficiently high inside the buffer to exclude significant microbial activity, so all microbial activity in the model is restricted to the region outside the buffer. For this reason, any elevated sulphide concentration that might be caused by microbial activity outside the buffer can be simulated by artificially increasing the concentration of sulphide in the porewater boundary condition. The advective transport conditions in the fracture mean that any errors introduced by effectively moving the SRB sulphide source to the boundary rather than being immediately adjacent to the bentonite are likely to be minimal.

8.1 FEP Representation

The key FEPs are listed in Table 8-1 and their treatment in the base case simulation are summarised.

Table 8-1 Treatment of key FEPs in the base case simulations

FEP	FEP Treatment in the base case simulation
<i>High-level scenario defining FEPs (Section 2)</i>	
Sulphide supply in groundwater	Flow rates and sulphide concentrations are varied.
Sulphate reducing bacteria (SRB)	<p>This is treated implicitly. Since the buffer is assumed to remain intact, no SRB processes take place in the buffer. Hence the only possible SRB activity is outside the buffer or in the low density gel.</p> <p>Since transport in the fracture is advection-dominated it is sufficient to treat the action of SRB as a perturbation of the sulphide concentration in the porewater.</p>

FEP	FEP Treatment in the base case simulation
Transport of sulphide to the canister (or part-way to the canister) by advection	Buffer redistribution is simulated to represent extrusion of bentonite into the fracture. After this time no further bentonite movement is possible since the bentonite mass is fixed (no erosion). Cavity formation in this case is not possible and density performance criterion is irrelevant (no erosion).
Changed buffer diffusivity (characterised by the relationship to buffer density)	N/A – buffer density remains constant after gel extrusion.
SRB in the presence of cavities or reduced density buffer	N/A – cavity formation not possible.
<i>Features / Geometry (Section 3)</i>	
Fracture apertures and flow properties	Fracture transmissivities in the range 10^{-11} - 10^{-6} m ² /s are considered, with apertures related to transmissivity by the Doe law (Section 5.2)
Bentonite gel transport properties	Diffusive transport processes are not dependent on density.
The buffer/backfill interface	Backfill is not represented.
<i>Processes (Section 4)</i>	
Corrosion	Corrosion is simulated using a zero sulphide concentration on the canister surface. Resulting diffusive fluxes of sulphide to the surface are taken to take part instantly in corrosion reactions, resulting in a diffusion limited reaction.
Sulphate / sulphide species	Only sulphide is considered, since sulphate-sulphide conversion by SRB is imposed externally as a boundary condition.
Pyrite and FeS _(am) solubility	This is treated in a similar way to SRB contributions to sulphide content. Any solubility limit can be imposed as a boundary condition in the fracture due to dominance of the advective transport process.
Gypsum as a source of sulphate in the buffer	This is not included since no sulphate-sulphide conversion is possible (SRB excluded) and sulphate will not therefore contribute to corrosion.
Ion exchange for the Na-Ca system	No density-dependent transport processes, are included, so this is not included in the base case simulations.
Microbial process.	N/A – SRB excluded from the base case simulations (see above).
Bentonite redistribution	Redistribution is implemented as in Section 6. This is only relevant during the initial period of bentonite extrusion into the fracture.

FEP	FEP Treatment in the base case simulation
Bentonite viscosity	Viscosity is implicitly present in the redistribution rate function $D_{sm}(\rho_{sm})$ (see Section 6). This is only relevant during the initial period of bentonite extrusion into fracture.
Colloidal loss term when conditions for erosion are satisfied (i.e. meltwaters are present)	Erosion is not considered in the base case simulations.
<i>External factors (Section 5)</i>	
Fracture flow rates	Fracture transmissivities in the range 10^{-11} - 10^{-6} m ² /s are considered, with apertures related to transmissivity by the Doe law (Section 5.2). During glacial periods the regional head gradient is increased to 0.2 m/m from 0.01 m/m.
Glacial and inter-glacial periods resulting in varying boundary water composition	No erosion is considered so the only relevant attribute of the glacial water composition is the sulphide content. For conservatism (maximal corrosion), the sulphide concentration is kept constant throughout the glacial period. A tracer species is included in the glacial water composition so that residence times in the buffer can be investigated.

8.2 Parameterisation

Since erosion is not being modelled in the simulations in this section, the action of buffer rheology being limited to providing the mechanism for initial intrusion of gel into the fracture. The rheology model is parameterised as discussed in Section 6. The sensitivity of the model to variations in fracture transmissivity and sulphide concentrations in the groundwater is assessed over the parameter ranges shown in Table 8-2.

Table 8-2 Model parameterisation considered in the no-erosion models

Parameter	Value (in base case simulation)	Variants
T	10^{-9} m ² s ⁻¹	10^{-6} – 10^{-11} m ² s ⁻¹
$D_{sm,1700}$ m ² s ⁻¹	10^{-9} m ² s ⁻¹ (to allow gel penetration into fracture)	
c_{HS^-}	10^{-4} mol kg ⁻¹	10^{-5} mol kg ⁻¹

8.2.1 Flow rates

In the base case the transmissivity is $T = 10^{-9}$ m²/s. From Table 5-1, the expected regional Darcy flow rates during glacial and non-glacial periods are approximately $q \approx 400$ and 20 m/y respectively ($\log q \approx 2.6$ and 1.3 m/y respectively). These Darcy velocities are presented in Figure 8-2, which shows the variation of Darcy velocity with time at the location shown by the yellow ellipse in Figure 8-1.

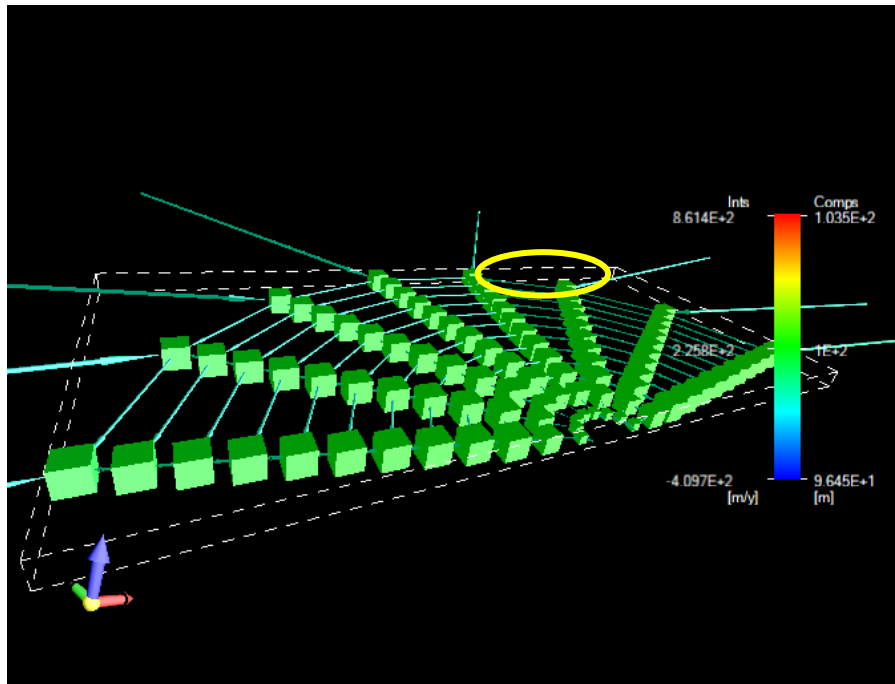


Figure 8-1 Fracture discretisation (not to scale). The location of the Darcy velocity reported in Figure 8-2 is highlighted by the yellow ellipse.

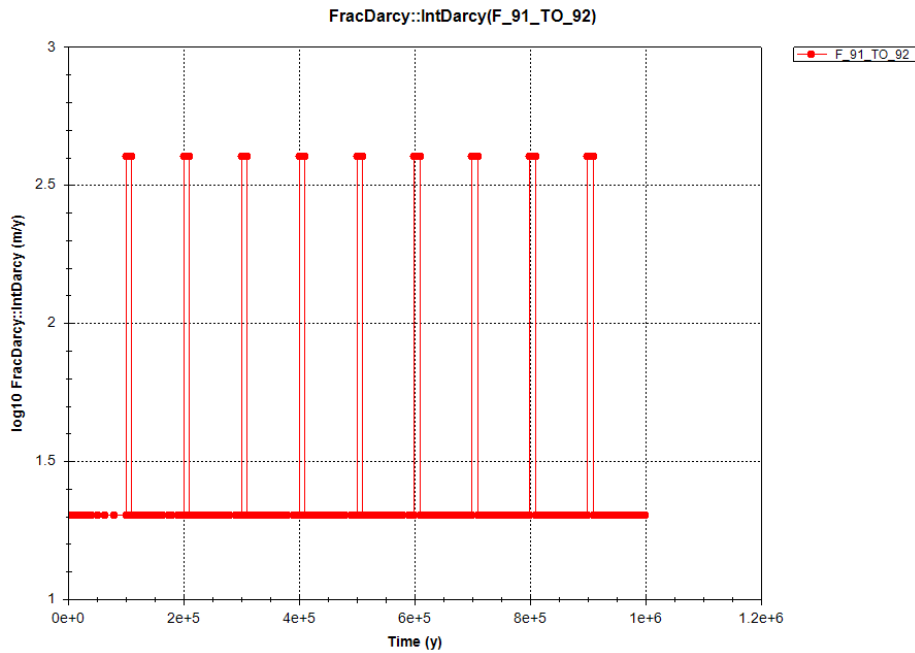


Figure 8-2 Darcy velocity at the outer fracture boundary (see Figure 8-1) in the direction of the regional head gradient for the $T = 10^{-9} \text{ m}^2/\text{s}$ base case. Darcy velocity varies between 20 m/y (between glaciations) to 400 m/y (during glacial period).

8.3 Calculations

8.3.1 Glacial water residence time in the buffer and sulphide transport

The concentration of the glacial water indicator tracer in the boundary condition porewater is shown as a function of time in Figure 8-3 and its concentration in the buffer compartment adjacent to the fracture is shown in Figure 8-4. It is clear that the inter-glacial periods do not provide sufficient time for the glacial water to completely diffuse out of the buffer. It should be noted that since the tracer species does not take part in chemical reactions it is able to penetrate deep into the buffer (Figure 8-5) whereas the concentration gradient induced by the corrosion reaction at the canister surface constrains the transported sulphide to lie close to the plane of the fracture (Figure 8-6).

In the buffer the maximum sulphide concentration is $2.5 \times 10^{-7} \text{ mol/kg}$. Figure 8-7 shows how the sulphide concentration falls from $1 \times 10^{-4} \text{ mol/kg}$ in the fracture through the gel.

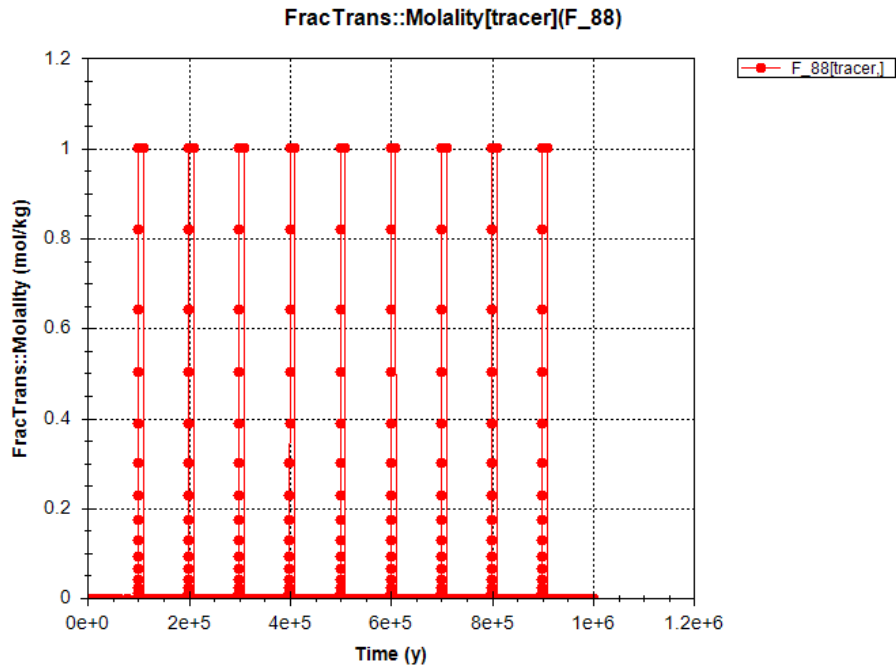


Figure 8-3 Concentration of the tracer species in the glacial meltwater

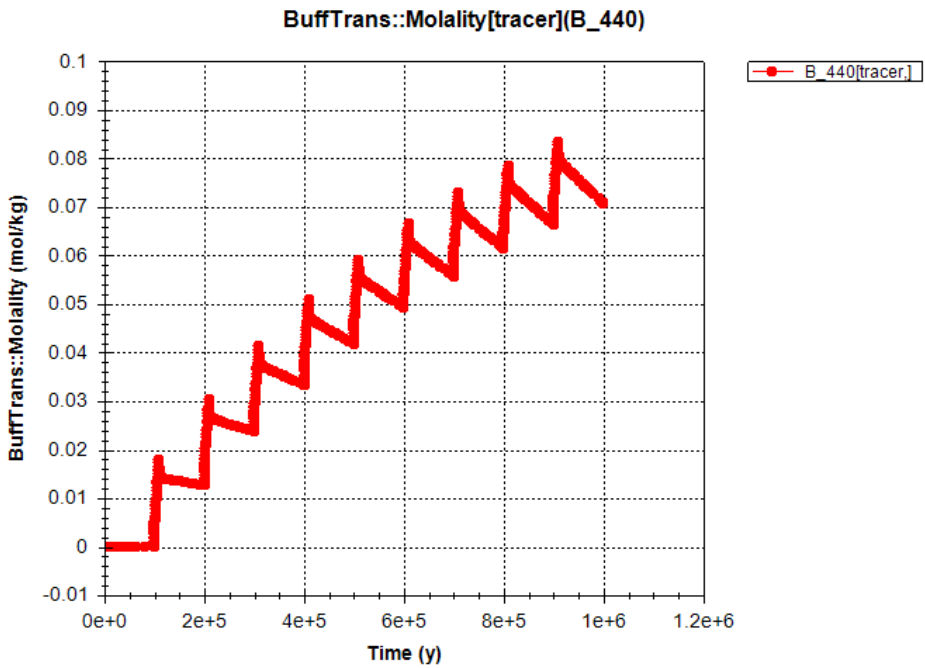


Figure 8-4 Residence of the tracer from the glacial meltwater in the buffer

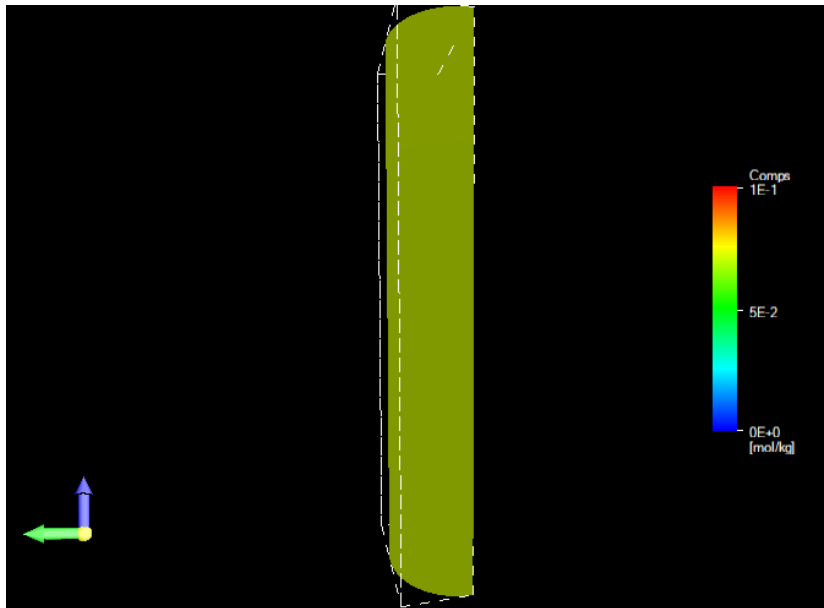


Figure 8-5 Concentration of the tracer species throughout the buffer at 10^6 y. Since the tracer does not take part in chemical reactions it is free to migrate without retardation.

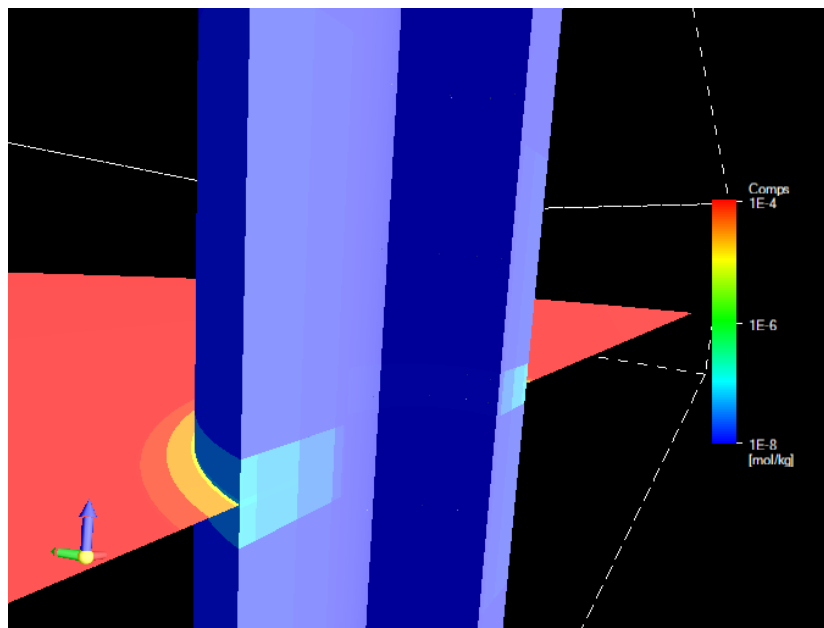


Figure 8-6 Concentration of sulphide in the buffer at 10^6 y. Due to the corrosion reaction at the canister surfaces and the concentration gradient that it induces, sulphide transport is constrained to lie close to the plane of the fracture. (Note that the blue region in the figure shows the region where sulphide concentrations are 10^{-8} mol/kg or less.)

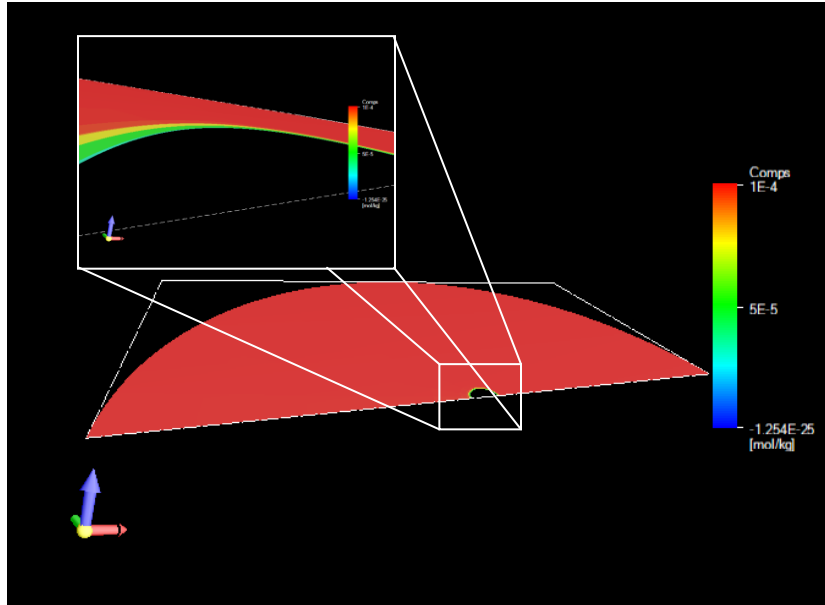


Figure 8-7 Sulphide concentrations at 10^6 y in the fracture and gel (yellow to light-green region) for boundary sulphide molality of 10^{-4} mol/kg

8.3.2 Canister surface corrosion profiles ($T=10^{-9}$ m²/s, sulphide at 10^{-4} mol/kg)

Corrosion profiles on the canister surface for the base case when $T=1 \times 10^{-9}$ m²/s and sulphide molality in the groundwater is 1×10^{-4} mol/kg are shown in Figure 8-8 and Figure 8-9. Slightly greater amounts of corrosion are seen at the upstream end of the canister than the downstream end, although the difference is very small. The maximum corrosion depth occurs in the fracture plane at the upstream end and is approximately 1×10^{-6} m after one million years. The degree of corrosion falls quickly away from the fracture plane with the amount of corrosion essentially falling to zero at distances around 1 m from the fracture plane (Figure 8-10).

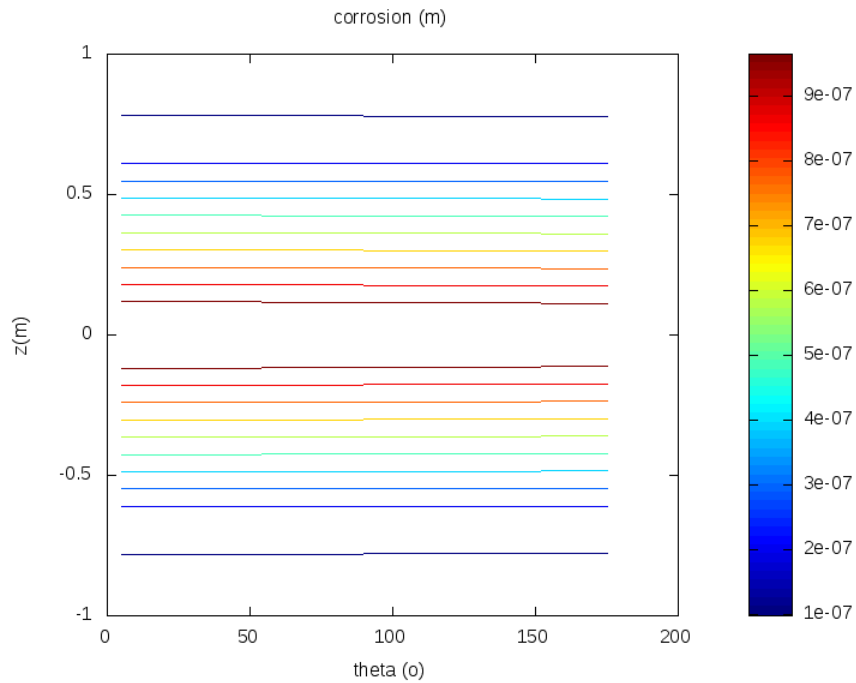


Figure 8-8 Corrosion contours on the canister surface in the base case when $T = 1 \times 10^{-9} \text{ m}^2/\text{s}$. The z coordinate represents distance up the canister, with 0 m corresponding to the position of the fracture plane; “theta” represents the angular coordinate around the canister surface, with $\theta = 0^\circ$ and $\theta = 180^\circ$ corresponding to the upstream and downstream locations on the canister surface.

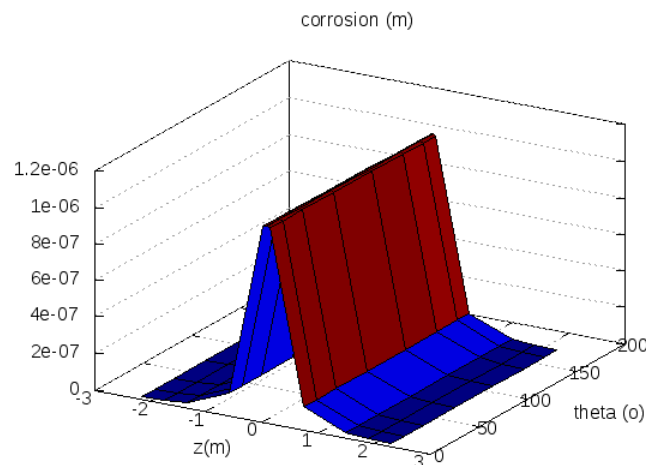


Figure 8-9 As Figure 8-8.

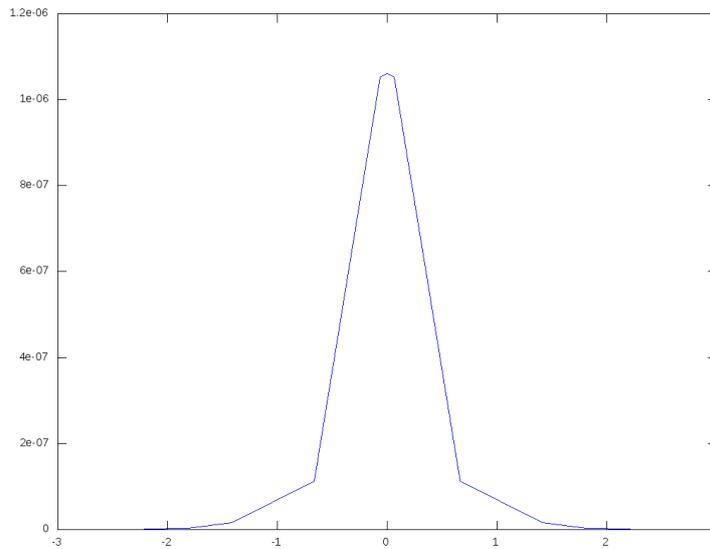


Figure 8-10 Corrosion profile up the canister at the upstream end (c.f. Figure 8-8)

8.3.3 Effect of varying fracture transmissivity

As discussed in Section 5.2, fracture transmissivity is related to the fracture aperture using Doe's law: $a = \zeta T^{1/2}$, with $\zeta = 0.5 \text{ s}^{1/2}$. As was seen in the base case model in Section 8.3.2, corrosion on the canister surface is greatest in the plane of the fracture and falls quickly away from the fracture plane. Figure 8-11 shows the maximum and minimum corrosion depths for a range of fracture transmissivities from 1×10^{-11} to $1 \times 10^{-6} \text{ m}^2/\text{s}$, which equates to fracture apertures in the range $5 \times 10^{-6.5}$ to $5 \times 10^{-4} \text{ m}$ and hydraulic conductivities in the range $2 \times 10^{-5.5}$ to $2 \times 10^{-3} \text{ m/s}$ (see Table 5-1). This leads to Darcy velocities in the range $2 \times 10^{-7.5}$ to $2 \times 10^{-5} \text{ m/s}$ in non-glacial periods and $4 \times 10^{-6.5}$ to 4×10^{-4} during glacial periods (see Table 5-1).

Maximum and minimum amounts of corrosion in the fracture plane occur in the upstream and downstream locations respectively. However the amount of variation in the upstream and downstream locations is very small and is barely noticeable even at very low transmissivities. Figure 8-11 shows that the amount of corrosion in the fracture plane exceeds $10 \text{ }\mu\text{m}$ after one million years only in cases where the transmissivity is greater than $1 \times 10^{-7} \text{ m}^2/\text{s}$.

The gradient of the curve in log units is $1/2$, which implies that the maximum amount of corrosion that can be expected in the fracture plane under these simple assumptions is proportional to the square root of the transmissivity, which is proportional to the aperture when using the Doe law.

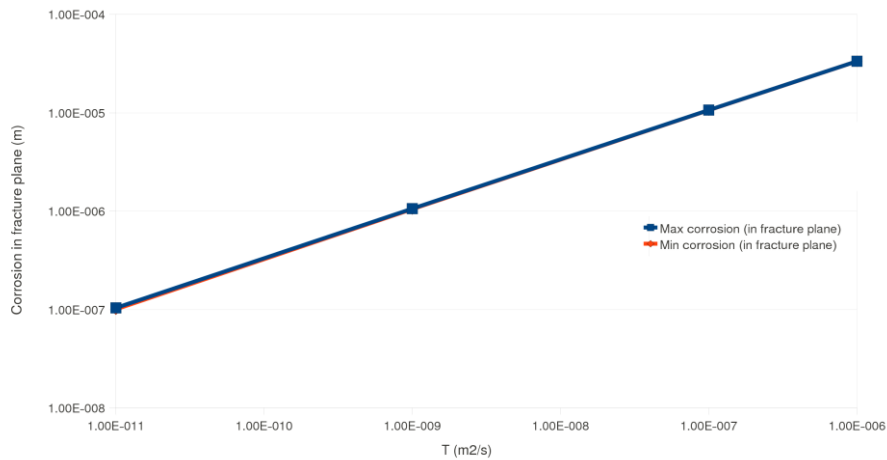


Figure 8-11 Maximum / minimum corrosion depths after one million years on the canister surface in the plane of the fracture as a function of transmissivity

8.3.4 Effect of varying sulphide concentrations

In the base case simulations, the effect of SRB in the fracture, or alternative sulphide buffering processes such as mineral-imposed solubility limits, can be expressed through changes in the sulphide concentration in the fracture porewater composition (Section 8.1).

Since the transport conditions in the fracture are advection-dominated for the range of transmissivities that are considered, and since there are effectively no sulphide transport or reaction processes in the buffer other than diffusion and the corrosion boundary (which is a zero sulphide concentration boundary condition), the amount of corrosion on the canister surface can be expected to vary approximately linearly with the sulphide concentration in the boundary porewater, since the concentration gradient across the buffer is scaled linearly by the boundary condition perturbation.

Figure 8-12 shows the same data as Figure 8-11, with superimposed data points for a simulation in which the sulphide concentration on the boundary is reduced by an order of magnitude (to 1×10^{-5} mol/kg). The calculated maximum and minimum amounts of corrosion in the fracture plane are an order of magnitude lower, as would be expected. Extrapolated lines showing the approximated maximum/minimum amounts of corrosion by scaling amounts of corrosion observed in the higher concentration cases for the other fracture transmissivities are also shown in the figure.

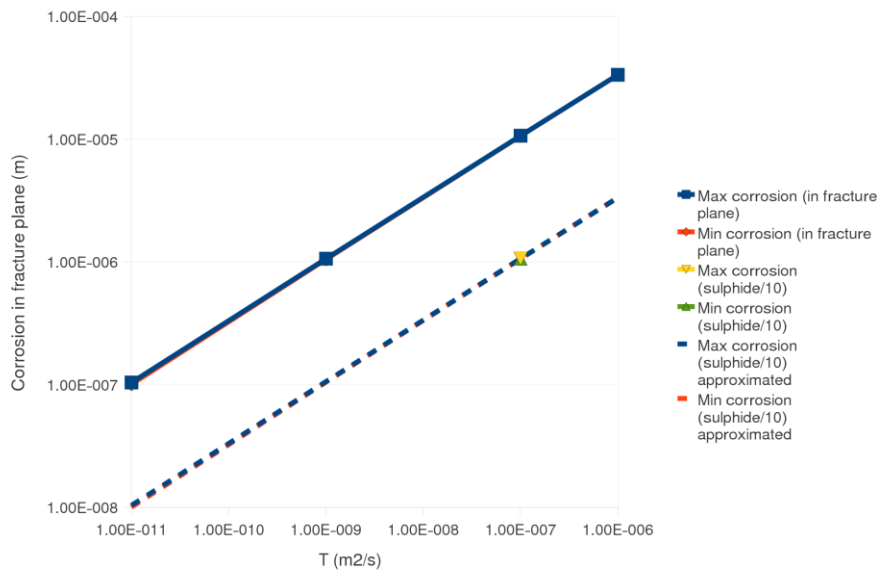


Figure 8-12 As Figure 8-11, with computed amounts of corrosion when the sulphide concentration in the fracture porewater is reduced by an order of magnitude (to 1×10^{-5} mol/kg) and lines showing approximated amounts of corrosion assuming the simple linear scaling.

Continuing the simple analysis from the previous section, the amount of corrosion in the fracture plane that can be expected in these simple models at 10^6 y can therefore be estimated as $\log C_{\max}^{(1e6)} = 1/2 \log T + \log c_{HS^-} + 2.5$, i.e.

$$C_{\max}^{(1e6)} = c_{HS^-} \sqrt{T} \times 10^{2.5}$$

or

$$C_{\max}^{(1e6)} = 2ac_{HS^-} \times 10^{2.5} \text{ (using the Doe law).}$$

Here $C_{\max}^{(1e6)}$ is the maximum depth of corrosion (m) at 10^6 y, a is the fracture aperture (m), T is the fracture transmissivity ($m^2 s^{-1}$) and c_{HS^-} is the sulphide concentration in the fracture (mol/kg). The maximum rate of corrosion on the canister surface (i.e. in the plane of the fracture) in these models, $R_{corrosion}$ ($m y^{-1}$), could therefore be expressed as

$$R_{corrosion} = c_{HS^-} \sqrt{T} \times 10^{-3.5} \text{ or } R_{corrosion} = 2ac_{HS^-} \times 10^{-3.5}.$$

Using this simple rate formula for one million years reproduces the maximum amounts of corrosion shown in Figure 8-12.

8.3.5 Comparison with SKB's calculated corrosion rates

Figure 8-13 (taken from [2]) shows cumulative probabilities for the rate of corrosion predicted by SKB's CPM and DFN models for the "Q1" pathway (a fracture intersecting a deposition hole) for a case when the sulphide concentration is 1×10^{-5} mol/kg. In these models the median fracture transmissivity is around 1×10^{-7} m²/s ([9] Section 6.5.6). The expected rate of corrosion is around 1×10^{-8} mm/y for all of the concepts and so for the simulation period considered in this study would equate to a corrosion depth of 1×10^{-5} m on the canister surface near the fracture.

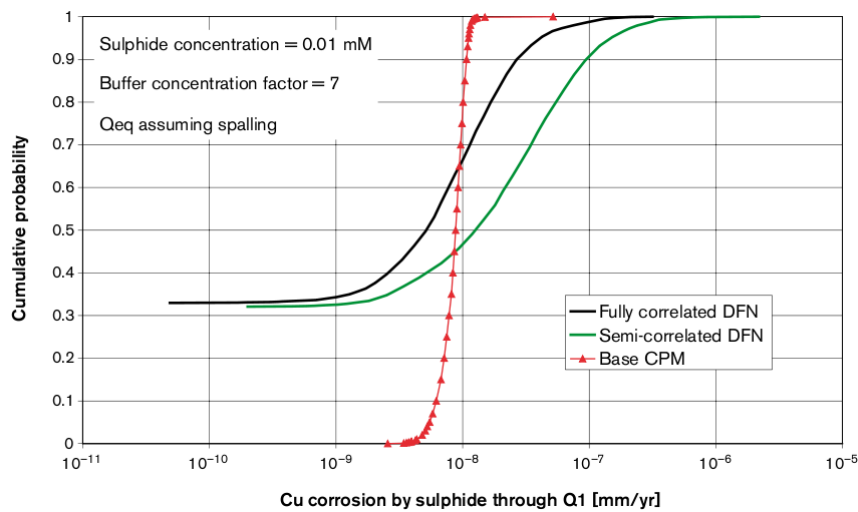


Figure 8-13 Expected amount of corrosion in SKB's DFN models ([2] Fig 9-62)

This choice of transmissivity and sulphide concentration corresponds to the "sulphide/10" data points shown in Figure 8-12, where a corrosion depth of 1×10^{-6} m was calculated in the base case simulation. Therefore the amounts of corrosion calculated here are around an order of magnitude lower than those reported by SKB.

One reason for the difference in the results may be that calculations performed by SKB did not take account of the added resistance to diffusion of the gel that has intruded into the fracture. In these calculations the gel extends around 15 cm into the fracture, which adds around 50% to the distance over which sulphide must diffuse to reach the canister surface, whereas the "Q-equivalent" calculations performed by SKB assume that bentonite only reaches as far as the edge of the deposition hole. The calculations presented in Section 9 where cavities are introduced to the model and where the gel is allowed to erode help to explain these differences.

9 The Base Case Scenario with Imposed Buffer Cavities

Corrosion of the canister surface will be enhanced if advective flow conditions are allowed to develop within the buffer, thus reducing the length of the diffusive pathway for corrodants to the canister surface. In this section we investigate the effect that cavities with varying size and shape can have on the amount of corrosion. We do this by imposing the presence of cavities on the model discussed in Section 8 rather than allowing cavities or low density regions to develop as a consequence of a mechanistic erosion process, which is discussed in Section 10.

In the models in this section the rheological properties of the buffer are ignored so that cavities remain open and lead to maximal amounts of corrosion. This is implemented by setting the parameter controlling the rate of redistribution, $D_{sm,1700}$ (see Section 6), to zero. In reality the buffer can be expected to recover from the development of any such cavities whilst its swelling capacity remains. The self-sealing process has been modelled by SKB [21] to investigate the potential for the bentonite to heal after erosion processes, or to homogenise in the early phase of evolution if any bentonite rings are imperfectly constructed during emplacement. The former of these processes is investigated in more detail in Section 10, where the development of non-uniform densities in the bentonite as a result of erosion is also simulated (rather than imposed) and is coupled to the buffer redistribution process, which allows low density regions to appear and recover cyclically with glaciations.

To simplify the comparison of results the same fracture transmissivity is used for all calculations in this section, and hence the same aperture is used throughout since the two are related by the Doe law (Section 5.2). A transmissivity of 10^{-7} m²/s is used, which corresponds to an equivalent aperture of 1.58×10^{-4} m.

In these models the cavities are assigned a hydraulic conductivity that is greater than that of intact bentonite, but less than that of the open fracture. The hydraulic conductivity of the open fracture is given by $T/a = 2 \times 10^{-3.5}$ m/s. Taking this hydraulic conductivity inside the buffer region of the model, where the grid sizes are relatively small, can lead to numerical difficulties when glacial periods begin and end since the concentrations of advected species will change rapidly as the groundwater flow velocity changes. The hydraulic conductivity in the cavity is set to 10^{-8} m/s, which is obviously considerably lower than the open fracture, but is still around six orders of magnitude higher than that of intact bentonite. Diffusion in the cavities is taken to be the same as in the open fracture.

Since the cavities in these models are not taken to be completely open from the point of view of advection, they could be considered to contain low density eroded bentonite that has not all been able to migrate away from the deposition hole.

A number of cavity geometries are considered:

- ▲ (CAV-FS) An annular cavity of the same height as the fracture aperture that extends across the full width of the buffer;
- ▲ (CAV-HS) An annular cavity of the same height as the fracture aperture that extends half the distance from the fracture to the canister surface;
- ▲ (CAV-FM) An annular cavity of height 22 cm, centred vertically on the fracture that extends across the full width of the buffer;
- ▲ (CAV-HM) An annular cavity of height 22 cm, centred vertically on the fracture that extends half the distance from the fracture to the canister surface;
- ▲ (CAV-HT) An annular cavity of half the height of the canister, centred vertically on the fracture that extends half the distance from the fracture to the canister surface;

The naming convention for the cavities is *CAV-WidthHeight* where cavity widths are fully across the buffer (F) or half of the way across the buffer (H) and heights are small (S), being the same height as the aperture, medium (M), being 22 cm and tall (T) being half the height of the canister, i.e. approximately 2.42 m. The small height cases could perhaps more accurately be described as fractured buffered cases rather than cavities.

The medium and tall geometries are shown schematically in Figure 9-1 to Figure 9-3. It is not possible to view the geometries for the small cavity height case due to the small size of the fracture aperture (since the transmissivity is 10^{-7} m²/s the implied fracture aperture is 0.158 mm which is not visible in the context of the full canister height), however conceptually they are similar to the HM and FM figures, but with a smaller cavity height.

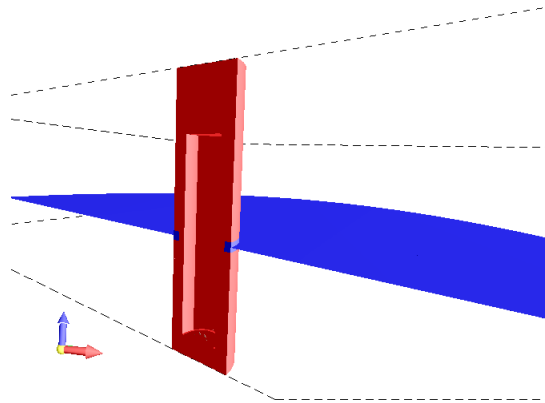


Figure 9-1 CAV-HM Geometry. Cavity of medium height extends half-way through the buffer.

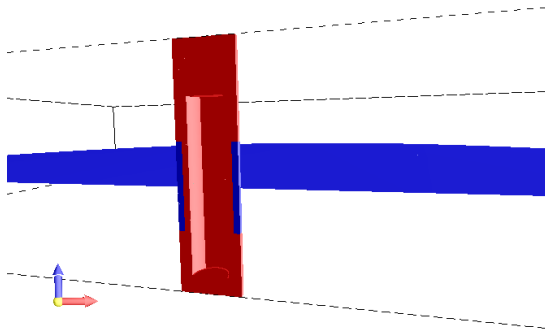


Figure 9-2 CAV-HT Geometry. Tall cavity extends half-way through the buffer.

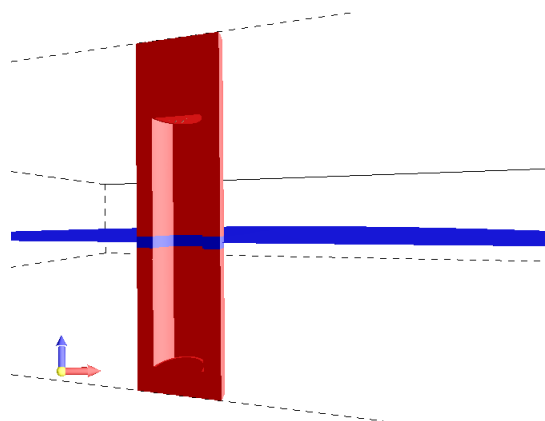


Figure 9-3 CAV-FM Geometry. Cavity of medium height extends fully through the buffer.

9.1 FEP Representation

The key FEPs are listed in Table 9-1 and their treatment in the imposed cavity simulations are summarised where this differs from the treatment in the base case (Table 8-1).

Table 9-1 Treatment of key FEPs in the imposed cavity models

FEP	FEP Treatment in the imposed cavity model
<i>High-level scenario defining FEPs (Section 2)</i>	
Sulphide supply in groundwater	As base case.
Sulphate reducing bacteria (SRB).	The buffer is assumed to contain cavities but be otherwise intact. For this reason the only possible locations for microbial activity are in the fracture and in the cavities. Since transport in the fracture and cavities is advection-dominated it is sufficient to treat the action of SRB as a perturbation or the sulphide concentration in the porewater.
Transport of sulphide to the canister (or part-way to the canister) by advection	Buffer redistribution is disabled to prevent cavities from re-sealing. Cavities are imposed on the model with a variety of geometry and sizes. Erosion is not considered (other than the implicit assumption that erosion of some sort lead to the formation of the cavities), hence comparison with the performance criterion is not necessary.
Changed buffer diffusivity (characterised by the relationship to buffer density)	N/A – buffer density remains constant since there is no erosion or redistribution.
SRB in the presence of cavities or reduced density buffer	Treated implicitly through variations in porewater sulphide concentration due to advective conditions dominating the fracture and cavity regions.
<i>Features / Geometry (Section 3)</i>	
Fracture apertures and flow properties	As base case.
Bentonite gel transport properties	N/A – no gel regions are present in the model. Gel is assumed to have been removed during cavity formation (all cavities are located adjacent to the fracture).
The buffer/backfill interface	As base case.
<i>Processes (Section 4)</i>	
Corrosion	As base case.
Sulphate / sulphide species	As base case.

FEP	FEP Treatment in the imposed cavity model
Pyrite and FeS _(am) solubility	As base case.
Gypsum as a source of sulphate in the buffer	As base case.
Ion exchange for the Na-Ca system	As base case.
Microbial processes	As base case.
Bentonite redistribution	N/A – the redistribution model is disabled to prevent cavities from re-sealing.
Bentonite viscosity	N/A – no redistribution.
Colloidal loss term (kg m ⁻² y ⁻¹) when conditions for erosion are satisfied (i.e. meltwaters are present)	Additional erosion beyond that assumed to have formed the cavities is not considered.
<i>External factors (Section 5)</i>	
Fracture flow rates	A fixed fracture transmissivity $T = 10^{-7} \text{ m}^2 \text{ s}^{-1}$ is assumed in the models to facilitate comparison of the effects of the varying geometries. Comparing the results with the analogous model in the no-erosion simulations (Section 8.3.3) will allow the likely effects of similar cavities being included in models with other transmissivities.
Glacial and inter-glacial periods resulting in varying boundary water composition	As base case.

9.2 Parameterisation

Since erosion is not being modelled in the simulations in this section and since we want to evaluate the effect on corrosion if the cavities are allowed to remain open, bentonite redistribution is disabled (by setting $D_{sm,1700} = 0$). The sensitivity of the model to variations in the cavity geometry is assessed, but no other variations are considered. Transmissivity is fixed at $T = 10^{-7} \text{ m}^2 \text{ s}^{-1}$. It should be possible to estimate the likely effect of cavities neighbouring fractures with other transmissivities by relating the results of these simulations to the analogous model in the no-erosion simulations (Section 8.3.3). The boundary condition sulphide concentration is set to 10^{-4} M .

9.3 Calculations

The effect of the various cavity geometries and sizes on the corrosion profiles on the canister surface at 10^6 y is shown in Figure 9-5 to Figure 9-9.

For comparison the corrosion profile when no cavity is present (and no erosion takes place) is shown in Figure 9-4.

The maximal amounts of corrosion on the canister surface are again in the plane of the fracture, and the amounts of corrosion are greater than seen for the simulations without cavities, as would be expected. The amounts of corrosion at 10^6 y at the upstream and downstream ends of the fracture plane are shown in Table 9-2. The CAV-FS model, in which the cavity is assumed to extend over the entire distance to the canister surface with an aperture equal to the fracture, shows the maximum depth of corrosion ranging from 1.86 cm downstream to 2.86 cm at the upstream end – a significant fraction of the 5 cm canister thickness. This is clearly quite an unlikely scenario since the focussing of erosion in a single planar direction within the buffer to cause a cavity with this geometry would not seem to be plausible; possibly a fracturing event in a buffer that had lost its plasticity could lead to this type of configuration. However it does provide a useful upper bound on the possible amount of corrosion. In this scenario the corrosion is focussed in a narrow band on the canister surface, as can be seen in Figure 9-5.

Table 9-2 Corrosion depths in the imposed cavity models at the upstream and downstream ends of the fracture plane at 10^6 y

Model	Upstream corrosion depth in fracture plane (m)	Downstream corrosion depth in fracture plane (m)
No cavity (Figure 9-4)	1.06×10^{-5}	1.06×10^{-5}
CAV-FS (Figure 9-5)	2.68×10^{-2}	1.86×10^{-2}
CAV-FM (Figure 9-6)	7.58×10^{-3}	1.76×10^{-3}
CAV-HS (Figure 9-7)	1.10×10^{-3}	7.65×10^{-4}
CAV-HM (Figure 9-8)	2.29×10^{-3}	1.37×10^{-3}
CAV-HT (Figure 9-9)	8.62×10^{-4}	3.58×10^{-4}

Increasing the aperture of the cavity in the CAV-FS case, to give the CAV-FM case, also reduces the depth of corrosion in the fracture plane, this time by a factor of around 3.5 and 10.5 in the upstream and downstream directions respectively to give corrosion depths in the range 1-7 mm. Although the maximum depth of corrosion is reduced, the corrosion is spread over a greater area and so, from a canister performance perspective, this might be considered to be more important as it could be argued that the cavity geometry is more likely to occur than the more planar cavity of the CAV-FS case. The cavity is 22 cm high by 35 cm deep and so represents a more spatially uniform pattern of implied erosion with a geometry closer to

that which might be expected if erosion within the buffer were believed to be possible. The cavity implies a total volume of eroded buffer of around 0.34 m^3 or around 560 kg, assuming a density of $1\,655 \text{ kg m}^{-3}$. One bentonite ring has a dry mass of around $1\,200 \text{ kg m}^{-3}$ [2], so this loss is equivalent to a volume of around half of one ring.

Halving the depth of the cavity to half the buffer width reduces the amount of corrosion, since a dominantly diffusive pathway to the canister surface remains. Maximum corrosion depths of around 1.1 mm, 2.3 mm and 0.8 mm are seen for the short, medium and tall cavities, illustrating that increasing the cavity height increases the amount of corrosion up to a point, until the range in height over which the sulphide-rich water is shared leads to a reduction in the maximum corrosion depth, although, as can be seen in Figure 9-9, the range over which the surface corrosion is spread at non-trivial levels extends almost the full height of the canister. The CAV-HM geometry leads to 1-2 mm maximal corrosion depths.

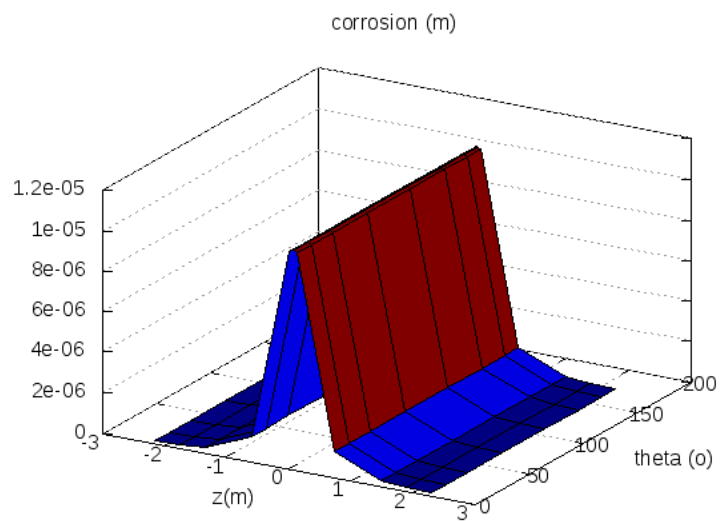
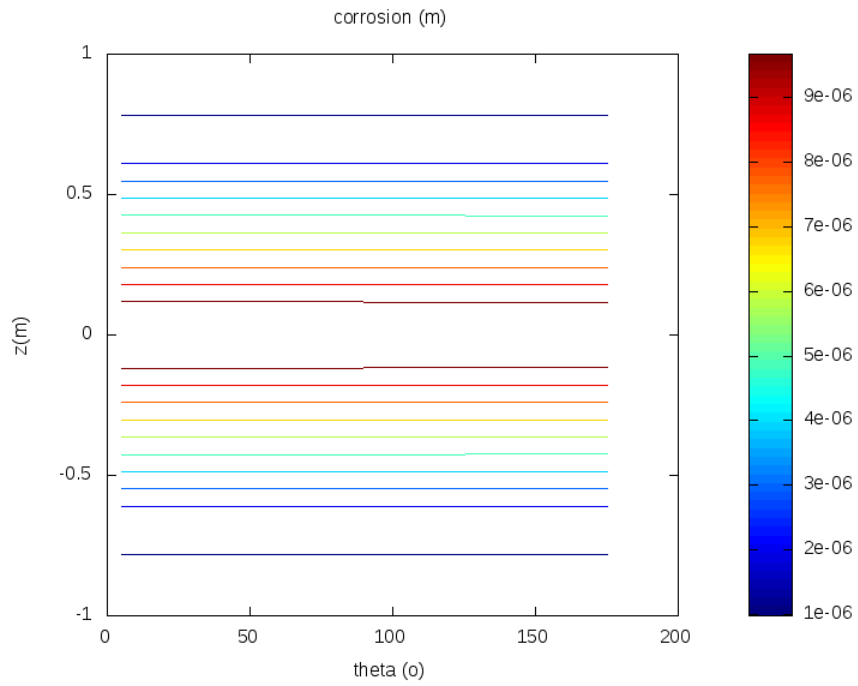


Figure 9-4 Corrosion profiles on the canister surface at 10^6 y in the case when no cavity is present (same calculat as Section 8.3.3).

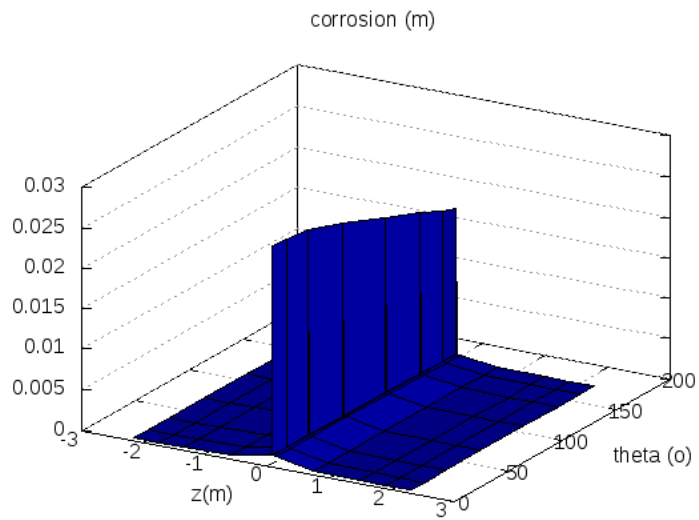
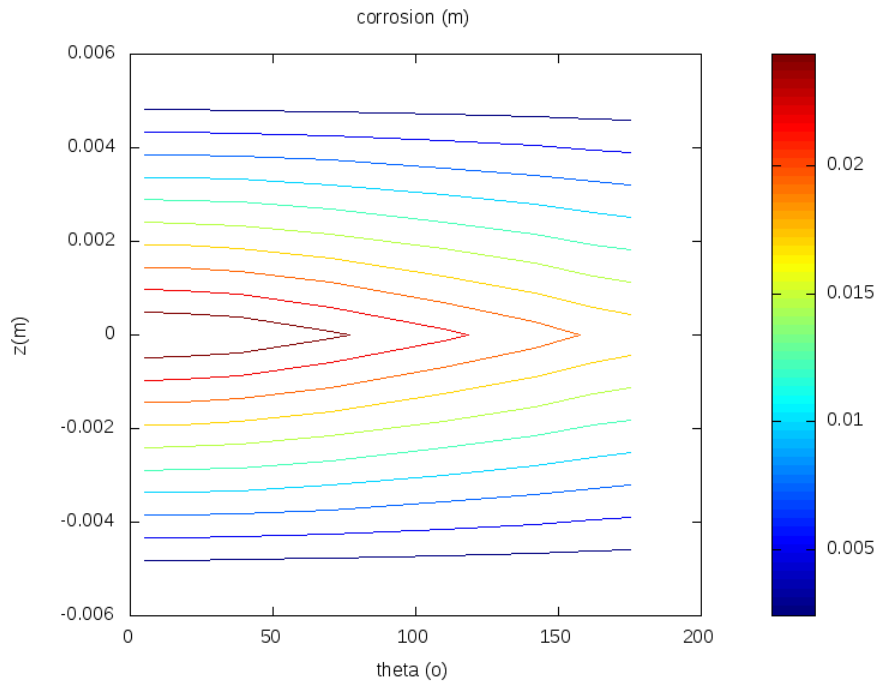


Figure 9-5 CAV-FS: Corrosion profiles at 10^6 y

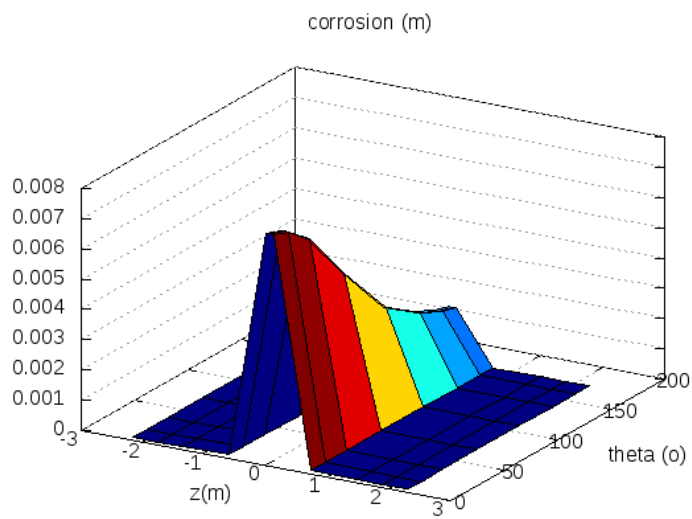
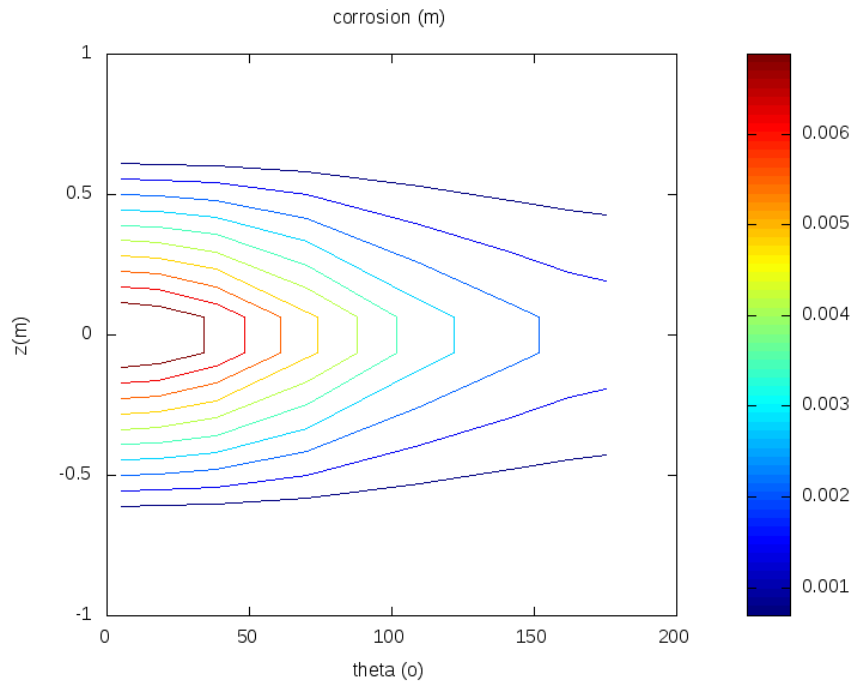


Figure 9-6 CAV-FM: Corrosion profiles at 10^6 y

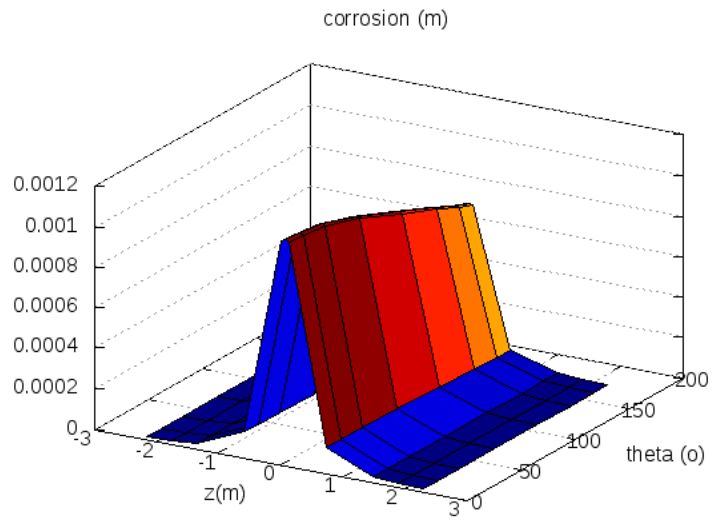
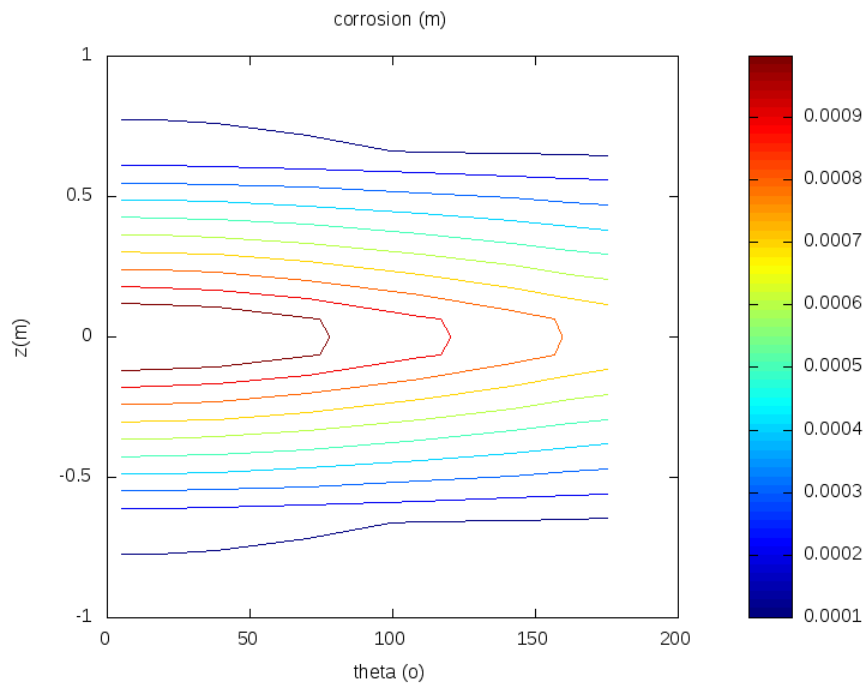


Figure 9-7 CAV-HS: Corrosion profiles at 10^6 y

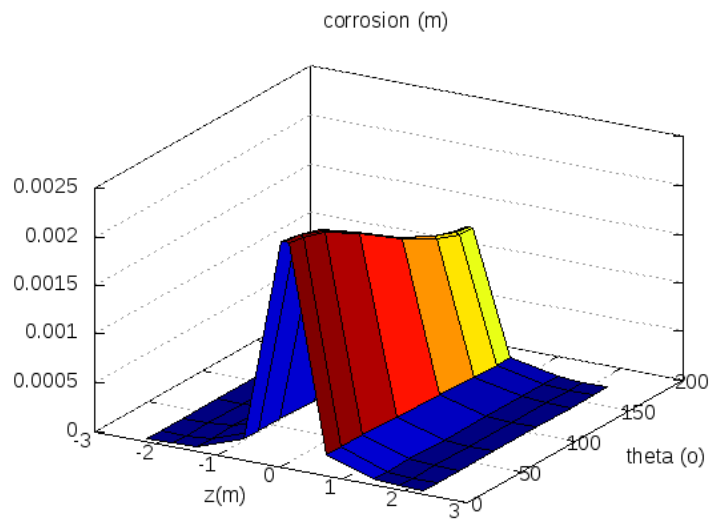
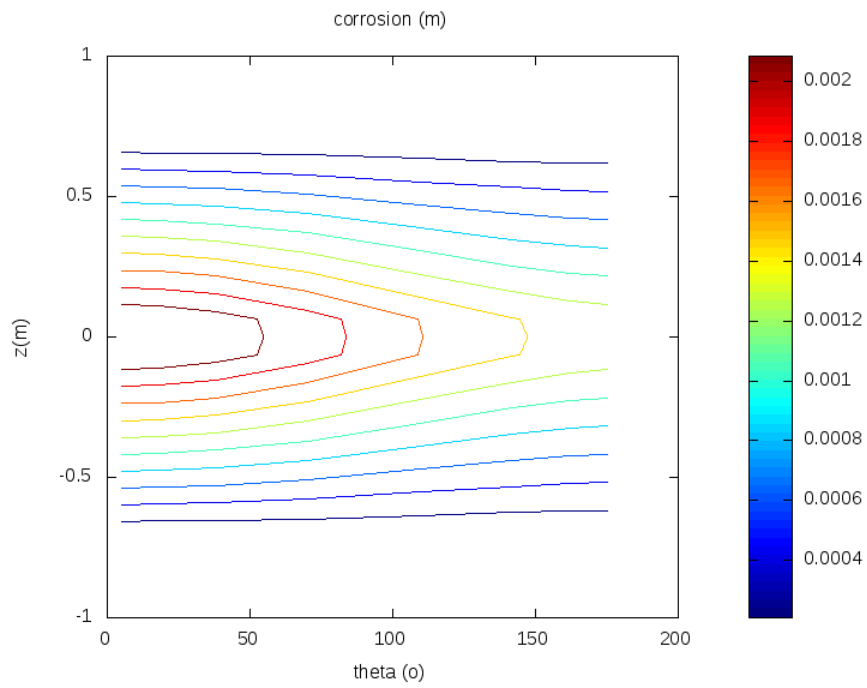


Figure 9-8 CAV-HM: Corrosion profiles at 10^6 y

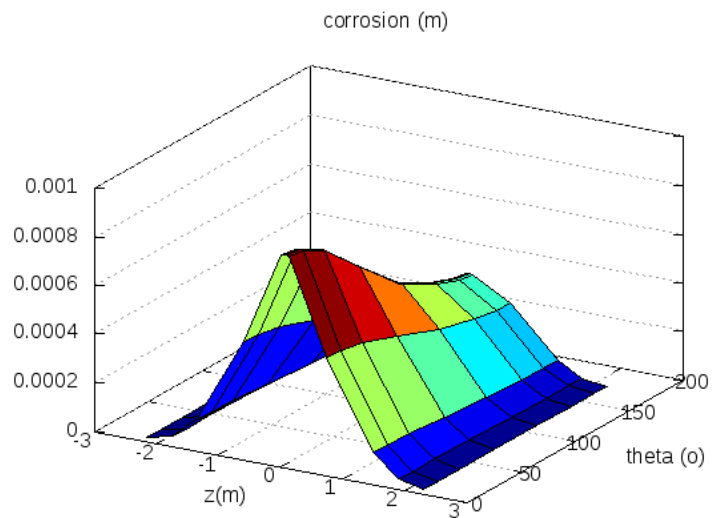
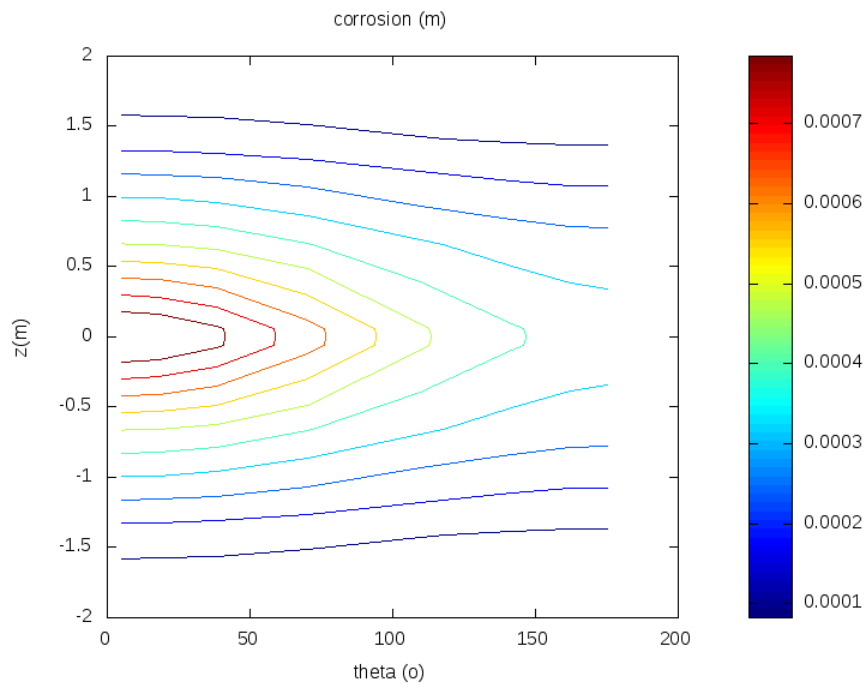


Figure 9-9 CAV-HT: Corrosion profiles at 10^6 y

9.3.1 Comparison with SKB's calculated corrosion rates

Figure 9-10 ([2] Figure 9-102) shows SKB's calculated corrosion rates in the plane of the fracture for a deposition hole containing a cavity of height 0.35 m centred vertically on the fracture and extending to the canister surface. Probabilistic rates are reported since a range of fracture transmissivities below $10^{-6} \text{ m}^2 \text{ s}^{-1}$ were considered in the calculations. The 95th percentile of corrosion depths was greater than 0.7 mm for the Forsmark base case DFN and greater than 3 mm for the Forsmark semi-correlated DFN.

The case discussed in the preceding section that is most similar to the 0.35 m cavity assumed in SKB's models is CAV-FM, in which the cavity has a height of 0.22 m and for which the upstream and downstream corrosion depths were found to be 7.6 mm and 1.8 mm respectively when the fracture transmissivity was taken to be $10^{-7} \text{ m}^2 \text{ s}^{-1}$. SKB's calculations assumed a sulphide concentration of 10^{-5} M whereas the preceding calculations assumed 10^{-4} M . Following the discussion in Section 8.3.4, the equivalent amounts of corrosion that can be expected from the CAV-FM case when sulphide concentrations are 10^{-5} M are a tenth of the values that were calculated, i.e. 0.76 mm upstream and 0.18 mm downstream. The average rates of corrosion implied by these amounts of corrosion are shown by the blue dashed lines on Figure 9-10. The results suggest that the rates of corrosion are consistent with those calculated by SKB.

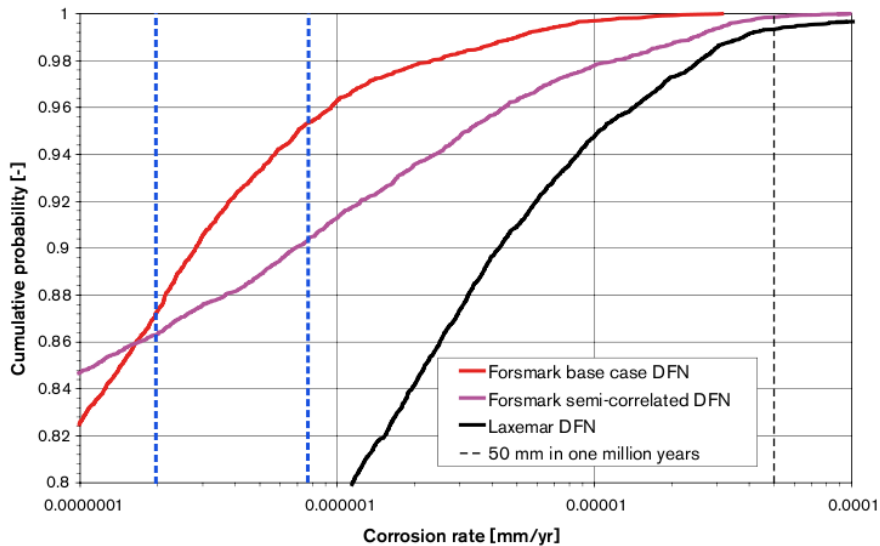


Figure 9-10 Copper corrosion rate in a deposition hole where advection occurs over a 0.35 m high half-cylindrical area centred around the intersecting fracture. The vertical line at $5 \cdot 10^{-5} \text{ mm/yr}$ denotes the rate required to penetrate the 50 mm copper shell in one million years (from [2] Figure 9-102). Blue dashed lines show the equivalent average upstream / downstream corrosion rates in the CAV-FM calculations.

10 Erosion Case Modelling

In the simulations in this section the colloidal concentration-limited erosion rates described in Section 7.2 are added to the base case (no erosion) simulations presented in Section 8. Buffer redistribution is simulated at all times. Initially the redistribution model governs extrusion of bentonite gel into the fracture (as in Section 7.2), but at later times it also controls the rheological response to buffer loss, and re-extrusion of material into the fracture after the glacial period has passed, if the gel front has receded due to erosion. The same process could be used to simulate the effect of an imperfectly emplaced buffer ring and represent the re-homogenisation of density within the buffer, similar to the self-sealing process that has been modelled by SKB [21].

The redistribution model can lead to non-uniform buffer densities and, in extreme cases, the formation of cavities. The tendency to form cavities will depend on the rate of redistribution. Fast redistribution will tend to prevent cavity formation but will lead to a more uniform net reduction in density. Slower redistribution will tend to preserve the local buffer density except in regions where erosion takes place, where the tendency to form cavities will be enhanced. The swelling capacity of the bentonite, and hence its ability to re-seal cavities and re-homogenise low density regions following glaciation, is assumed to persist provided that the smectite dry density exceeds a critical value of $1\,000\text{ kg m}^{-3}$. This criterion has been chosen somewhat arbitrarily and is lower than some other key bentonite dry densities that are required to support alternative performance criteria of the buffer, such as its ability to exclude microbes. It is included to show that the effect of loss of swelling capacity can be represented if data to support such a cut-off is available.

The simulations do not include redistribution of material between the deposition hole and the tunnel above it. There is potential for material to move either way across this interface and this may be a topic for a future study.

The hydraulic conductivity of the bentonite is taken to be a function of the bentonite density.

The central case that is discussed assumes a fracture transmissivity of $T = 10^{-7}\text{ m}^2\text{ s}^{-1}$ and a bentonite redistribution parameter $D_{sm} = 10^{-9}\text{ m}^2\text{ s}^{-1}$. This is a reasonably fast redistribution rate that tends to maintain fairly uniform buffer densities when the density is close to initial values. Calculations for a less transmissive fracture ($T = 10^{-9}\text{ m}^2\text{ s}^{-1}$ with $D_{sm} = 10^{-11}\text{ m}^2\text{ s}^{-1}$) and a more transmissive fracture ($T = 10^{-6}\text{ m}^2\text{ s}^{-1}$ with $D_{sm} = 10^{-11}\text{ m}^2\text{ s}^{-1}$) are also discussed.

10.1 FEP Representation

The key FEPs are listed in Table 10-1 and their treatment in the erosion case model are summarised where this differs from the base case.

Table 10-1 Treatment of key FEPs in the erosion case models

FEP	FEP Treatment in the erosion case model
<i>High-level scenario defining FEPs (Section 2)</i>	
Sulphide supply in groundwater	As base case
Sulphate reducing bacteria (SRB).	SRB are not considered in the erosion case simulations, except in that the effect of any SRB in the fracture can be simulated by altering the boundary porewater sulphide composition (due to the dominance of advection in the fracture).
Transport of sulphide to the canister (or part-way to the canister) by advection	<p>Buffer redistribution is simulated. Initially the redistribution model governs extrusion of bentonite gel into the fracture, but at later times it controls the rheological response to buffer loss due to erosion, and re-extrusion of material into the fracture after the glacial period has passed (if the gel front recedes due to erosion).</p> <p>The redistribution model can lead to non-uniform buffer densities and, in extreme cases, the formation of cavities. The tendency to form cavities depends on the rate of redistribution. Fast redistribution will tend to prevent cavity formation but will lead to more uniform net reduction in density. Slower redistribution will tend to preserve local buffer density except in regions where erosion takes place, where the tendency to form cavities will be enhanced.</p>
Changed buffer diffusivity (characterised by the relationship to buffer density)	The effective diffusion coefficient in the buffer is linearly proportional to the bentonite porosity (which is coupled to the evolution of the dry density).
SRB in the presence of cavities or reduced density buffer	SRB are not considered in these simulations.
<i>Features / Geometry (Section 3)</i>	
Fracture apertures and flow properties	As base case.
Bentonite gel transport properties	Diffusive transport processes are dependent on bentonite density.
The buffer/backfill interface	As base case.
<i>Processes (Section 4)</i>	
Corrosion	As base case.

FEP	FEP Treatment in the erosion case model
Sulphate / sulphide species	Only sulphide is considered.
Pyrite and FeS _(am) solubility	Since SRB are not present, maximum sulphide concentrations are dictated by the boundary water composition, which can be related back to mineral solubility.
Gypsum as a source of sulphate in the buffer	As base case.
Ion exchange for the Na-Ca system	As base case.
Microbial processes	N/A – SRB excluded from the simulations (see above).
Bentonite redistribution	Redistribution is implemented as in Section 6.
Bentonite viscosity	Viscosity is implicitly present in the redistribution rate function $D_{sm}(\rho_{sm})$ (see Section 6).
Colloidal loss term (kg m ⁻² y ⁻¹) when conditions for erosion are satisfied (i.e. meltwaters are present)	A constant colloidal loss rate of 100 kg m ⁻² y ⁻¹ is assumed.
<i>External factors (Section 5)</i>	
Fracture flow rates	Fracture apertures are related to transmissivity using the Doe law (Section 5.2). During glacial periods the regional head gradient is increased to 0.2 m/m from 0.01 m/m.
Glacial and inter-glacial periods resulting in varying boundary water composition	For conservatism (maximal corrosion), the sulphide concentration is kept constant throughout the glacial period. Glacial and inter-glacial periods are used to control activation and de-activation of the erosion process.

10.2 Parameterisation

The hydraulic conductivity of the bentonite is taken to be a function of the smectite density, with hydraulic conductivity increasing as the bentonite density falls. At a critical density (500 kg m⁻³) the location is assumed to have become a cavity at which time the cavity hydraulic conductivity (to 10⁻⁸ m s⁻¹) from Section 9 is applied. As discussed in Section 9, this hydraulic conductivity is higher than the conductivity of “open space”, but is still six orders of magnitude higher than that of intact bentonite, so the distinction between non-advective buffer and advective cavity is clear. The dependence of buffer hydraulic conductivity on dry density for dry densities above 500 kg m⁻³ is based on that given in SKB (2006c), as shown in Figure 10-1.

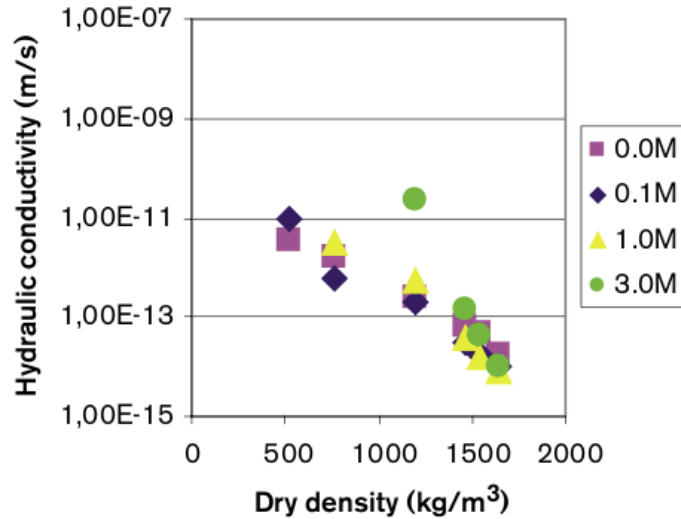


Figure 10-1 Variation of bentonite hydraulic conductivity with dry density (from [9] Figure 5-3)

The bentonite hydraulic conductivity has the form

$$\log K_{sm} = \begin{cases} -11 - 3 \frac{\rho_{sm} - 500}{1000} & \rho_{sm} \geq 501 \text{ kg/m}^3, \\ -11.003 - 3.003(\rho_{sm} - 501) & 500 \text{ kg/m}^3 \leq \rho_{sm} \leq 501 \text{ kg/m}^3 \\ -8 & \rho_{sm} \leq 500 \text{ kg/m}^3. \end{cases}$$

where K_{sm} is the bentonite hydraulic conductivity (m s^{-1}) and ρ_{sm} is the bentonite dry density (kg m^{-3}).

The bentonite diffusion coefficient is also assumed to be dependent on the evolving dry density. However since no trend of the bentonite diffusion coefficient with dry density is reported by SKB (in particular, in [22] it is stated that “In particular, there is no clear trend of D_e as a function of smectite content.”) the diffusion coefficient is taken to follow a simple linear Archie law. However below a critical value (arbitrarily taken to be 50 kg m^{-3}) the bentonite diffusivity is assumed to start to become more like that of open cavity with the diffusion coefficient ramping linearly toward the open cavity diffusion coefficient when the dry density reaches zero. The cavity porewater diffusion coefficient is taken to be the same as the fracture. Thus the diffusion coefficient in the bentonite is given by

$$D_{eff} = \begin{cases} \theta D_{buff} & \rho_{sm} \geq 50 \text{ kg/m}^3, \\ \theta \left(\frac{\rho_{sm}}{50} D_{buff} + \frac{50 - \rho_{sm}}{50} D_{frac} \right) & 0 \text{ kg/m}^3 \leq \rho_{sm} < 50 \text{ kg/m}^3. \end{cases}$$

Here the porewater diffusion coefficients D_{buff} and D_{frac} (the fracture porewater diffusion coefficient, which is assumed to be the same for cavities) are taken to be $D_{buff} = 10^{-10} \text{ m}^2 \text{ s}^{-1}$ and $D_{frac} = 10^{-9} \text{ m}^2 \text{ s}^{-1}$. The value of D_{frac} is taken from [9] but no single definitive value for the buffer diffusion coefficient could be found.

10.3 Calculations

The simulations that include erosion are numerically more challenging, primarily due to the transport problem for the colloids being numerically difficult around the time that cells erode, which turns off the advection-diffusion colloid filtering effects of the bentonite in the location at which erosion takes place. For this reason simulations did not run to completion (10^6 y) but tended to slow down when colloidal releases from the exposed bentonite surfaces became large. However the calculations at the time of termination of the calculation can be compared with the corresponding calculations discussed in Section 8.3, in which erosion was assumed not to take place. It is noted that further investigation is required to resolve the numerical difficulties, but they have not prevented the required results being calculated.

10.3.1 Case when $T = 10^{-7} \text{ m}^2 \text{ s}^{-1}$ and $D_{sm} = 10^{-9} \text{ m}^2 \text{ s}^{-1}$

The evolution of the buffer dry density in the case when $T = 10^{-7} \text{ m}^2 \text{ s}^{-1}$ and $D_{sm} = 10^{-9} \text{ m}^2 \text{ s}^{-1}$ is shown in Figure 10-2 to Figure 10-5. The behaviour of the system is summarised below.

Glaciations 1-4 (to 500 000 y)

The net dry density in the buffer can be seen to be reducing during successive glaciations, with the fall in the average dry density being between 600 and 800 kg m^{-3} as can be seen in the top graph in Figure 10-7. During the first four glaciations, erosion occurs in the fracture with the distance of intrusion of the bentonite gel reducing during erosion and then recovering after the glacial periods have ended. Other than some localised small dry density non-uniformity near the fracture interface, the dry density of the buffer responds quite uniformly to the loss in bentonite mass due to erosion. After the first four glaciations the buffer dry density has reduced to around 1 150 kg m^{-3} .

The amount of material eroded during each glaciation is around 430 kg as shown in Figure 10-6. The amount of material eroded to the end of the first glacial period appears slightly greater in this figure because the time to the end of the first glacial period from the simulation start time is 10% longer than the other inter-glacial periods, since glaciations begin at 100 000 y.

By the end of the fourth glacial period the maximum depth of corrosion on the canister surface is only around 8×10^{-6} m, as can be seen in the left-most plots in Figure 10-10. In the equivalent calculation in which erosion was not simulated (Section 8.3.3) the maximum depth at 10^6 y was 10^{-5} m after nine glaciations, suggesting that the amount of corrosion that is seen so far is consistent with the no-erosion cases and that the net increase in porosity due to the loss in net dry density in the buffer and the subsequent increase in diffusion (which only assumes a linear relationship) has not had a significant effect on the amount of corrosion.

Glacial period 5 (400 000 to 500 000 y)

The trend followed during the first four glaciations is continued but the amount of eroded material, and hence the loss in the net dry density of the buffer, increases during this glacial period. The reason for this is that the fifth glacial period is the first one in which some erosion occurs inside the deposition hole leading to the formation of a cavity. This can be seen in the middle plot in Figure 10-7, which shows the dry density in the deposition hole adjacent to the fracture. During the glacial period the dry density falls locally to zero, indicating that there is a complete loss of bentonite in this location, although a non-zero density recovers at the end of the glacial period because the net bentonite density in the buffer remains above the critical value at which swelling capacity is lost (which, as noted in Section 6 was chosen arbitrarily to be $1\ 000\ \text{kg m}^{-3}$). The bottom plot in the same figure shows the dry density in the plane of the fracture at the canister surface. The density here does not fall as dramatically as at the fracture interface (but does fall as low as $1\ 000\ \text{kg m}^{-3}$) indicating that the cavity does not extend all the way to the canister surface.

Due to the increase in the surface area that is available for erosion, the amount of eroded material increases during this glaciation to 560 kg (Figure 10-6), which causes the average dry density in the buffer to fall below $1\ 050\ \text{kg m}^{-3}$, which is approaching the critical value at which swelling capacity is assumed to be lost.

Following the fifth glaciation and the brief introduction of a cavity to the system, a non-uniform corrosion profile begins to develop in which the upstream end of the canister surface in the plane of the fracture starts to experience increased rates of corrosion (Figure 10-10). The corrosion depth at the upstream end is around 2×10^{-5} m with the downstream end at around 1.8×10^{-5} m. Thus the rate of corrosion increases significantly through the fifth glaciation, with more corrosion occurring than was seen in the earlier four periods combined. This is most easily seen in Figure 10-11, which shows the evolution of the maximum corrosion depth on the canister surface in time.

Glacial period 6 (after 600 000)

During the sixth glaciation the behaviour of the system changes dramatically. After the onset of erosion, the dry density of the bentonite neighbouring the fracture again falls below the critical value required to maintain swelling capacity and erosion starts again in the deposition hole.

This time, the dry density in the areas neighbouring the interface also fall below the $1\,000\text{ kg m}^{-3}$ critical value and swelling capacity is lost over a larger area. This leads to the development of a larger cavity which by around 5 000 y into the glacial period has exposed the canister surface in the upstream direction (see the top-right plot in Figure 10-4). This cavity continues to enlarge through the glacial period and a cavity in the tangential and downstream directions begins to form, although this cavity does not reach the canister surface by 8 000 y of glacial meltwater intrusion.

Colloidal concentrations in the cavities are buffered at the limiting concentration for erosion of 0.136 mol kg^{-1} , equivalent to the erosion-limiting concentration of 50 kg m^{-3} (Section 7.2) as can be seen in Figure 10-8. The colloidal concentrations in the fracture are lower, as can be seen in Figure 10-9, which is consistent with the observations of Section 7.2 which suggested that erosion limiting concentrations would not be seen in the fracture where advective conditions dominate. In the cavities rates of advection fall quickly away from the plane of the fracture, which is the reason why erosion-limiting concentrations are allowed to develop.

During the sixth glaciation, which was not completely simulated since the simulation was halted 80% of the way through the glaciation, 1 526 kg of bentonite is eroded (Figure 10-6) and the dry density approaches the critical value for swelling capacity in the buffer that remains. Although the simulation was not run to completion (i.e. to 10^6 y) sufficient bentonite is lost that all relevant performance criteria for the buffer have failed.

The rate of corrosion on the canister surface increases dramatically with the development of the large cavities, as can be seen in Figure 10-11. The maximum depth of corrosion increases by around 0.2 mm during the (partially simulated) sixth glacial period. This rate of corrosion (0.2 mm in around 8 000 y) is consistent with the rates of around 2 cm in 10^6 y that were seen for the fastest corroding cases in Section 9.3. In Section 9.3 these fastest corroding cases were seen when the cavity aperture was constrained to be a small value. In the erosion case presented here the cavities do not remain as small, but because they do not extend the entire way around the canister as they did in the imposed cavity cases, the erosion process is concentrated on a smaller area of canister, leading to similar maximal rates of corrosion.

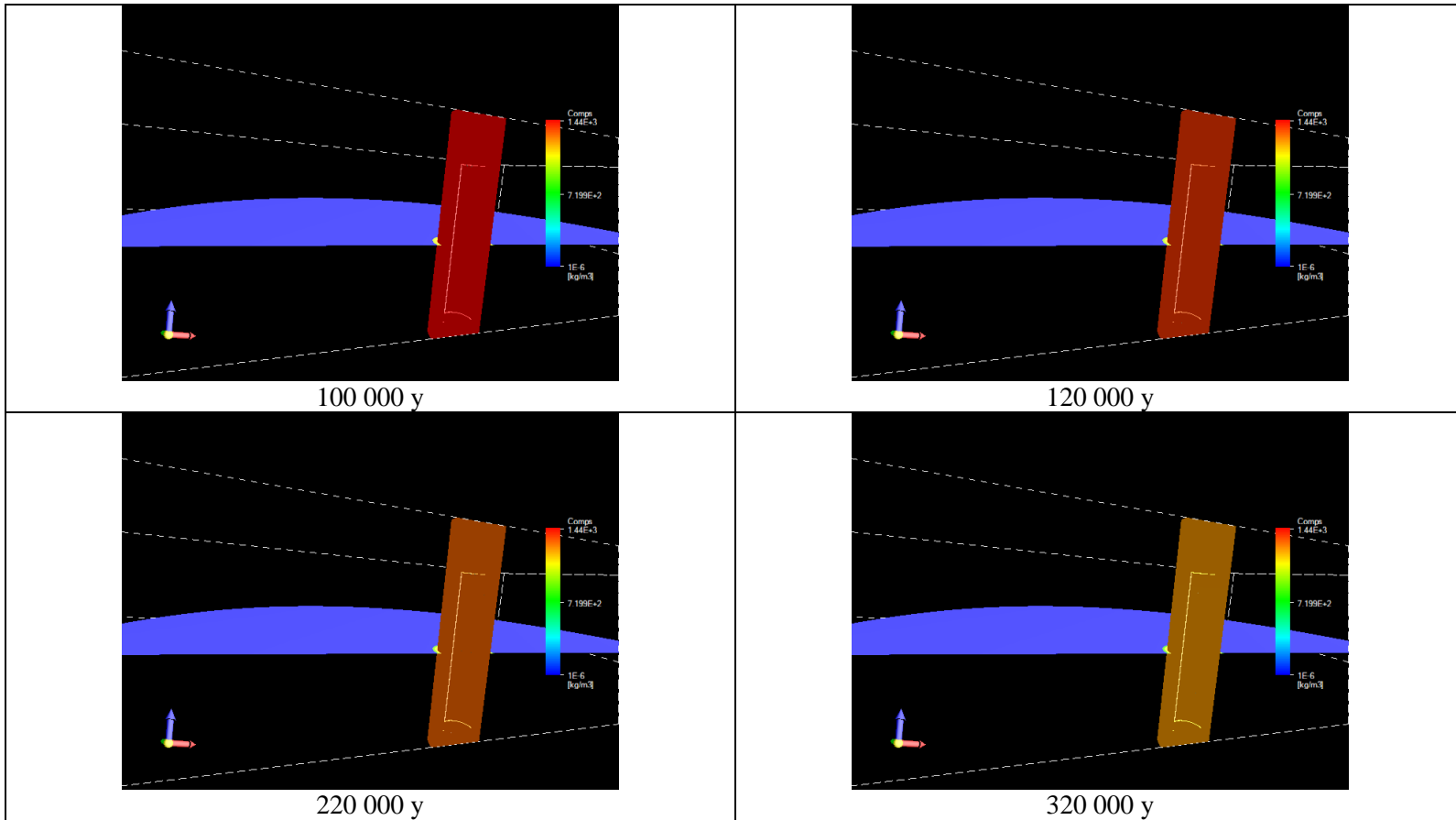


Figure 10-2 Dry density before first glaciation (top-left) after first glaciation (top-right), after second glaciation (bottom-left) and after fourth glaciation (bottom-right)

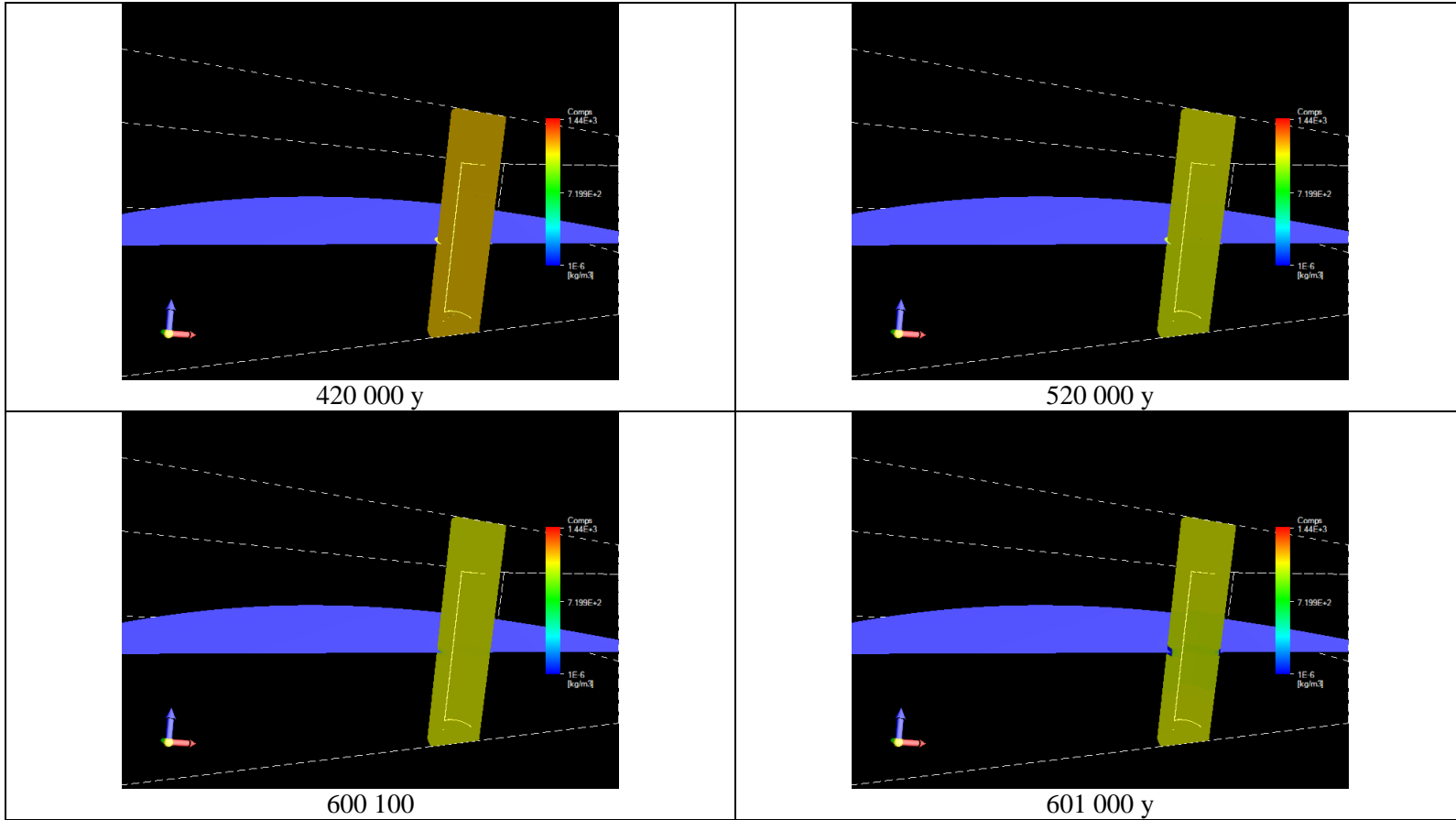


Figure 10-3 Dry density after fourth glaciation (top-left), after fifth glaciation (top-right), at the onset of the sixth glaciation at 600 100 y (bottom-left) and during the sixth glaciation at 601 000 y (bottom-right)

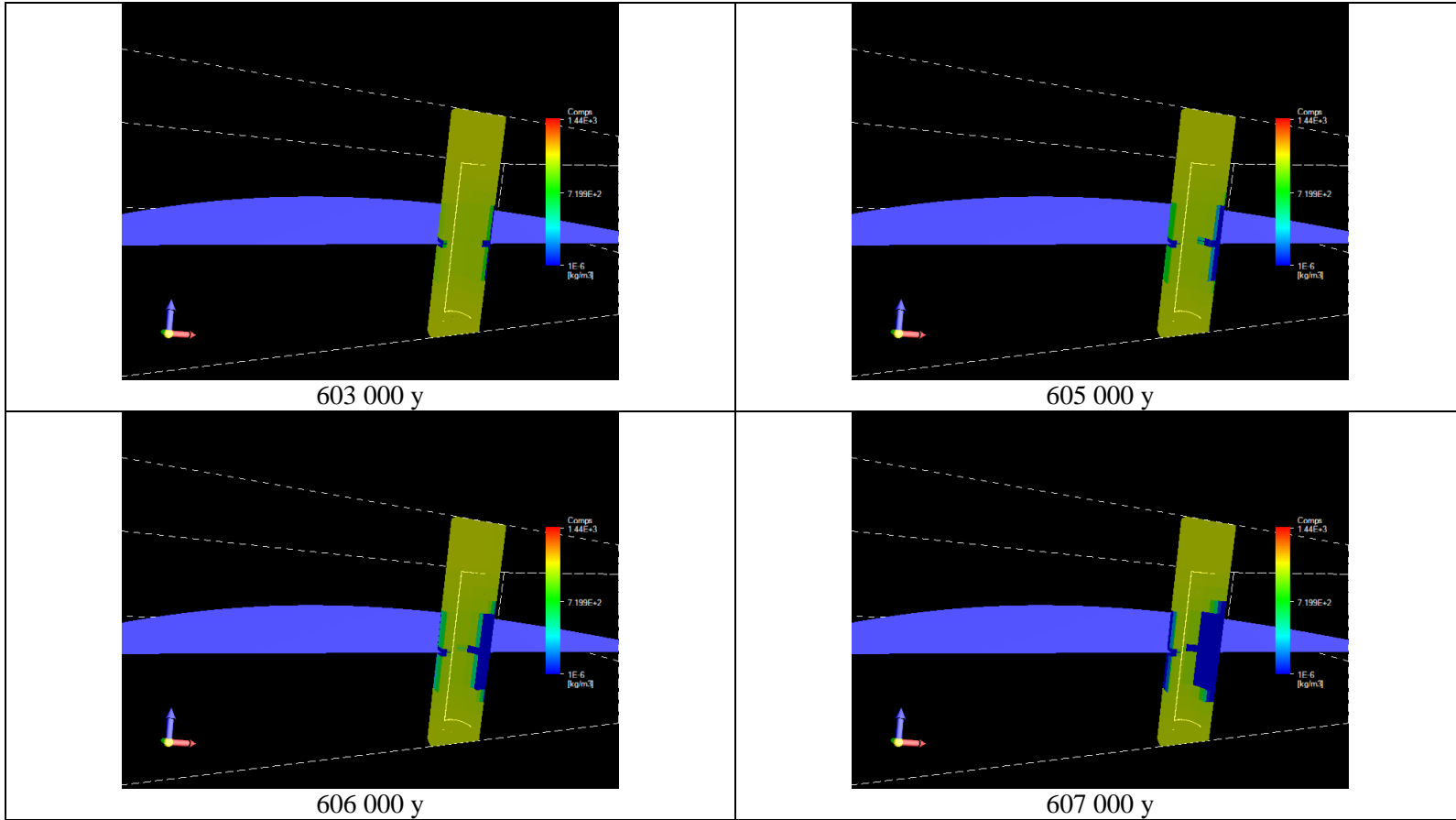


Figure 10-4 Dry density during the sixth glaciation at 603 000 y (top-left), at 605 000 y (top-right), at 606 000 y (bottom-left) and at 607 000 y (bottom-right)

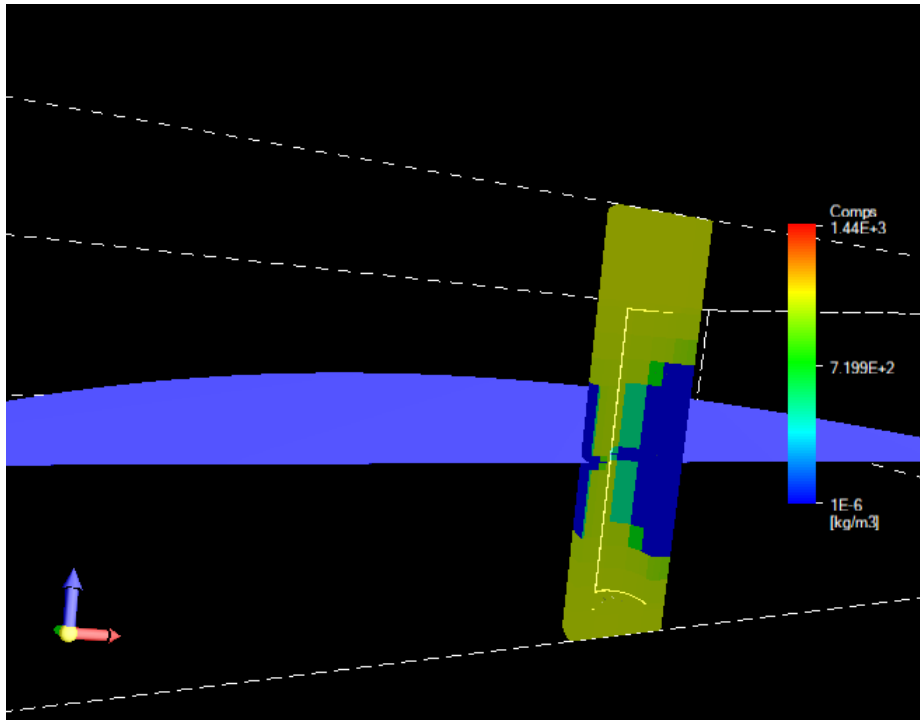


Figure 10-5 Dry density in the buffer at 608 000 y. After the density falls below the critical value at which redistribution cannot take place, erosion in the deposition hole begins, which, due to the geometry of the exposed bentonite surfaces increasing over that in the fracture, can occur at a rapid rate.

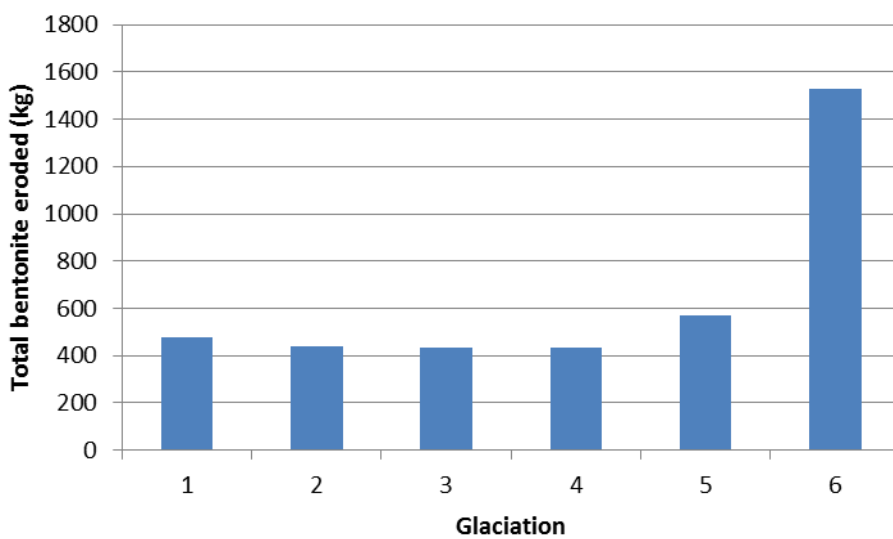


Figure 10-6 Total amounts of bentonite eroded during the first six glaciations when $T = 10^{-9} \text{ m}^2 \text{ s}^{-1}$ and $D_{sm,1700} = 10^{-9} \text{ m}^2 \text{ s}^{-1}$

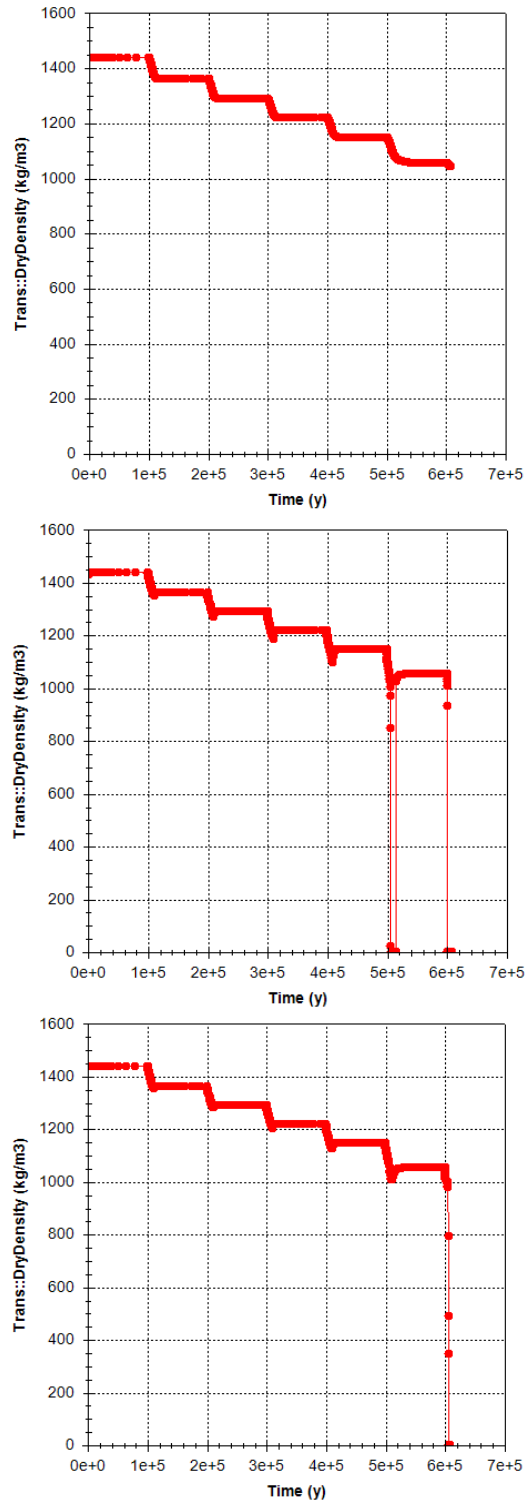


Figure 10-7 Evolution of dry density at the top of the buffer (top figure), in the buffer in the plane of the fracture adjacent to the fracture (middle) and in the buffer in the plane of the fracture adjacent to the canister (bottom)

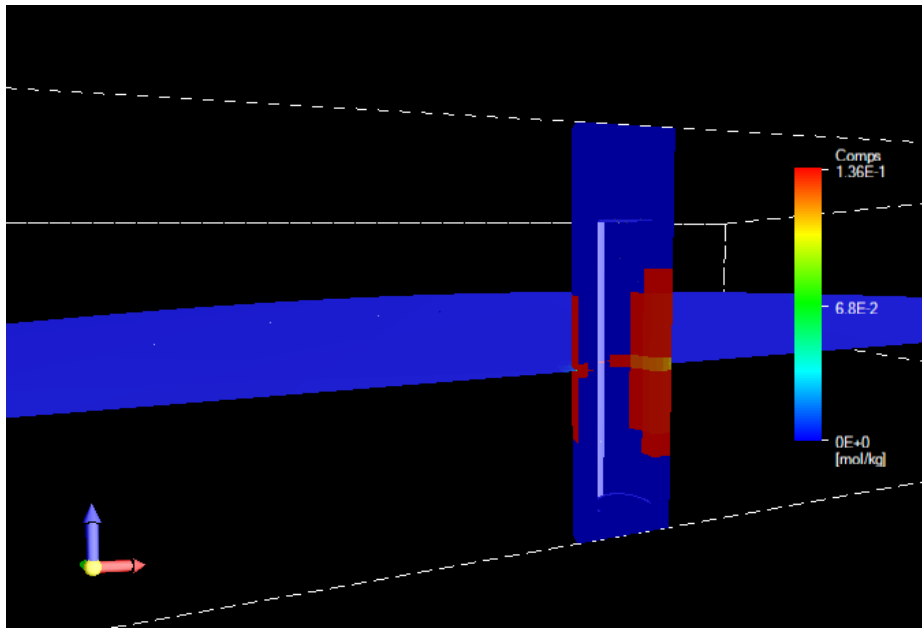


Figure 10-8 Bentonite colloid concentrations at 608 000 y. Concentrations are limited at $0.136 \text{ mol kg}^{-1}$, equivalent to the erosion-limiting concentration of 50 kg m^{-3} (Section 7.2).

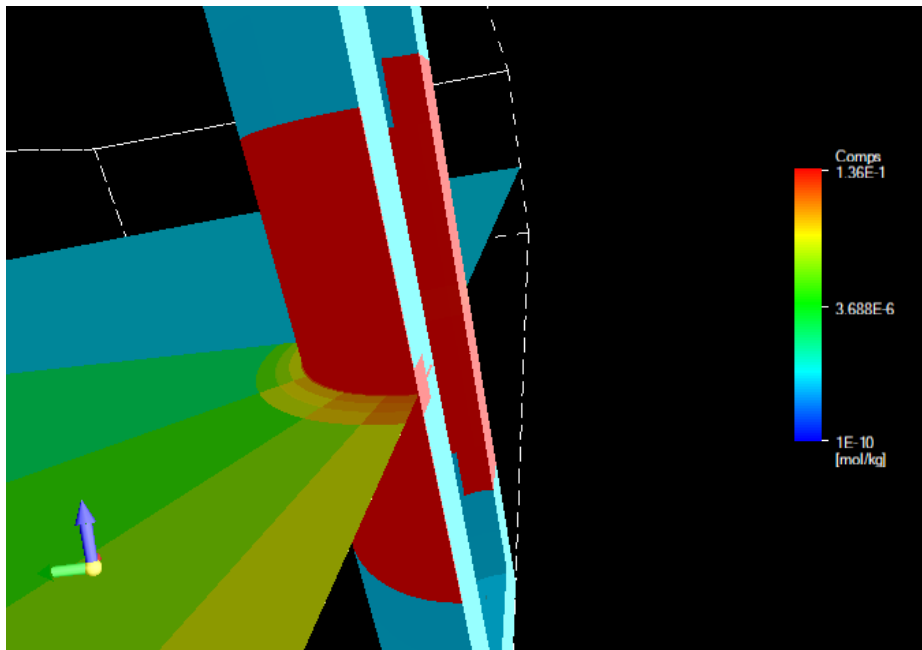


Figure 10-9 As Figure 10-8 with log scale colloid concentrations, showing the advection pathway of colloids in the fracture. Colloid concentrations in the fracture are maintained below the concentration limit due to rapid advection, as discussed in Section 7.2.

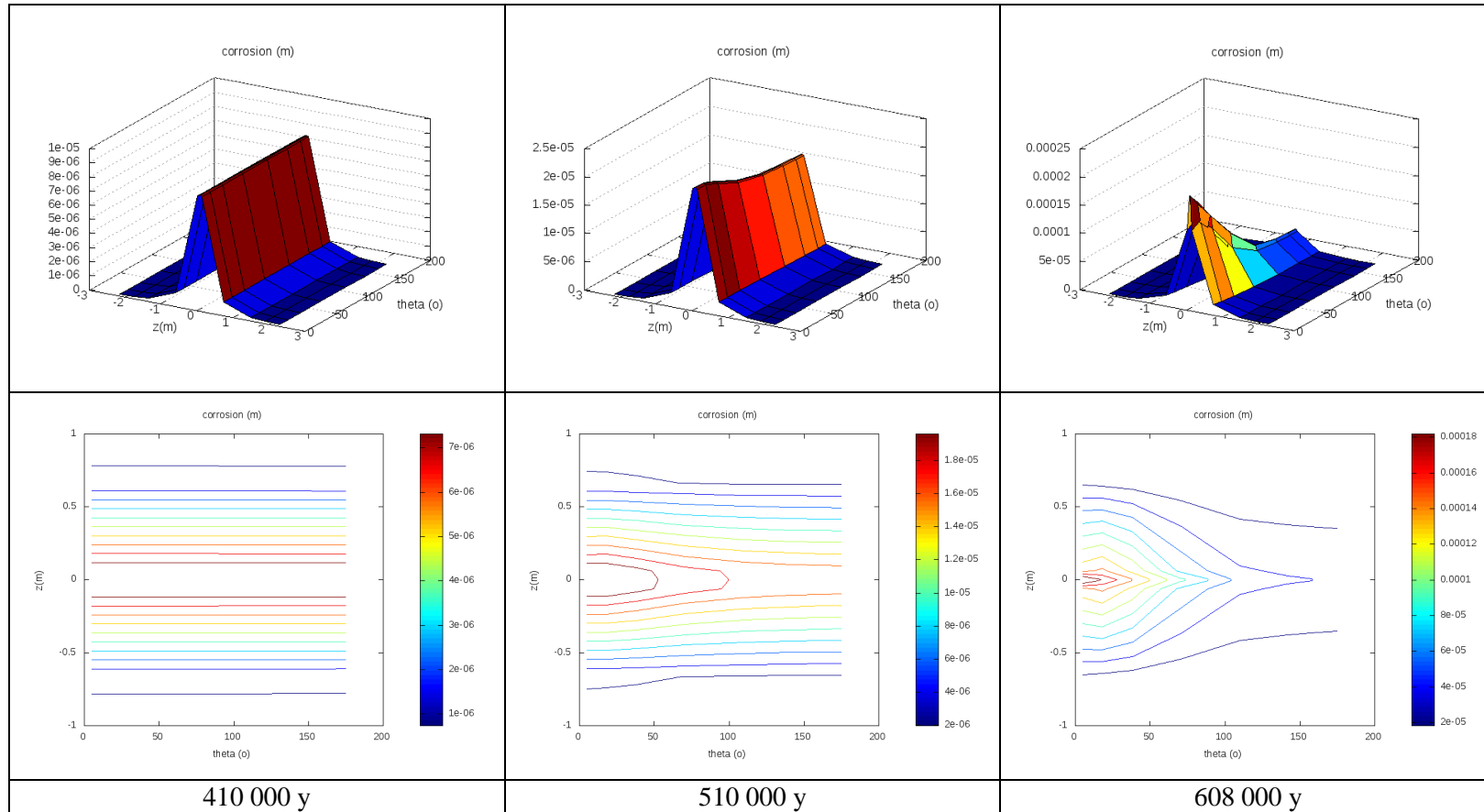


Figure 10-10 Corrosion profiles on the canister surface in the eroding buffer simulations with $T = 10^{-7} \text{ m}^2 \text{ s}^{-1}$ and $D_{sm} = 10^{-9}$

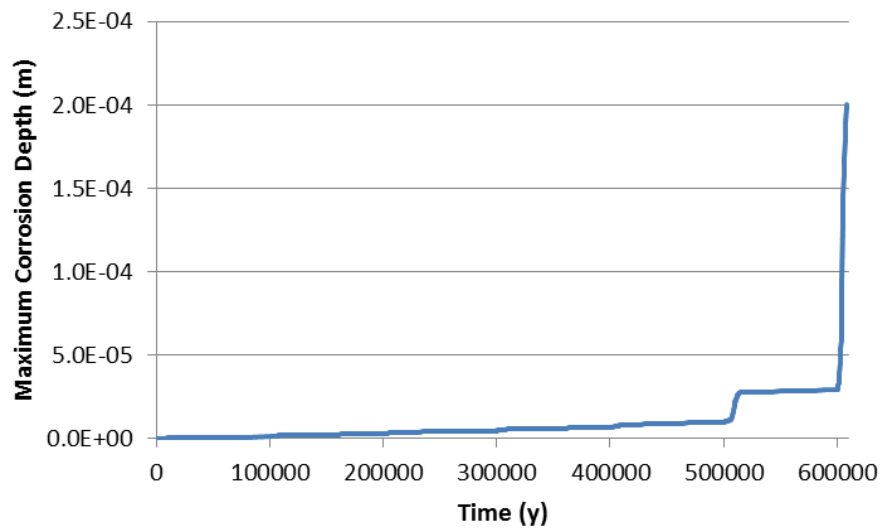


Figure 10-11 Maximum corrosion depths with time for the case $T = 10^{-7} \text{ m}^2 \text{ s}^{-1}$ and $D_{sm} = 10^{-9}$. The jump at 500 000 y is caused by bentonite being completely eroded in the fracture plane, adjacent to the fracture, during the fifth glaciation, but then re-sealing at the end of the glacial period.

10.3.2 Case when $T = 10^{-9} \text{ m}^2 \text{ s}^{-1}$ and $D_{sm} = 10^{-11} \text{ m}^2 \text{ s}^{-1}$

This case represents a smaller, less transmissive fracture than the case in discussed in Section 10.3.1 where the buffer is assumed to be less able to redistribute following erosion. In this case the effect of erosion on the buffer is much less severe. Figure 10-12 shows the evolution of dry density in the buffer, which on average only falls by around 65 kg m^{-3} during 10^6 y of evolution. The dry density adjacent to the fracture is seen to vary more during glacial periods (bottom plot in Figure 10-12) as bentonite is extruded to replenish eroded material. The amount by which the density falls during glacial periods increases with successive glaciations and reaches a minimal value of $1\,250 \text{ kg m}^{-3}$ during the last glaciation, but recovers again when glaciation stops.

The total amount of bentonite eroded in this case is less than 400 kg (Figure 10-13), which is less than that eroded during a single glaciation in the case with the more transmissive fracture in Section 10.3.1.

The corrosion profile in the up and downstream directions is uniform, since no cavities are formed and the maximum amount of corrosion in the plane of the fracture is around $1.5 \times 10^{-6} \text{ m}$. This is around 50% greater than was seen in the similar non-eroding case in Section 8.3.2. The reason for the increase is most likely the reduced diffusion distance during periods of glaciation

(when some of the gel is eroded) and the slightly increased effective diffusion in the buffer as the dry density falls and porosity increases.

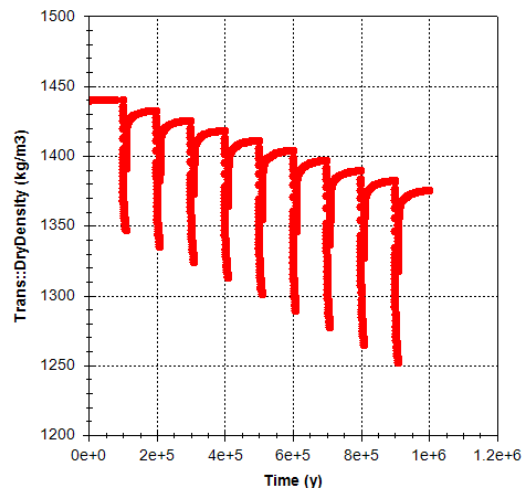
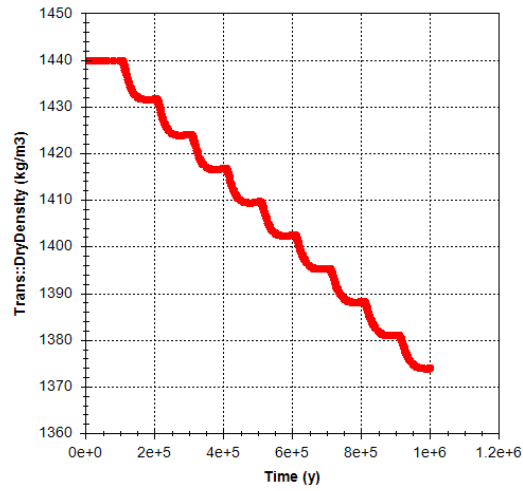


Figure 10-12 Dry density in the buffer away from the fracture plane (top) and at the fracture interface (bottom) when $T = 10^{-9} \text{ m}^2 \text{ s}^{-1}$ and $D_{sm} = 10^{-11} \text{ m}^2 \text{ s}^{-1}$

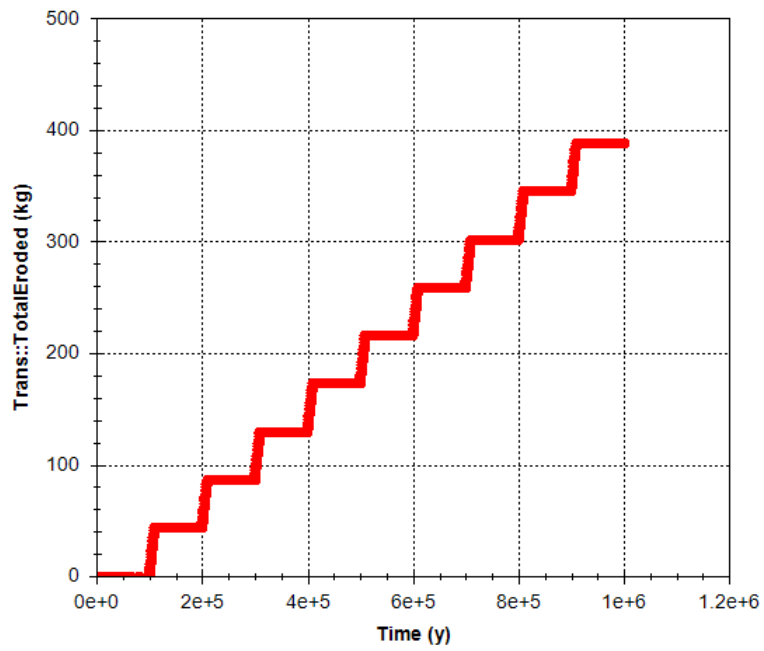


Figure 10-13 Total bentonite eroded when $T = 10^{-9} \text{ m}^2 \text{ s}^{-1}$ and $D_{sm} = 10^{-11} \text{ m}^2 \text{ s}^{-1}$

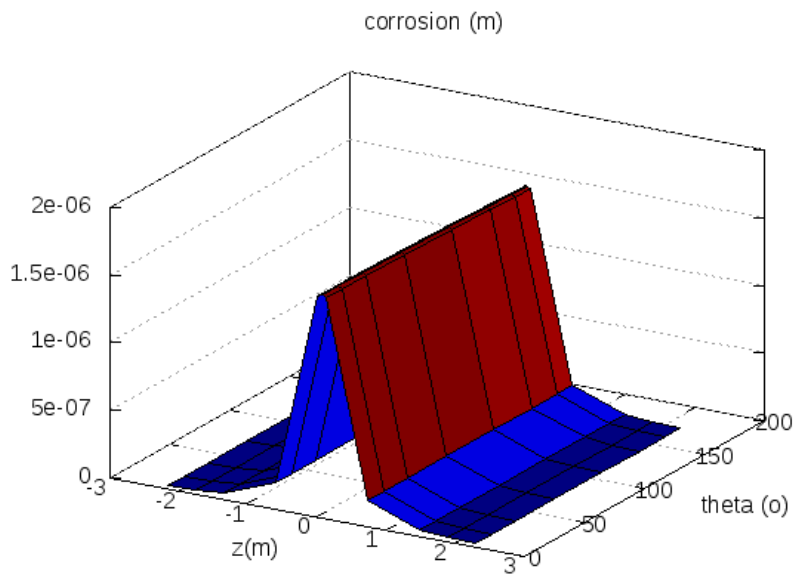


Figure 10-14 Corrosion profile on the canister surface at 10^6 y when $T = 10^{-9} \text{ m}^2 \text{ s}^{-1}$ and $D_{sm} = 10^{-11} \text{ m}^2 \text{ s}^{-1}$

10.3.3 Case when $T = 10^{-6} \text{ m}^2 \text{ s}^{-1}$ and $D_{sm} = 10^{-11} \text{ m}^2 \text{ s}^{-1}$

This case represents a larger, more transmissive fracture than the case discussed in in Section 10.3.1 where the buffer is assumed to be less able to redistribute following erosion. This case therefore represents a system that is more susceptible to erosion since flow rates are higher and bentonite redistribution is slow to respond to erosion in the fracture.

The simulation is numerically difficult due to the fast rate of colloid transport and rapid changes in colloid concentration as bentonite is eroded in successive compartments and the case was only simulated to 109 000 y, i.e. close to the end of the first glaciation. Despite the short simulation time, extensive erosion is seen to occur in the buffer and a large cavity forms across a significant portion of the buffer (Figure 10-15).

Corrosion profiles are shown in Figure 10-16. The maximal corrosion depth is around 0.3 mm after almost one glaciation (10 000 y), so depths of around 3 cm might be expected after the entire 10^6 y period, which is consistent with the larger amounts calculated in Section 9.

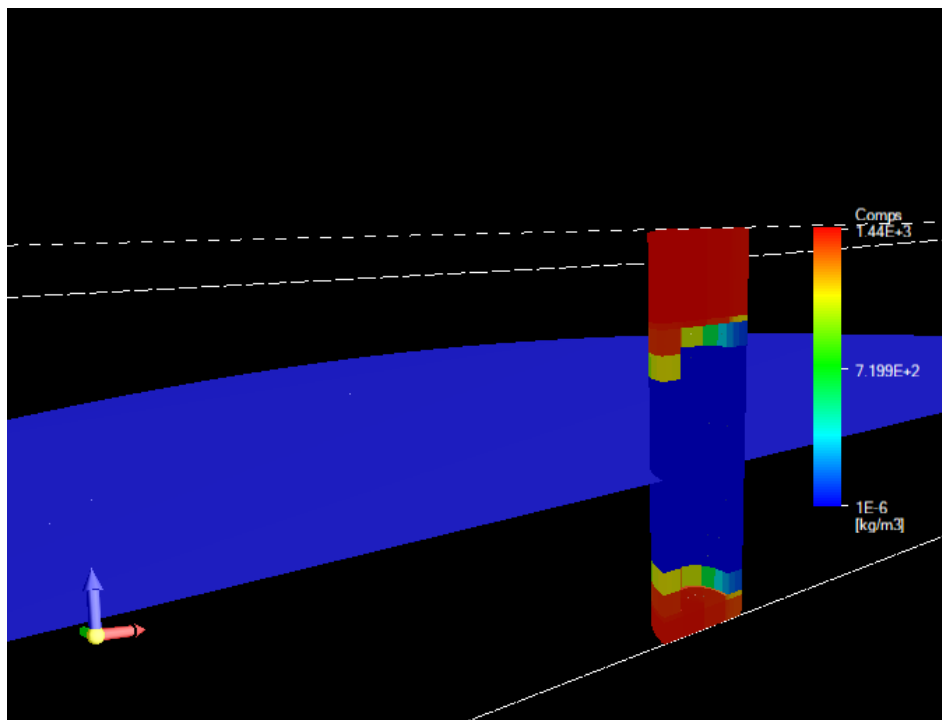


Figure 10-15 Dry density at 109 000 y when $T = 10^{-6} \text{ m}^2 \text{ s}^{-1}$ and $D_{sm} = 10^{-11} \text{ m}^2 \text{ s}^{-1}$.

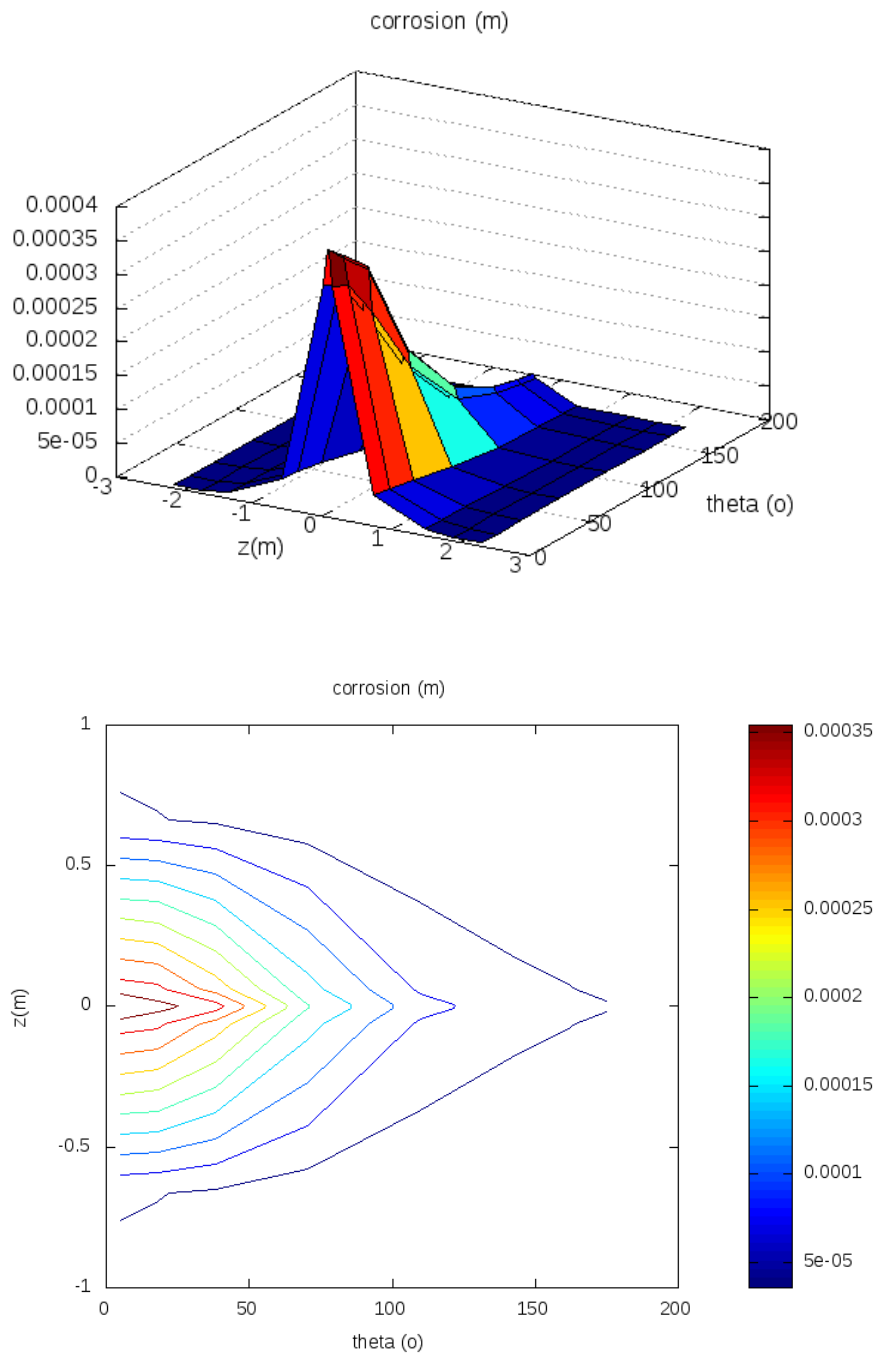


Figure 10-16 Corrosion profiles on the canister surface at 109 000 y when $T = 10^{-6} \text{ m}^2 \text{ s}^{-1}$ and $D_{sm} = 10^{-11} \text{ m}^2 \text{ s}^{-1}$

11 Modelling Erosion and Microbial Effects

Sulphate reducing microbial activity in the buffer has the potential to elevate sulphide concentrations and increase the amount of corrosion. The initial buffer dry density and the implied swelling pressure are assumed to be high enough to exclude the possibility of microbial activity, and hence sulphate reducing bacteria (SRB) will only be a potential source of elevated sulphide concentrations when the buffer swelling pressure is reduced below a critical value of 2 MPa, according to SKB's safety function indicator Bu3 [2].

Swelling pressure decreases with dry density and with salinity as shown in Figure 11-1 (taken from [2] Figure 4-7). In this figure, measured data points are shown with symbols. The lines in the plot show calculated values of swelling pressure as a function of dry density using a Donnan equilibrium approach [23].

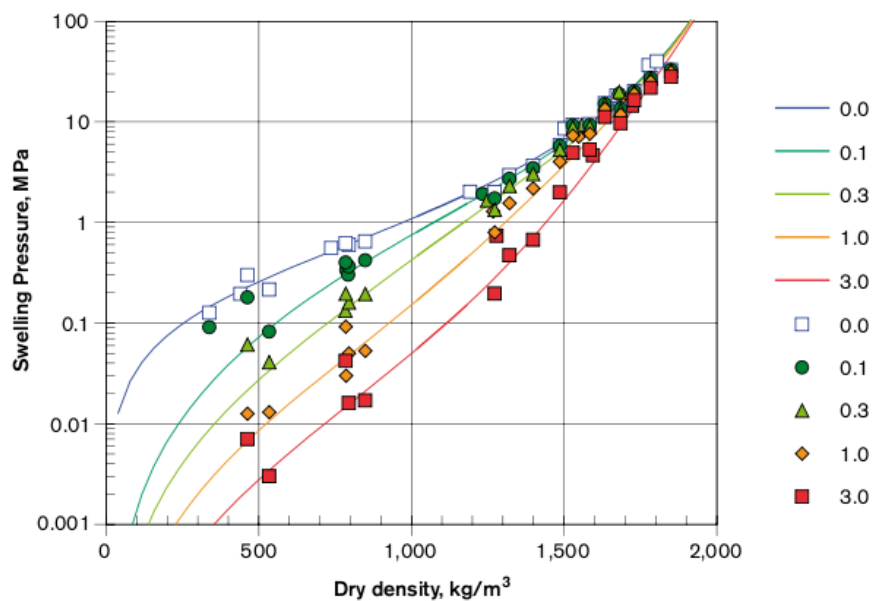


Figure 11-1 Swelling pressures of MX-80 exposed to NaCl solutions of varying concentrations (mol/L) ([2] Figure 4-7)

As noted in Section 6, an initial buffer density of $1\,655\text{ kg m}^{-3}$ is assumed (with a corresponding initial smectite dry density of $1\,440\text{ kg m}^{-3}$). From Figure 11-1, buffer densities above $1\,500\text{ kg m}^{-3}$ are sufficient to maintain swelling pressures above 2 MPa for all but the most concentrated NaCl solutions that were considered (3M). In the case of the 1M solution the

swelling pressure was found to fall below 2 MPa at a dry density of around 1 400 kg m⁻³. This is taken to be the critical buffer dry density for microbial activity in the simulations presented here. Dry densities of each mineral component in the buffer are calculated. Assuming that there is little mineral alteration in the buffer, so that the initial weight percentage persists, this gives a corresponding dry density of smectite of 1 218 kg m⁻³.

As in the earlier sections, where only sulphide was modelled in the porewater, the notation c_{HS^-} (mol kg⁻¹) is used to denote the sulphide concentration in the porewater. With $c_{SO_4^{--}}$ (mol kg⁻¹) denoting the sulphate concentration, the production rate of dissolved sulphide from microbial process is implemented using the simple expression

$$R_{SRB} = k_{SRB} c_{SO_4^{--}} \left(1 - \frac{c_{HS^-}}{c_{sol}} \right), \quad (12-1)$$

where R_{SRB} (mol kg⁻¹ s⁻¹) is the rate of conversion of sulphate to sulphide with rate constant k_{SRB} (s⁻¹). Since c_{HS^-} will initially be below the sulphide solubility limit c_{sol} (mol kg⁻¹), the $1 - c_{HS^-} / c_{sol}$ term acts to reduce the sulphide reduction rate as the solubility limit is approached.

This rate is limited in terms of how much dissolved sulphide can be produced by the availability of sulphate and by solubility limits in the in-situ conditions. SKB [2] quotes [24] as estimating the maximum amount of sulphide that can be produced microbially per deposition hole to be ~10 moles. No such maximum limit is imposed in the calculations presented here, which may therefore be deemed conservative.

It is noted the sulphide produced by SRB reactions is expected to react with Fe(II) in the porewater or diffuse away from the canister [24]. This Fe(II) reaction process is not included in the simulations presented here.

The model in Section 10.3.1 has been rerun to investigate the effects of SRB that become active in low density regions using the simple rate expression above. The parameterisation of the SRB reaction rate is discussed in Section 11.3.

11.1.1 Approach to coupling – imposing buffer evolution from earlier simulations

The modelling presented in Section 10.3.1 simulated the coupled flow, transport, buffer rheology and erosion and corrosion processes. Since there is no feedback from microbial processes on the rate of buffer erosion and rheology (the coupling is assumed to be “one-way” with density affecting the presence of microbes but not vice versa), the modelling takes advantage of the capability in QPAC to load results from earlier calculations in order to simplify the problem and decrease run times. The evolving dry density and the coupled porosity evolution from the earlier calculations have therefore

been loaded and the coupled flow and transport of reactants simulated in this setting, with the subsequent impact on corrosion being calculated.

To demonstrate the ability to load pre-calculated results, the simulation has first undertaken with the microbial reaction disabled. It is not expected that exactly the same calculations will be obtained when using this approach, because the pre-calculated results do not record the full time-history of the solution, but only contain the solution at snapshots that are interpolated during intermediate times in the solve process. However the results obtained are very similar. The corrosion profile that is obtained at 608 000 y (the time that the simulations in Section 10.3.1 were terminated) is shown in Figure 11-2, which is little different from the analogous Figure 10-10 (top-right) from the original calculation.

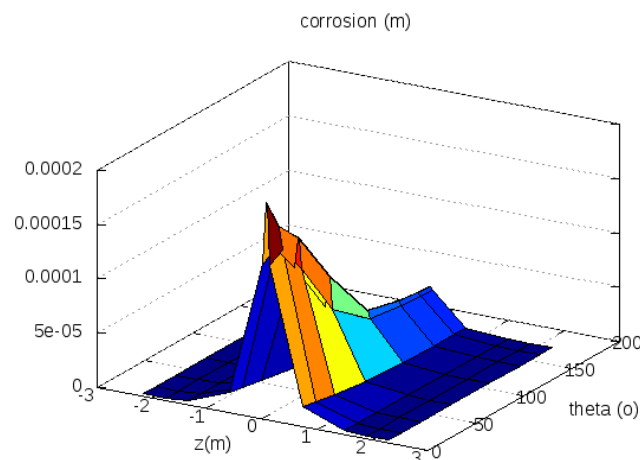


Figure 11-2 Corrosion profile obtained at 608 000 y by simulating transport and corrosion using the pre-calculated buffer erosion and porosity evolution from the simulations described in Section 10.3.1. (c.f. Figure 10-10 (top-right), which is similar.).

Using this approach, the earlier calculation can be continued by assuming that the buffer evolution remains static after the 608 000 y termination time, but with corrosion continuing in the eroded buffer at that time to the end of the simulation period at 10^6 y. The calculations are shown in Figure 11-3 and are highly non-uniform, with greater amounts of corrosion (around 2.5 mm) being seen midway between the upstream and downstream sides.

The reason for this pattern of corrosion is that the location of highest corrosion coincides with the point at which the cavity narrows (see Figure 11-4). At this point the potential for diffusive averaging of the sulphide in the vertical direction is reduced, causing a more focussed area of corrosion. This is consistent with the observations of Section 9, which found that amounts of corrosion begin to decrease when cavities become sufficiently large. In the current simulations, the corrosion rate for very localised corrosion is not treated differently from the general uniform corrosion case;

the potential for enhanced mass transport resistance caused by the corrosion pit could be considered in future studies.

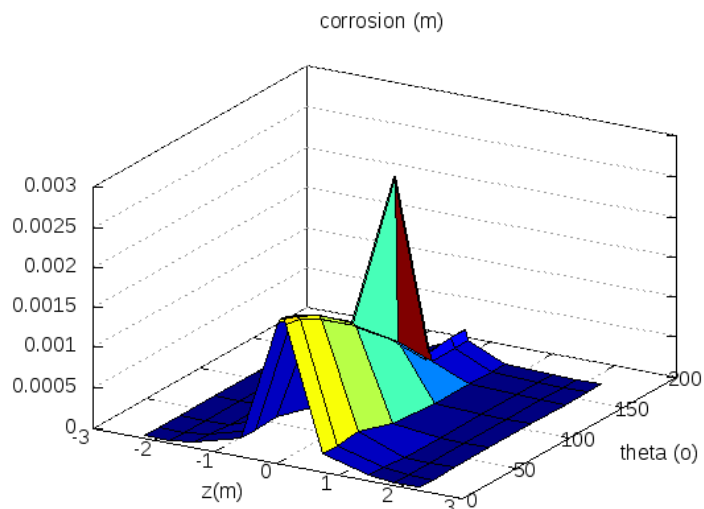
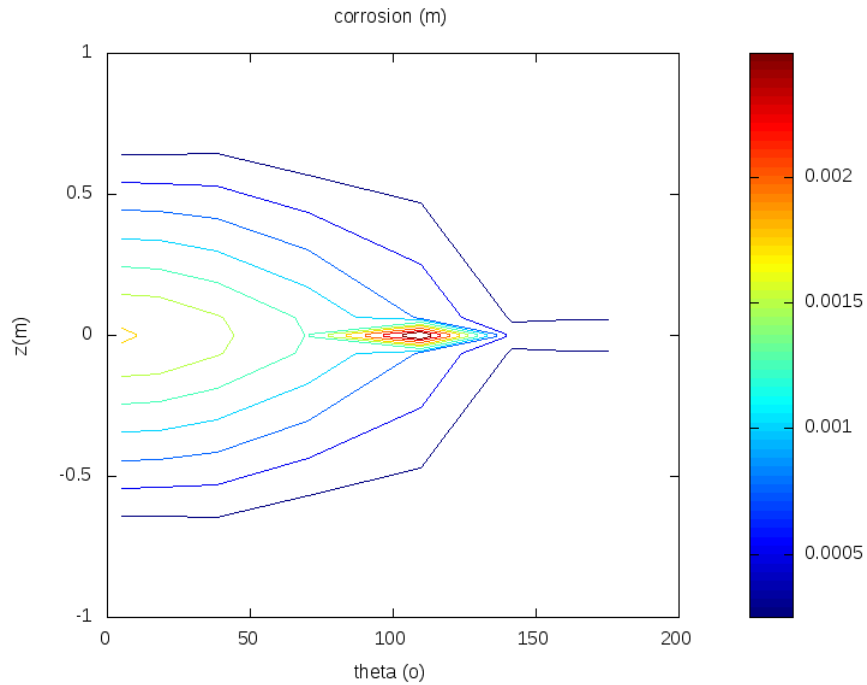


Figure 11-3 Corrosion profiles obtained when continuing the simulation to 10^6 y by assuming that the buffer remains immobile after the 608 000 y termination time of the earlier calculation.

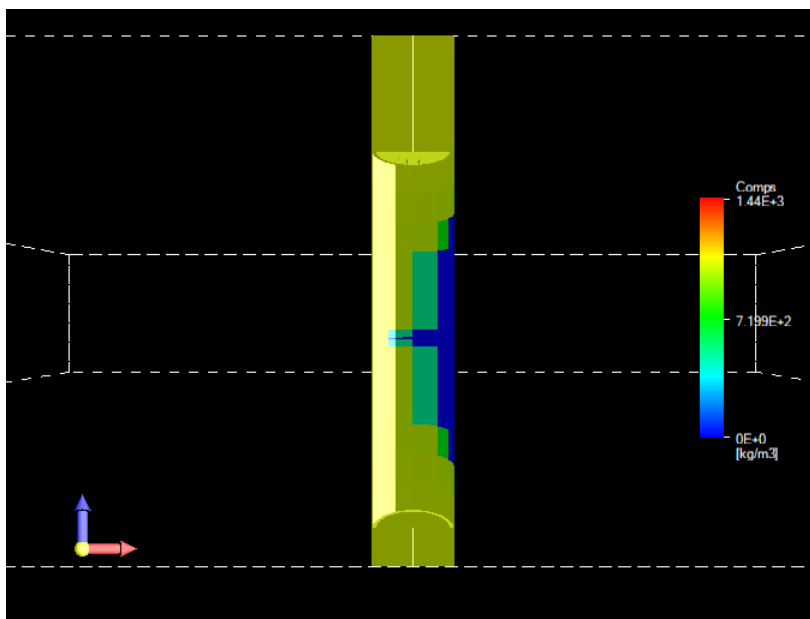


Figure 11-4 Geometry of the buffer cavity at 608 000 y, which is assumed to persist to 10^6 y in the calculations. The narrow aperture cavity on the downstream (left) side is the location of maximum corrosion.

11.2 FEP Representation

The treatment of the key FEPs are the same as those listed in Table 10-1 with the exception of FEPs related to SRB, as given in Table 11-1.

Table 11-1 Treatment of key FEPs in the microbial case simulations

FEP	FEP Treatment in the base case model
<i>High-level scenario defining FEPs (Section 2)</i>	
Sulphate reducing bacteria (SRB).	SRB are assumed to be present in the buffer and become active when the dry density of smectite falls below $1\,218\text{ kg m}^{-3}$, which is equivalent to a total buffer dry density of $1\,400\text{ kg m}^{-3}$.
The effect of SRB in the presence of cavities or reduced density buffer	Cavities and low density regions in the buffer are the only places in which active SRB can exist (see above).
<i>Processes (Section 4)</i>	
Sulphate / sulphide species	The SRB-mediated reaction is assumed to be a simple kinetic conversion reaction with a solubility limit.

FEP	FEP Treatment in the base case model
Pyrite and FeS _(am) solubility	The rate at which dissolved sulphide is produced by SRB will become zero when the solubility limit is reached. This assumes that any excess sulphide that SRB are able to produce is precipitated as pyrite or FeS _(am) , although the inventory of these minerals is not updated as a consequence.
Gypsum as a source of sulphate in the buffer	This is not represented in this simulation, although it would be possible to add this later if a more realistic porewater chemistry model could be employed.
Microbial processes	The SRB-mediated reaction is assumed to be a simple kinetic conversion reaction with a solubility limit.

11.3 Parameterisation

The parameterisation of the simulation is the same as that for the coupled erosion corrosion model in Section 10.3.1, although as noted in Section 11.1.1, the evolution of the buffer dry density and porosity is re-loaded from the earlier calculation to reduce run times.

As previously, the boundary sulphide concentration has been set to 10^{-4} mol kg⁻¹. This concentration is higher than that assumed in SKB's calculations and has therefore also been used as the sulphide solubility limit c_{sol} in equation (12-1). The sulphate concentration in Forsmark groundwater is given as 0.0052 mol/L [10]. The sulphate entering the buffer is expected to react with the buffer minerals with the resulting concentration depending on many factors including the calcium concentration which will depend on the ion exchange in the montmorillonite. A full chemical analysis is beyond the scope of the models presented here, although key chemical processes could be added in future. The sulphate concentration in MX-80 water is given in [25] as 2.94×10^{-2} mol kg⁻¹.

A sulphate concentration $c_{SO_4^{--}}$ of 10^{-4} mol kg⁻¹ has been assumed in the groundwater. This is below the concentrations reported for Forsmark and MX-80. In the absence of microbial reactions and since no other chemical reactions are included in the model, this concentration from the groundwater would be expected to spread throughout the buffer in a similar way to the tracer concentration in Figure 8-5. Hence, at the onset of microbial reactions when the bentonite density falls below the critical value, a potential "additional" 10^{-4} mol kg⁻¹ of sulphide will become available with the amount converted depending on the rate of the reaction k_{SRB} . Once the in-situ sulphate is exhausted the SRB reaction will be driven by the arrival of additional sulphate from either the groundwater or by diffusion of sulphate from intact (high density) regions of the buffer.

The SRB reaction rate, k_{SRB} , has been chosen to be 0.1 y^{-1} or 0.01 y^{-1} . The effects of faster and slower rates of microbial activity can be inferred from the two sets of calculations.

11.4 Calculations

11.4.1 Density evolution

The microbial effects cases are based on the simulation discussed in Section 10.3.1, where $T = 10^{-7} \text{ m}^2 \text{ s}^{-1}$ and $D_{sm} = 10^{-9} \text{ m}^2 \text{ s}^{-1}$. The dry density and porosity evolution arising from the erosion calculations in that simulation have been reloaded and coupled with the model of microbial reduction of sulphate described by equation (12-1). Figure 10-7 shows that in the earlier simulation the smectite dry density in the deposition hole approaches the critical smectite dry density of 1218 kg m^{-3} that has been chosen to exclude microbial activity at around the time of the third glacial period. The data from Figure 10-7 is redrawn in Figure 11-5, where it can be seen that the critical density is obtained for a short period during the third glaciation for bentonite in the fracture plane, but then the redistribution of density in the buffer causes the critical value to be exceeded again shortly after the end of the third glaciation. After the onset of the fourth glacial period the critical density is obtained everywhere.

Following these observations we would expect that no significant microbial reduction of sulphate would take place in the deposition hole until the fourth glacial period, except for a brief period of localised microbial activity during the third glacial period. The bentonite gel in the fracture has a lower density than the deposition hole, as shown in Figure 11-6. From this we would expect microbial activity to be present over most of the intruded gel region for the entire period, with the exception of the region closest to the deposition hole, where a sufficient high density is maintained up to the third glacial period (except for during the preceding glacial periods, when erosion causes removal of the gel across the entire fracture).

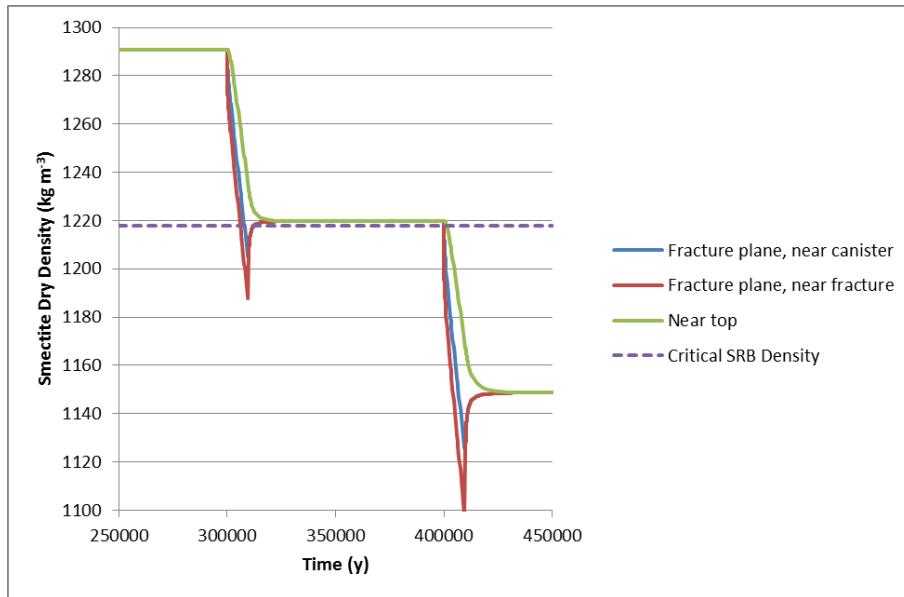


Figure 11-5 Evolution of smectite dry density between the second and fourth glacial periods compared to critical dry density for SRB

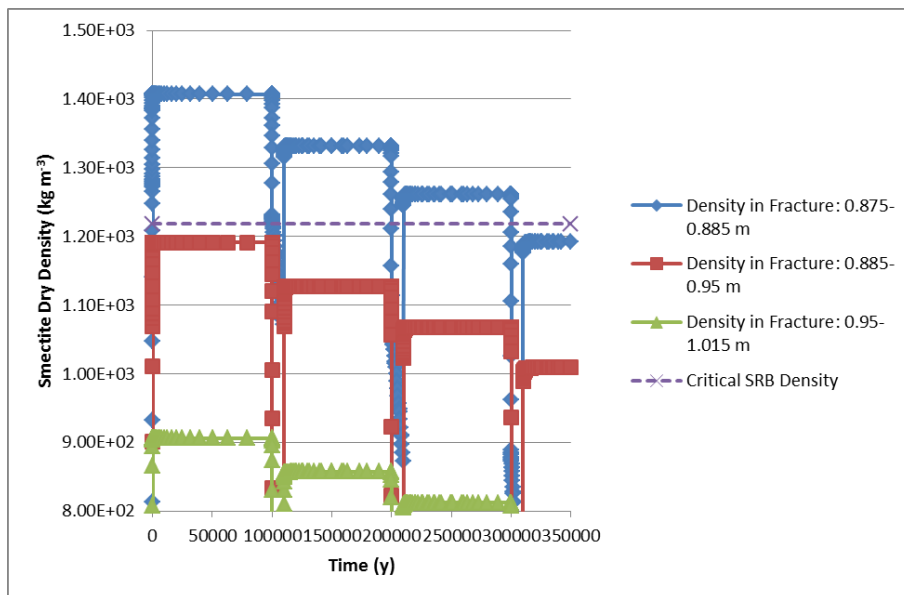


Figure 11-6 Evolution of smectite dry density in the fracture during the first, second and third glacial periods compared to critical dry density for SRB

11.4.2 Case when $k_{SRB} = 0.1 \text{ y}^{-1}$

The microbial activity in the buffer and fracture are shown in Figure 11-7 and Figure 11-8. The figures show the rate of microbial reduction of sulphate ($\text{mol kg}^{-1} \text{ y}^{-1}$) across the entire system at snapshots at the start at end of each glacial period.

As expected from the preceding discussion, while gel is present in the fracture, microbial activity proceeds there for the entire simulation, except very close to the deposition hole, where the gel density is close to that of the buffer.

Glaciations 1-3 (to 400 000 y)

Within the deposition hole, no significant microbial activity takes place until the third glacial period. From the snapshot towards the end of the glacial period (Figure 11-7 bottom-right) it can be seen that microbes have become active in the buffer during this period, but from the snapshot at the start of the fourth glacial period (Figure 11-7 top-left) it can be seen that the microbial activity ceases when the buffer density is redistributed. This is consistent with the observations on the buffer dry density discussed in Section 11.4.1 based on the plot in Figure 11-5.

Glacial period 4 (400 000 to 500 000 y)

During the fourth glacial period, microbes again become active in the deposition hole. The snapshot at the end of the fourth period (Figure 11-7 top-middle) suggests that the activity is less than during the third glacial period. The reason for this is that the sulphate concentrations in the buffer were higher during the third glacial period, having had 300 000 y to accumulate. Figure 11-9 shows that most of the sulphate that was present was consumed in SRB reactions during the third glacial period so that the amount of sulphate present for SRB reactions during the fourth glacial period is less, having only had a single inter-glacial period to accumulate. The resulting rate of sulphate reduction is around half that in the previous glacial period, as can be seen in Figure 11-10.

By the end of the fourth glacial period, average smectite dry densities in the deposition hole have fallen to around 1.150 kg m^{-3} (Figure 11-5), so that microbial activity can continue through the non-glacial periods that follow. This leads to an increase in sulphide concentrations across the buffer, with the concentration adjacent to the fracture approximately doubling from $4 \times 10^{-7} \text{ mol kg}^{-1}$ to around $7.5 \times 10^{-7} \text{ mol kg}^{-1}$ during the non-glacial period to 500 000 y.

Glacial period 5 (500 000 to 600 000 y)

During the fifth glacial period the microbes continue to be active everywhere in the buffer with sulphide concentrations elevated above the case when microbes were not included. The flux of sulphate entering the buffer is balanced by conversion to sulphide by SRB, which leads to a continuous rate

of sulphate reduction of $1.5 \times 10^{-6} \text{ mol kg}^{-1} \text{ y}^{-1}$ at the location in the buffer adjacent to the fracture.

The corrosion profile on the canister surface at 600 000 y is shown in Figure 11-11 (bottom). The similar plot from the earlier simulation is shown at the top of the figure. The net amount of corrosion can be seen to have approximately doubled with the inclusion of microbes in the simulation. The increased corrosion towards the upstream end is less pronounced (but still visible) in the case with microbes, since the distribution of microbes everywhere in the buffer, due to the overall reduction in density, acts to smooth out the profile. The fact that the amount of corrosion has doubled is not surprising. From Figure 11-11 it can be seen that most of the corrosion prior to 600 000 y took place in the period from 500 000 y to 600 000 y. In the present simulation with microbes included, the sulphide concentration in the buffer is approximately doubled in regions where microbes are present due to the choice of sulphate concentration in the incoming water (sulphate concentrations were set to be the same as sulphide concentrations at $10^{-4} \text{ mol kg}^{-1}$). Hence the potential amount of sulphide in the buffer would be double the previous amount if all sulphate was converted to sulphide, which leads to twice the amount of corrosion.

Glaciation 6 (to 608 000 y)

The calculation was terminated at 608 000 y to be consistent with the earlier simulation. By this time a considerable cavity has developed in the buffer (see Figure 11-5).

Since the cavity exposes the surface of the canister to the incoming water, the potential microbial reduction of sulphate does not have such a large effect on the amount of corrosion after the cavity develops. This is because the sulphide concentrations in the incoming water composition were chosen to already be at the maximum solubility limit, so the SRB has a lesser effect. This can be seen in Figure 11-12, which shows the amount of corrosion of the canister surface at 608 000 y in the case when microbes are not present (top) and are present (bottom). The peak amounts of corrosion in the fracture plane are only around 25% greater when SRB are included in the simulation (as opposed to double at earlier times when transport of sulphide to the surface is diffusion limited). There is slightly more corrosion away from the fracture plane in this simulation than the simulation in which SRB were not included.

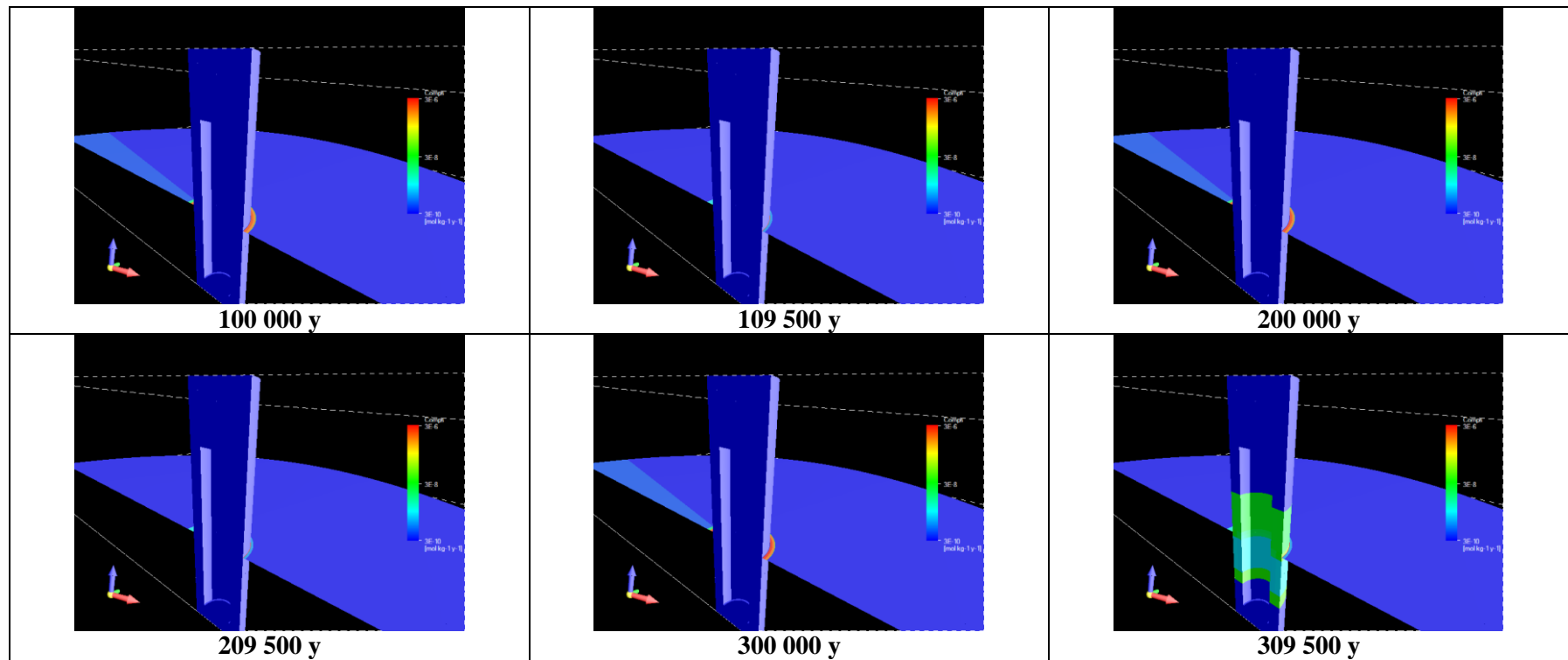


Figure 11-7 Rates of SRB conversion of sulphate to sulphide. Times shown are snapshots at the beginning and near the end of each of glacial periods 1-3

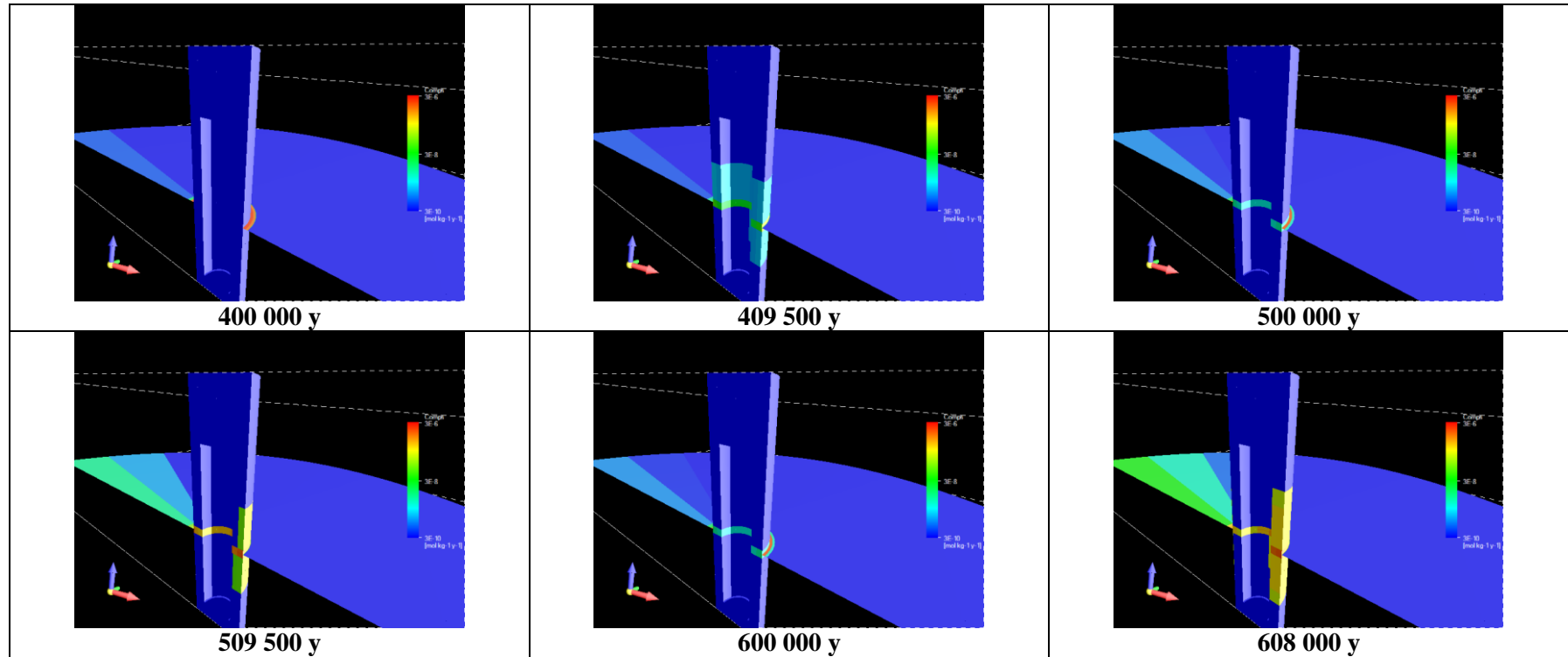


Figure 11-8 Rates of SRB conversion of sulphate to sulphide. Times shown are snapshots at the beginning and near the end of each of glacial periods 4 and 5 and at the start of glacial period 6 and 608 000 y (the end time of the simulation in Section 10.3.1)

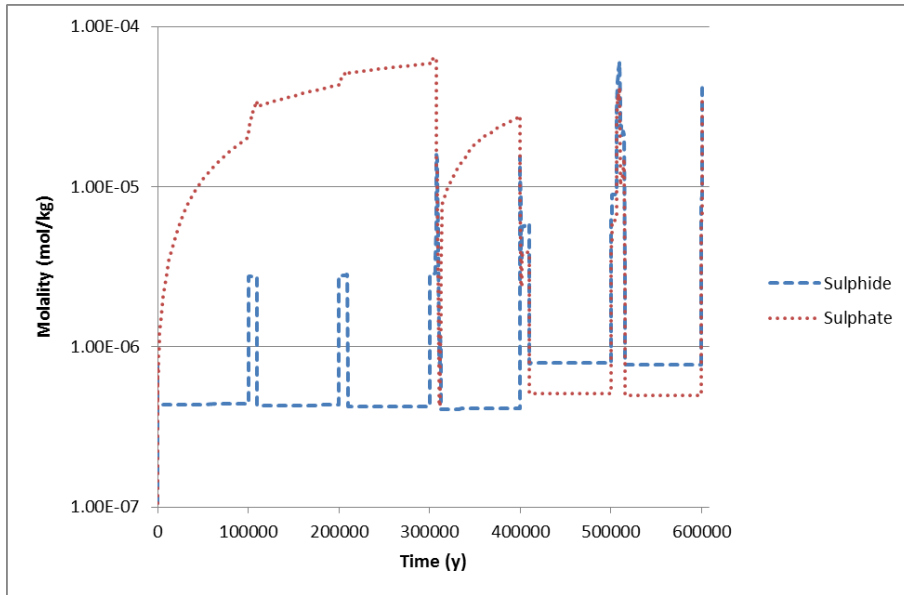


Figure 11-9 Sulphate and sulphide concentrations in the buffer in the plane of the fracture near the fracture

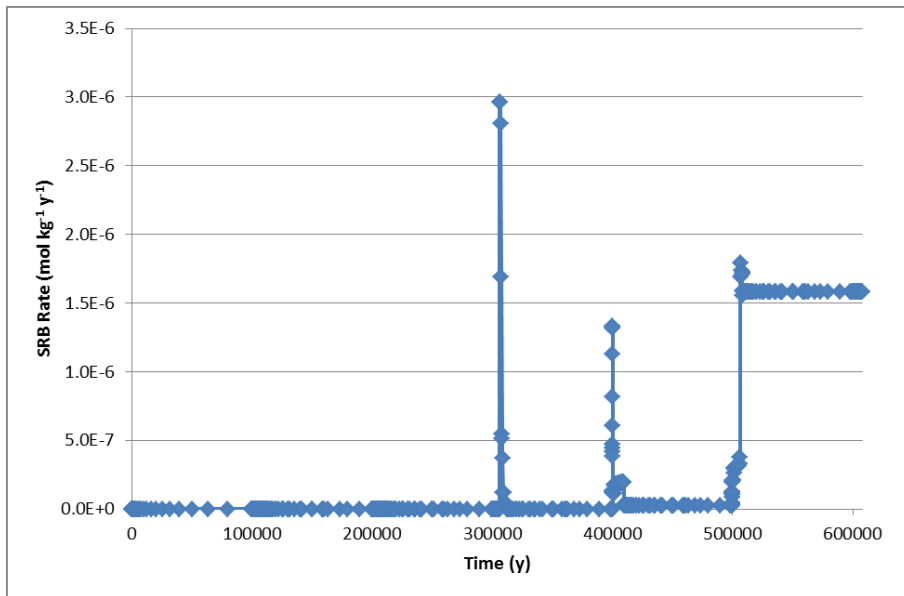


Figure 11-10 Rates of microbial reduction of sulphate in the buffer in the plane of the fracture near the fracture (c.f. Figure 11-9)

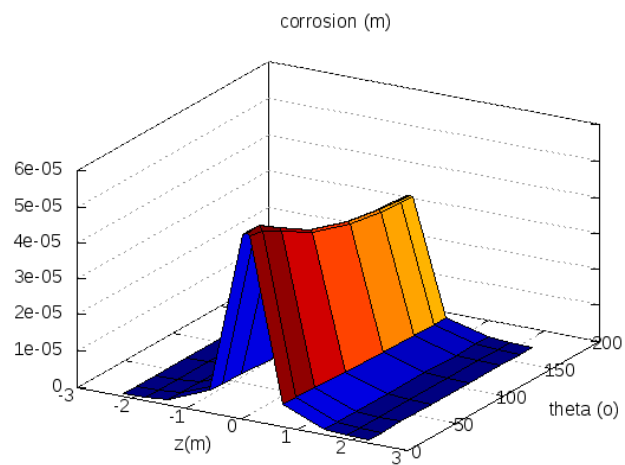
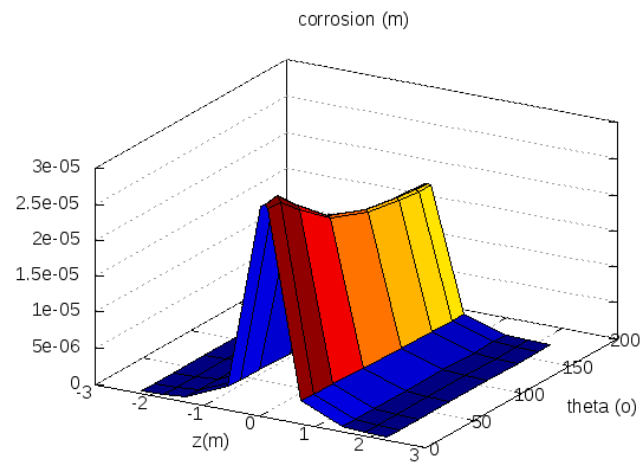


Figure 11-11 Corrosion profile on the canister at 600 000 y from no-microbe simulation (top) and simulation with microbes (bottom)

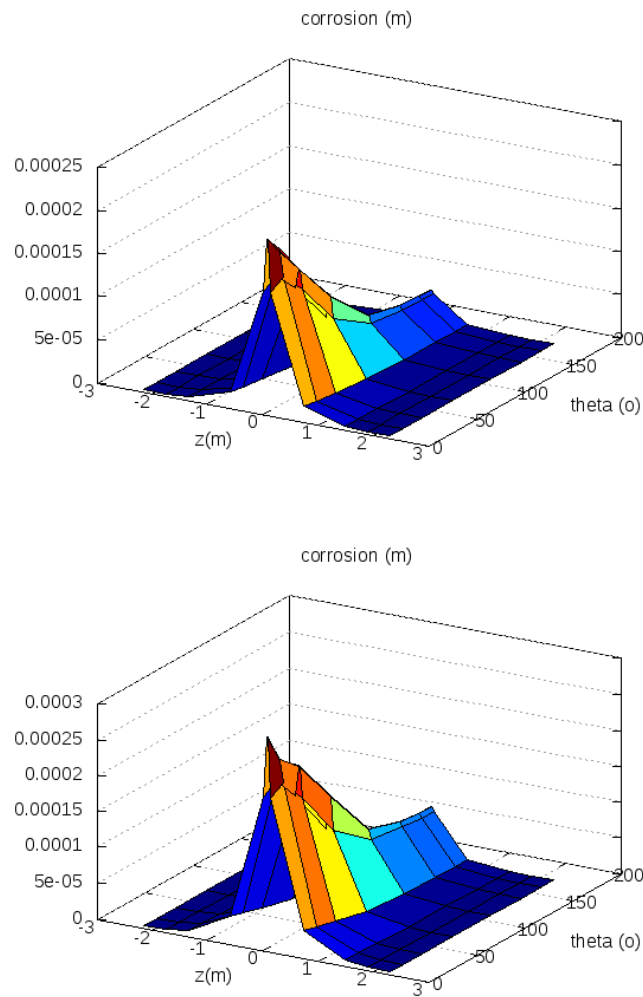


Figure 11-12 Corrosion profile on the canister at 608 000 y from no-microbe simulation (top) and simulation with microbes (bottom)

11.4.3 Case when $k_{SRB} = 0.01 \text{ y}^{-1}$

When the rate of microbial activity is reduced to 0.01 y^{-1} , the amounts of corrosion in the plane of the fracture prior to the formation of cavities is around 25-30% more than was observed when SRB were not included in the simulation (Figure 11-13), compared to around double when $k_{SRB} = 0.1 \text{ y}^{-1}$ (Section 11.4.2).

As in the case when $k_{SRB} = 0.1 \text{ y}^{-1}$, after the formation of cavities during the sixth glaciation the peak amounts of corrosion in the plane of the fracture are similar to those in the non-SRB case, since transport of sulphide to the canister surface becomes advection dominated, with concentrations in the groundwater already at the sulphide solubility limit.

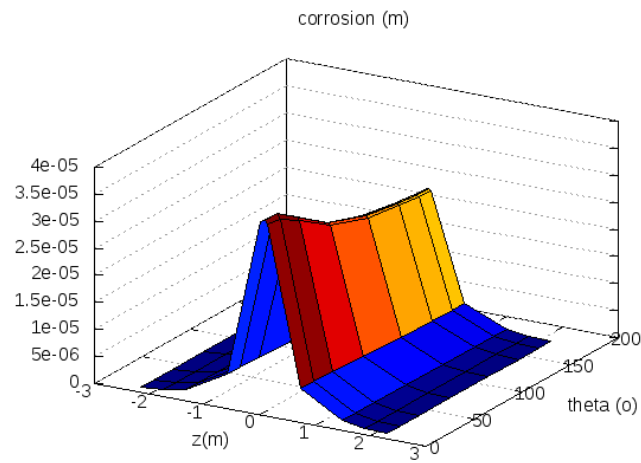
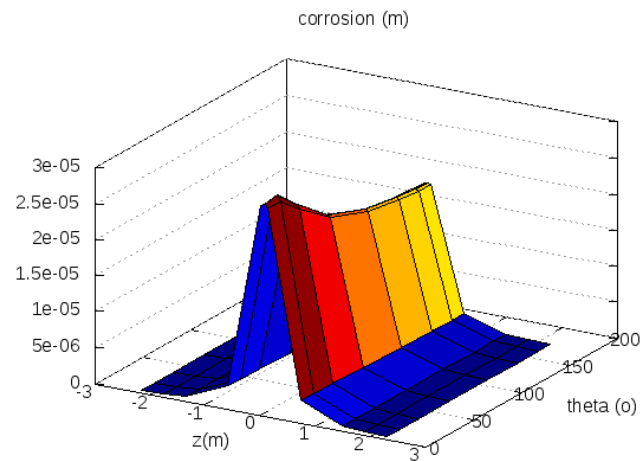


Figure 11-13 Corrosion profile on the canister at 600 000 y from no-microbe simulation (top) and simulation with microbes (bottom)

12 Summary

The work presented represents a preliminary assessment of the coupled processes related to erosion of a bentonite buffer and corrosion of a copper canister. Additional work would be needed to explore uncertainties and sensitivities relating to the sulphidic corrosion of copper canisters in the SKB KBS-3 design. In developing the models used here, a range of features and processes have been represented which have the potential to influence the amount of corrosion, at a level of detail that is consistent with reproducing the main features of system behaviour over realistic timescales. The processes can be parameterised through a number of simple input parameters that could be used to calibrate the models if sufficient information were to become available from experimental measurements or more detailed mechanistic process models.

The focus of the modelling was to investigate factors that could lead to non-uniform corrosion of the canister surface. The most likely scenario leading to such evolution is one in which a flowing fracture intersects a canister deposition hole. The simulations presented investigate the potential for erosion caused by the intrusion of (relatively) fast flowing glacial meltwaters to lead to non-uniform corrosion profiles. Due to uncertainties in the composition of meltwaters, water compositions have not been varied during glacial periods, which possibly represents a conservatism assumption if sulphide concentrations fall during glacial water intrusion. However, since the duration of the glacial periods represents only 10% of the overall simulation time, the effect of this assumption is expected to be small.

Simulations been presented in which:

- ▲ No buffer erosion occurs;
- ▲ Cavities due to buffer erosion are imposed;
- ▲ Buffer density evolves as erosion takes place, leading to the development of cavities; and
- ▲ Microbial reduction of sulphate occurs in regions where the buffer density falls below that needed to exclude microbes.

In the case when no buffer erosion takes place, estimated amounts of corrosion after one million years are minimal with maximum corrosion depths less than 0.1 mm for the range of fracture transmissivities that have been considered. In the imposed cavity simulations, corrosion depths at the millimetre scale were seen for cavity geometries that could possibly develop, and in extreme cases, with cavity geometries that might not be physically realistic, maximal corrosion depths of up to 2 cm after one million years were calculated.

In the simulations in which buffer density was allowed to evolve according to a simplified rheology model, the characteristic behaviour that might be expected from an eroding buffer was seen. In particular, the effect of repeated glaciations was evident. The buffer swelling capacity was sufficient to allow it to recover from the early glaciations and continue to extrude gel into the fracture, with amounts of eroded material on the order of 500 kg per glacial period; the amount of corrosion was limited to small amounts consistent with the no erosion cases. The net density of the buffer reduced as a consequence of each glaciation until it fell sufficiently low that it could no longer provide sufficient swelling capacity for gel intrusion to continue. At this point, erosion in the deposition hole region began to take place which led to the rapid development of a cavity. At this time corrosion rates increased rapidly.

An initial analysis of erosion-limiting processes suggested that the colloidal concentration limits on the order of 50 kg m^{-3} that have been suggested by SKB as a possible corrosion-limiting factor are unlikely to be reached under the modelling assumptions employed in regions where advective transport dominates, i.e. in the fracture and in the fracture plane within cavities. To increase colloidal concentrations in the water it would be necessary for flow rates during the glacial period to be smaller than assumed here, or for other colloid transport inhibiting processes to be included such as filtration or coagulation. However, as was seen in the erosion simulations, the colloidal concentration limit can be reached in cavities in regions away from the fracture plane where diffusive conditions dominate transport.

In the simulations that included microbial reduction of sulphate the simple representation of the microbial conversion process had no requirement for an energy source. The simulations were undertaken by re-loading the buffer response to erosion from earlier simulations, since it was assumed that the coupling was one-way, with erosion processes not being dependent on microbial processes. Re-loading the outputs in this way reduced the complexity of the modelling and reduced run times.

The activation and subsequent suppression of microbial activity as buffer, redistribution took during periods of recovery acted to increase density in eroded regions, were represented in the simulations. For the case presented it was found that a brief period of microbial activity was possible during the third glacial period. Since sulphate concentrations in the buffer had been allowed to accumulate for three inter-glacial periods the amount of microbial was actually higher than in later glacial periods, when the microbial activity was then limited by the amount of sulphate that could re-invade the areas in which the microbes were active. No buffering of sulphate concentrations by buffer minerals (e.g. gypsum) was included in the simulation, although sulphate concentrations were limited by the in-situ groundwater concentrations, which were taken to be $10^{-4} \text{ mol kg}^{-1}$.

Continued microbial activity in the buffer was excluded until the fourth glacial period. After this time sulphide concentrations in the buffer were increased over the non-microbial levels, resulting in a doubling of the amount of corrosion of the canister surface until cavities appeared for the faster microbial rate that was considered. This doubling is an upper bound

for the boundary conditions that were applied, where sulphate concentrations in the porewater and sulphide solubility limits were taken to be equal. After cavities formed, the calculated rates of corrosion were similar to the non-SRB case, since sulphide was then advected to the canister surface at groundwater concentrations. However, there was slightly more corrosion away from the plane of the fracture when SRB were included due to the microbial reduction of sulphate that was able to diffuse vertically in the buffer.

In future work the models developed so far could be extended to include additional features, processes and modelling variations such as those listed in Appendix A. In particular, the current suite of models does not include chemical processes other than implicit treatments through the specification of the sulphide content in the fracture porewater. In future it would be possible to include ion-exchange reactions, particularly for the Na-Ca pair, in order to assess the possibility of CCC-based stabilisation of the bentonite. It is possible that, following the discussion in Section 7.2, advective conditions in the porewater may make it difficult to establish divalent calcium ion concentrations at sufficiently high levels in the fracture to prevent bentonite erosion but this remains to be investigated. Dissolution of gypsum may also play an important role in providing a source of Ca^{2+} ions.

13 Relevance for the SR-Site Review

The objective of the work presented here was to demonstrate a flexible and independent capability that can be used to support regulatory review.

Building on earlier modelling work and utilising the general-purpose QPAC software, a coupled model for the evolution of the EBS system through a sequence of glacial cycles has been developed and applied. The flexibility of the approach has been demonstrated by modelling a range of scenarios and variants covering both parameter variations and conceptual model alternatives.

Although many simplifying assumptions have been made, particularly in the chemistry aspects, a rich variety of behaviour is seen in the modelling results. The linkage between erosion and corrosion has been clearly demonstrated to depend on factors such as the precise geometry of any cavities that form in the buffer due to erosion in addition to the physical and chemical parameters of the system.

The flexibility of the QPAC approach, with models being coded in the input language, has allowed the required range of processes to be treated at a suitable level. It proved possible to develop models over relatively short time periods, demonstrating that the approach should be sufficiently responsive to address issues that arise during the review process. In future work the sophistication with which particular processes are modelled can be adjusted to suit the needs of specific investigations.

The simulations presented here should be taken as illustrative and indicative. At this preliminary stage of the modelling it would be premature to consider any of the results to be definitive.

References

- [1] Robinson, P. C. and Watson, C. E. (2010) Analysis of barrier performance: Quintessa's Input to Consequence Analysis Modelling Ahead of SR-Site. Quintessa Report to SSM QRS-1503A-2.
- [2] SKB (2006) Long-term safety for KBS-3 repositories at Forsmark and Laxemar – a first evaluation: Main Report of the SR-Can project, SKB TR-06-09.
- [3] Apted M., Bennett, D. and Saario, T. (2009) A Review of Evidence for Corrosion of Copper by Water, SSM 2009:30.
- [4] Maul, P. R., Benbow, S. J., Bond, A. E. and Robinson, P. C, (2010) Modelling coupled processes in the evolution of repository barrier systems using QPAC-EBS. SSM 2010:25.
- [5] Strömberg, B. (2010) Personal communication. Presentation entitled "Meeting with Quintessa, 16/5-2010".
- [6] Neretnieks, I., Lui, L. and Moerno, L. (2009) Mechanisms and models for bentonite erosion. SKB TR-09-35.
- [7] Geier, J. (2010) Email communication, 8th September 2010.
- [8] SKB (2006) Initial state report for the safety assessment SR-Can, SKB TR-06-21.
- [9] SKB (2006) Data report for the safety assessment SR-Can, SKB TR-06-25.
- [10] Atkins, P. and de Paula, J. (2009) Physical Chemistry, OUP.
- [11] King, F. (2007) Mixed-potential modelling of the corrosion of copper in the presence of sulphide, Posiva 2007-63.
- [12] Geochemist's Workbench database, thermo.com.V8.R6.230
- [13] Auqué, L. F., Gimeno, M. J., Gómez, J. B., Puigdomenech, I., Smellie, J. and Tullborg, E.-L. (2006) Groundwater chemistry around a repository for spent nuclear fuel over a glacial cycle: Evaluation for SR-Can, SKB TR-06-31.
- [14] Bath, A. and Hermansson, H.-P. (2009) Biogeochemistry of Redox at Repository Depth and Implications for the Canister, SSM 2009:28.

- [15] Bond, A. and Watson, C.E. (2008) The Use of QPAC-EBS for Project THERESA Benchmarking Studies. Quintessa Report QRS 3009A-1 version 3.0
- [16] Bath, A. (2010) Draft report on porewaters for SSM (unpublished).
- [17] Apted, M., Arthur, R., Bennett, D., Sällfors, G., Savage, D. and Wennerström, H. (2010) Buffer erosion: An overview of concepts and potential safety consequences, SSM Report 2010:31.
- [18] Outters, N. (2003) A generic study of discrete fracture network transport properties using FracMan/MAFIC, SKB R-03-13.
- [19] Liu, J. and Neretnieks, I. (2006) Physical and chemical stability of the bentonite buffer, SKB R-06-103.
- [20] Quintessa (2010) QPAC: Quintessa's General Purpose Modelling Software, Quintessa Report QRS-QPAC-11.
- [21] Börgesson, L. and Hernelind, J. (2006) Consequences of loss or missing bentonite in a deposition hole: a theoretical study, SKB TR-06-13.
- [22] SKB (2006) Buffer and backfill process report for the safety assessment SR-Can, SKB TR-06-18.
- [23] Karnland, O., Olsson, S., Nilsson, U. and Sellin, P. (2006) Mineralogy and sealing properties of various bentonites and smectite-rich clay materials, SKB TR-06-30.
- [24] Hallbeck, L., Grivé, M., Gaona, X., Duro, L. and Bruno J (2006) Main organic materials in a repository for high level radioactive waste, SKB R-06-104.
- [25] Arcos, D., Grandia, F. and Domènech, C. (2006), Geochemical evolution of the near field of a KBS-3 repository, SKB TR-06-16.
- [26] Hermansson, H-P., Tarkpea, P. and Holgersson, S. (2001), Composition of copper whiskers grown on copper in repository environment, SKI Report 01:45.

Appendix A: Possible Variants for Future Studies

With the simulations undertaken it was not possible to consider all potential variants. This appendix records ideas for possible variants that might be considered in future studies. It is intended to provide a check list for future work and should not be considered to be comprehensive.

The appendix is structured to match the main text so that the variants described can easily be related back.

A.1 System Features and Geometry

A.1.1 The Buffer

It is possible that some piping may occur during resaturation that could lead to flow pathways around the bentonite along the buffer/rock interface. Hence, one possible variant is:

- △ Investigation of the effect of flow pathways along the buffer/rock interface resulting from piping or erosion.

The distribution of gypsum distribution is potentially heterogeneous (expected weight percentages with uncertainties are listed in [2]). Therefore the following variant could be considered:

- △ Investigation of the impact of heterogeneously distributed gypsum within the buffer.

A.1.2 Cavities

Alternative erosion processes might apply within the cavity. At this stage no definite alternative approaches have been identified.

A.1.3 The Buffer/Host Rock Interface

Piping flows may have the effect of increasing the amount of naturally occurring sulphide diffusing into the buffer, since they potentially increase the contact area between the buffer and the groundwater. They also increase the area over which erosion can occur and so may lead to enhanced erosion. The following variant could therefore be considered:

- △ Include in the model a thin feature to allow for the possibility of channelled flow around the buffer (piping).

A.1.4 The Fracture

The location of the intersection of the fracture with the deposition hole (top/middle/bottom) and its orientation may lead to alternative evolution of the system. In particular, if the fracture is intersected by the tunnel EDZ it may transport corrodants or cementitious water towards the buffer.

This leads to the following variants:

- △ Investigation of the impact of channelled flows;
- △ Investigation of impact of corrodants transported via the EDZ;
- △ Investigation of the impact of cementitious waters.

A.1.5 Bentonite Gel

The bentonite gel properties are likely to be different from those in the non-gel bentonite in the buffer; for example its transport properties may be different. The following variant is therefore possible:

- △ Assume that the bentonite gel transport properties are different from those of the buffer.

A.1.6 The Canister

There is potential for the explicit modelling of corrosion products, but no specific approach has been suggested.

A.1.7 The Buffer/Backfill Interface

Instead of a fixed location for the interface:

- △ Assume that the position of the buffer /backfill interface responds to buffer and backfill density changes.

A.1.8 Tunnel Backfill

If the position of the buffer/backfill interface were assumed to move then the backfill would need to be modelled. Similar processes to the buffer would apply.

A.1.9 The EDZ

The tunnel EDZ could interact with the flow field in/around the buffer if the fracture intersects the EDZ or if piping flows are assumed that intersect the EDZ. Additionally, flows in the EDZ distinct from those in the fracture

could also play a role in the buffer evolution. Thus a potential variant for future work is:

- △ Include the EDZ as a boundary condition to provide an alternative source of water, and hence sulphate and sulphide, near the top of deposition hole.

A.2 Processes

A.2.1 Thermal Processes

There will be a continuing thermal pulse even after resaturation, so a potential variant is:

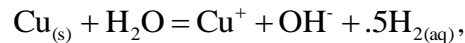
- △ Include consideration of the evolving temperature from decay heat in the canister.

A.2.2 Corrosion

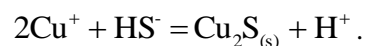
Instead of treating corrosion as transport controlled, a possible variant case is:

- △ Treat corrosion as a kinetically controlled function of Eh.

The sulphidic corrosion reaction could be represented as a two-stage process beginning with the dissolution reaction:



followed by a precipitation reaction:



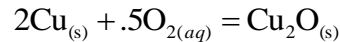
Treating the corrosion process in this way provides a mechanism for corrosion products to precipitate in the buffer rather than only on the copper surface, an effect that has been observed in the LOT experiments.

Speciation of CuCl_2^- will tend to keep Cu^+ concentrations low (CuCl_2^- will dominate Cu^+ when the concentration of Cl^- is greater than $10^{-2.4}$ mol/kg using 25°C data from thermo.com.V8.R6.230). Forsmark has Cl^- concentrations of 0.153 mol/kg [13].

Thus

- △ Treat corrosion as a two stage process, allowing ions to diffuse into the buffer before precipitating as product minerals.

Oxic corrosion, represented by the reaction



is also possible but is not the focus of this modelling study. It is also only relevant at early times during resaturation, unless glacial waters carry a lot of oxygen, and so its effect could be included in the initial conditions.

The Cu_2O corrosion product may form a layer that could inhibit the transport controlled reaction. Additionally, secondary Cu_2S precipitation has the potential to affect sulphide solubility and may enhance transport (as has been claimed as a mechanism for “whisker” growth) [SKI TR-01:45]. The role of corrosion products is ignored in the current study, but in future studies the following variant could be considered:

- △ The corrosion boundary condition could take account of the transport resistance of corrosion products layers by including its effect on diffusion to the canister surface, noting that an appropriate mass transfer rate would be needed.

A.2.3 The Role of Pyrite in the Buffer

The role of pyrite is a complex area and further variants may be useful but none are specifically identified at this stage.

A.2.4 Other Chemical Processes

Instead of treating sulphate and sulphide as separate species in the model, a possible variant is:

- △ Kinetically control the sulphate / sulphide redox reaction.

Instead of assuming that sulphide is buffered by pyrite and $\text{FeS}_{(am)}$ solubility, a variant would be to:

- △ Assume that $\text{FeS}_{2(am)}$ is kinetically converted to pyrite.

It would also be possible to:

- △ Include Cl^- reactions explicitly.

Cement waters (e.g. from grouted fractures in tunnel that meet with deposition hole fractures or EDZ) could be considered. Thus

- △ The effect of cementitious waters on buffer chemistry could be considered.

A.2.5 Microbial Processes

Thus the variants that can be considered are:

- △ The H₂ form of the microbial reaction could be used.
- △ The CH₄ form of the microbial reaction could be used.

These approaches could be combined and treated as a model for the electron donor needed for sulphate to sulphide conversion.

There is most likely a solubility limit associated with microbial HS⁻ production. This limit, or the solubility limit from FeS_(am), will provide an upper bound on feasible sulphide concentrations in the system. The limit is not known for the microbial activity, but sensitivity to an artificially imposed limit could be investigated. If the microbes continue to produce sulphide when the mineral controlled limit has been reached then precipitation must occur (in the current study the production rate goes to zero in that case). Thus:

- △ Solubility limits for microbially produced sulphide can be imposed on the system..
- △ Excess microbial production of sulphide could be allowed to precipitate as FeS_(am).

A.2.6 Bentonite Redistribution

The following variant for bentonite redistribution could be considered:

- △ The redistribution process is characterised by density differences and bentonite composition.

An alternative to the imposed viscosity treatment is:

- △ The bentonite viscosity parameter is linked to rheological properties of bentonite.

A.2.7 Erosion

The bentonite solid to colloidal bentonite loss term could be characterised in a different way:

- △ Assume a colloid solubility-limit based term, which would implicitly depend on the groundwater flow rate.

A.2.8 Bentonite Gel Extrusion

There are clearly alternative approaches to modelling gel intrusion, but no specific variants have been suggested at this stage.

A.2.9 Groundwater Flow

The fracture itself may be channelled, hence

- △ A heterogeneous permeability field in the fracture could be used to investigate the effect of channelling.

Also,

- △ At the buffer/rock interface any channels that have developed due to piping and survived the swelling phase could be represented by suitably parameterising the thin feature representing this feature.

A.2.10 Groundwater-mediated Transport

No variants have been suggested as the processes are well established.

A.2.11 Spalling

Spalling is a consequence of the local stress field around the deposition hole, leading to fracturing of the host rock, and hence enhanced hydraulic conductivity, near the deposition-hole surface. If spalling occurs in the vicinity of the fracture this may lead to enhanced flows across a wide area of the deposition-hole surface, reducing the transport resistance associated with the buffer/fracture interface, as indicated in [1]. Hence

- △ Spalling effects could be investigated by reducing the transport resistance of the fracture/buffer interface.

2011:12

The Swedish Radiation Safety Authority has a comprehensive responsibility to ensure that society is safe from the effects of radiation. The Authority works to achieve radiation safety in a number of areas: nuclear power, medical care as well as commercial products and services. The Authority also works to achieve protection from natural radiation and to increase the level of radiation safety internationally.

The Swedish Radiation Safety Authority works proactively and preventively to protect people and the environment from the harmful effects of radiation, now and in the future. The Authority issues regulations and supervises compliance, while also supporting research, providing training and information, and issuing advice. Often, activities involving radiation require licences issued by the Authority. The Swedish Radiation Safety Authority maintains emergency preparedness around the clock with the aim of limiting the aftermath of radiation accidents and the unintentional spreading of radioactive substances. The Authority participates in international co-operation in order to promote radiation safety and finances projects aiming to raise the level of radiation safety in certain Eastern European countries.

The Authority reports to the Ministry of the Environment and has around 270 employees with competencies in the fields of engineering, natural and behavioural sciences, law, economics and communications. We have received quality, environmental and working environment certification.

Strålsäkerhetsmyndigheten
Swedish Radiation Safety Authority

SE-171 16 Stockholm
Solna strandväg 96

Tel: +46 8 799 40 00
Fax: +46 8 799 40 10

E-mail: registrator@ssm.se
Web: stralsakerhetsmyndigheten.se